

DESIGN AND IMPLEMENTATION OF
A MEMS BASED GRAVIMETRIC DETECTOR
FOR CYTOMETRY APPLICATIONS

A THESIS SUBMITTED TO
THE GRADUATE SCHOOL OF NATURAL AND APPLIED SCIENCES
OF
MIDDLE EAST TECHNICAL UNIVERSITY

BY

EKREM BAYRAKTAR

IN PARTIAL FULFILLMENT OF THE REQUIREMENTS
FOR
THE DEGREE OF MASTER OF SCIENCE
IN
ELECTRICAL AND ELECTRONICS ENGINEERING

SEPTEMBER 2010

Approval of the thesis:

**DESIGN AND IMPLEMENTATION OF
A GRAVIMETRIC DETECTOR
FOR MEMS BASED CYTOMETRY APPLICATIONS**

submitted by **EKREM BAYRAKTAR** in partial fulfillment of the requirements for the degree of **Master of Science in Electrical and Electronics Engineering Department, Middle East Technical University** by,

Prof. Dr. Canan Özgen
Dean, Graduate School of **Natural and Applied Sciences** _____

Prof. Dr. İsmet Erkmén
Head of Department, **Electrical and Electronics Engineering** _____

Assoc. Prof. Dr. Haluk Kùlah
Supervisor, **Electrical and Electronics Eng. Dept., METU** _____

Examining Committee Members:

Prof. Dr. Tayfun Akın
Electrical and Electronics Engineering Dept., METU _____

Assoc. Prof. Dr. Haluk Kùlah
Electrical and Electronics Engineering Dept., METU _____

Prof. Dr. Cengiz Beşikçi
Electrical and Electronics Engineering Dept., METU _____

Prof. Dr. Nevzat Güneri Gençer
Electrical and Electronics Engineering Dept., METU _____

Dr. Said Emre Alper
Technical Vocational School of Higher Education, METU _____

Date: 15.09.2010

I hereby declare that all information in this document has been obtained and presented in accordance with academic rules and ethical conduct. I also declare that, as required by these rules and conduct, I have fully cited and referenced all material and results that are not original to this work.

Name, Lastname: Ekrem Bayraktar

Signature:

ABSTRACT

DESIGN AND IMPLEMENTATION OF A MEMS BASED GRAVIMETRIC DETECTOR FOR CYTOMETRY APPLICATIONS

Bayraktar, Ekrem

M. Sc., Department of Electrical and Electronics Engineering

Supervisor: Assoc. Prof. Dr. Haluk Klah

September 2010, 140 pages

This thesis reports design and implementation of a MEMS based gravimetric resonator for cytometry applications. There are mainly two objectives of this thesis; to enable in-flow analysis and to perform closed loop operation that does not require any additional processing or equipment.

A novel MEMS based resonator with in-flow capabilities is proposed for detection of agents inside micro channels. High resolution of mass detection inside micro channels is planned to be succeeded with lateral motion in the micro channel floor. The idea embedding lateral resonators emerges from decreasing squeeze film damping during the motion of the resonator. Lateral motion is supported by hydrophobic parylene coating to decrease the damping.

Theory and design of the gravimetric resonators are explained and the fabrication flow is constructed and performed successfully by combining SOI, SOG and polymer micro fabrication techniques. Problems during the fabrication are overcome and optimized

flow is presented. The devices have a foot print area of $1.5 \times 0.5 \text{ cm}^2$ which is mainly composed of reservoirs for fluidic connections. Ten types of devices are designed according to their mass sensitivities and compliances. Trade offs between frequency, injected current, and compliance are analyzed successfully by taking also the performance parameters of the interface electronics in to account.

Test results reveal that single latex bead with $3 \text{ }\mu\text{m}$ diameter and 14.127 pg mass can be sensed successfully and mass sensitivity is measured to be 5.91 fg/Hz for this type of device.

Keywords: Gravimetric resonator, rare cell detection, oscillation, parylene, hydrophobic coating, damping, lateral motion, fabrication of suspended structures, cytometry.

ÖZ

SITOMETRİ UYGULAMALARI İÇİN MEMS TABANLI GRAVİMETRİK DUYARGA TASARIMI VE UYGULANMASI

Bayraktar, Ekrem

Yüksek Lisans, Elektrik ve Elektronik Mühendisliği Bölümü

Tez Yöneticisi: Doç. Dr. Haluk Külah

Eylül 2010, 140 sayfa

Bu tez, MEMS teknolojisine dayanan ve sitometri uygulamalarında kullanılabilir bir ataletsel rezonatörün tasarım ve uygulamasını anlatmaktadır. Çalışmada temel olarak, sıvı içinde analiz yapabilecek bir sistemin oluşturulması ve oluşturulan bu sistemin herhangi bir ekipmana veya ön analize ihtiyaç duymadan çalışabilmesi olmak üzere iki amaç hedeflenmiştir.

Mikro kanallar içinde, akış esnasında analiz yapabilecek, MEMS teknolojisine dayalı özgün bir rezonatör önerilmiştir. Mikro kanallar içinde yüksek çözünürlükte kütle analizi yapılabilmesi için yapıların kanal tabanında yanal hareketler yapması planlanmıştır. Yanal hareketli rezonatörlerin kullanılma amacı, rezonatörlerin hareketi esnasında oluşan sıkıştırma-sönümlenme kuvvetlerinin azaltılmak istenmesidir. Yanal harekete ek olarak hidrofobik parylene kaplama yapılması ve bu sayede sıkıştırma-sönümlenme kuvvetlerinin daha da azaltılması hedeflenmiştir.

Ataletsel rezonatörlerin teori ve tasarımlarından bahsedilip, üretim için SOI, SOG ve polimer üretim tekniklerini kullanarak oluşturulmuş olan üretim şeması verilmiştir. Üretim esnasında karşılaşılan problemler başarıyla aşılmış ve son üretim şeması sunulmuştur. Üretilen yapılar $1.5 \times 0.5 \text{ cm}^2$ bir alana oturuyor olup, bu alanın çoğunu akışkan bağlantı rezervuarları oluşturmaktadır. Kütle hassasiyetlerine ve yapı muvafakatlarına göre toplamda on çeşit yapı tasarlanmıştır. Tasarım yapılırken; salınım frekansı, çıkış akımı, ve yapı muvafakatı arasındaki etkileşimler arayüz devresinin çalışma parametreleri de göz önüne alınarak başarıyla analiz edilmiştir.

Test sonuçları, $3 \text{ }\mu\text{m}$ çapında ve 14.127 pg ağırlığında tek bir lateks boncuğun yapı üzerinde başarıyla algılandığını göstermiştir ve kütle hassasiyeti bu yapı için 5.91 fg/Hz olarak ölçülmüştür.

Anahtar Kelimeler: Ataletsel rezonatör, Ender hücre algılama, salınım, parylene hidrofobik kaplama, sönümlleme, yanal hareket, havada asılı yapıların üretimi, sitometri.

*To my family,
... and my love*

ACKNOWLEDGEMENTS

First of all I would like to thank my advisor Assoc. Prof. Dr. Haluk Külâh for his support and belief in my ideas during my studies. The encouragement and the research environment that he supplied helped me to complete my studies and taught me lots for my future career. I would also like to thank Prof. Tayfun Akın for contributions and supports during my studies. Thanks to TUBITAK (The Scientific and Technological Research Council of Turkey) for supporting my MS studies for two years.

I would like to express my gratitude to my colleague and good friend Gürkan Yılmaz not for his helps during my thesis work but also not leaving me alone during this journey any time I need him. The experiences that we shared in teaching labs, clean room environment, and in small vacations are invaluable and they all contributed deeply to my life that I will never forget. I also would like to thank other BioMEMS group members: Sertan Sukas (currently at University of Twente for his PhD research) for his advices and long discussions over my future career, Ata Tuna Çiftlik (currently at EPFL for his PhD research) for his contributions to the project and valuable suggestions, and Dr. İbrahim Sarı (currently at University of Southampton for his post doctoral research) for ideas over fabrication and advices, Deniz Erođlu for his helps during tests and simulations, Deniz Ertürkan, Dr. Yekbun Adıgüzel and Bilge Akbıyık for their contributions to the project during tests and supporting my work in different aspects, not to mention Ender Yıldırım, Hatice Ceylan, and Aziz Koyuncuođlu for their kindness, encouragements and contributions at my thesis work and also it was great experience to work in clean room with all of you. I would like to thank all other group members for their friendship and enjoyable research environment that we share all together.

There are lots of people in the clean room that I also should thank for their contributions: not to mention Orhan Akar and Dr. Kađan Topallı for discussions over fabrication and being elder brothers for me to listen and advice me, Dr. Said Emre Alper also contributed a lot to the project by questioning and giving advices during the fabrication,

thanks to him for joining long meetings about this project. Akın Aydemir deserves special thanks for his helps especially in STS Room and thank to him for turning the machines to 4' for my processes. There are also friends from RF MEMS group that helped me during my thesis and for being faithful friends to me: Çağrı Çetintepe, İlker Comart, Ozan Doğan Gürbüz, and other group members. I also give my appreciation to all other METU MEMS Research group members and all METU MET facility employees for their contributions; it was very entertaining to share this experience with all of you.

Special thanks to my love, Nilüfer Sayar, for her patience and support and not to forget her contributions on graphics of my thesis work. Thank you for being in my life and for your endless love.

Finally I want to express my thanks to my parents Eyüp and Yıldız Bayraktar for their endless love, encouragements and supporting me without questioning. They taught me to show patience over difficulties and their pray keep me walking on this way. My aunts, especially Saliha Sayın and Fatma Şahin, also deserve thanks for supplying me some delicious traditional foods. Not to forget my brothers Engin and Batuhan for their love, I wish we will not be separated forever.

TABLE OF CONTENTS

ABSTRACT	iv
ÖZ	vi
ACKNOWLEDGEMENTS	ix
TABLE OF CONTENTS	xi
LIST OF TABLES	xiii
LIST OF FIGURES	xiv
CHAPTERS	
1 INTRODUCTION.....	1
1.1 Micro Scale Detection and Separation Techniques.....	5
1.1.1 Mechanical Separation and Detection Techniques.....	6
1.1.2 Electrical Techniques	8
1.1.3 Chemical/Electrochemical Techniques.....	14
1.1.4 Optical Techniques	16
1.2 Gravimetric Techniques.....	19
1.3 Research Objectives and Motivation.....	31
2. THEORY & DESIGN	33
2.1 Theory of Micro Electromechanical Resonance:	34
2.2 Capacitive Electrostatic Actuation and Sensing	39
2.2.1 Electrostatic Capacitive Actuation	40
2.2.2 Electrostatic Capacitive Sensing	42
2.2.3 Electrical Equivalent Circuit of Gravimetric Resonator	44
2.3 Damping Analysis	48
2.3.1 Damping of a comb Drive Resonator:	50
2.4 Gravimetric Detection and Performance Parameters	52
2.4.1 Mass sensitivity in Gravimetric Resonators.....	54
2.5 Summary	55

3	DESIGN AND SIMULATION OF GRAVIMETRIC RESONATORS.....	56
3.1	Mechanical Structure of Gravimetric Resonator.....	57
3.1.1	Design of Spring Beams	59
3.1.2	Micro channel design and constraints.....	61
3.1.3	Design Parameters Summary	62
3.2	Simulations	64
3.2.1	FEM Analysis.....	67
3.2.2	Spice Analysis of Stray Capacitance on Resonance Behavior.....	68
3.3	Summary of Design and Simulation.....	69
4.	FABRICATION.....	71
4.1	Fabrication Techniques for Gravimetric Resonator	72
4.1.1	Dissolved wafer Process	72
4.1.2	SOI process:	73
4.1.3	SOG Process.....	74
4.2	Fabrication Steps of Gravimetric Resonator.....	75
4.2.1	1 st Generation Fabrication Flow	75
4.2.2	2 nd Generation Fabrication Flow	86
4.2.3	3 rd Generation Fabrication Flow.....	87
4.3	Summary.....	94
5.	TESTS AND RESULTS.....	95
5.1	Test Circuit and Setup	95
5.2	Open Loop Test Results.....	97
5.3	Mass Detection tests on Gravimetric Resonators.....	105
6.	CONCLUSION AND FUTURE WORK.....	108
	REFERENCES	111
	APPENDICES	
A.	DETAILED ANALYSIS OF SPRING-MASS-DAMPER SYSTEM.....	118
B.	COMSOL AND MATLAB SIMULATIONS OF GRAVIMETRIC RARE CELL DETECTORS	130

LIST OF TABLES

TABLES

Table 1.1 Advantages of Microfluidic Devices [5].....	3
Table 1.2 Prominent gravimetric techniques in the literature with their principles, quality factors, resonance frequencies, and mass sensitivities.	31
Table 3.1 COMSOL and MATLAB results for all device types.	70
Table 5.1 Simulation Results in COMSOL and MATLAB are compared with test results	99

LIST OF FIGURES

FIGURES

Figure 1.1 Research areas resulting from the integration of micro- and nano-scale systems and biomedical sciences [3].	2
Figure 1.2 Comparison of biological agent dimensions with micromechanical structures [4].	3
Figure 1.3 Schematic illustration of attachment of liposomes onto cantilever surface [9].	6
Figure 1.4 Cantilever stress change due to polymerization on the surface. (a) focus is on the substrate, (b) focus is on the cantilever tip [8].	7
Figure 1.5 RF characteristics for a transmission line type device. (a) fabricated device, (b) power losses, (c) S-parameters, (d) Phase changes [10].	9
Figure 1.6 Microfluidic devices and the experimental set up for impedance spectroscopy measurements. (a) Schematic drawing of the impedance measurement test setup. (b) Cell isolation and lysis. The lysed cells cause ion increase in the solution. (c) – (e) Different electrode layouts and device assembly [11].	10
Figure 1.7 (a) Fabricated device. (b) Return loss for (S11) on bare device compared with biotin and avidin treatment respectively [12].	11
Figure 1.8 (a) Permittivity comparison, (b) Conductivity comparison of healthy and patient cells for various frequencies. (c) SEM photograph of normal human peripheral blood cells, (d) SEM photograph of early (left) and late (right) apoptosis of patient human peripheral blood cells [13].	12
Figure 1.9 Schematic diagram of separation by dielectrophoretic forces (a) antibody immobilization, (b) DEP force applied to manipulate the target particles, (c) Washing out of non-targeted bacteria. (d) Results of detection during consecutive DEP trapping and washing processes [14].	13

Figure 1.10 (a) SEM image of the fabricated cantilever sensor array prior to deposition of sensor coatings. (b) Schematic setup to measure cantilever deflection with optical setup, readout and control units [16].....	15
Figure 1.11 Amperometric microfluidic device with PDMS cover, tubings and electrodes [17].	16
Figure 1.12 (a) Experimental setup of the proposed LSPR system with optics and biosensor, (b) LSPR absorbance data of the layers on the biosensor, (c) Effect of hybridization when probe oligonucleotids are immobilized on the LSPR biosensor surface [20].....	17
Figure 1.13 CTC isolating pillar type microfluidic device with experimental setup and captured cancer cell on the periphery of the microposts array [19].	18
Figure 1.14 SEM images of the integrated resonant piezoresistive cantilevers with the electromagnetic excitation schemes denoted. Parts (a) and (b) are the no. 1 and the no. 2 cantilevers, respectively. Part (c) shows measured amplitude–frequency properties of the no. 1 and the no. 2 cantilevers. The resonant frequency and the Q value for both the first and the second resonant modes are obtained [21].	20
Figure 1.15 Single Cantilever and frequency change after bacteria immobilization on to the cantilever surface [23].	21
Figure 1.16 Schematic diagram of living cantilever array. Target cells in suspension are captured and immobilized on the cantilever. Then the cells are cultured and the mass of a cell on a cantilever is measured <i>via</i> the resonance frequency shift of a cantilever [24].	22
Figure 1.17 Measured quality factors in air and DI water with theoretical calculations [25].....	23
Figure 1.18 Scanning electron micrograph (SEM) showing a cantilever beam with a single vaccinia virus particle and plot of resonant frequency shift after loading of a single virus particle [26].....	24
Figure 1.19 (a) Scanning electron micrograph (SEM) of a single <i>E. coli O157:H7</i> cell bound to the immobilized antibody layer on top of the oscillator. (b) The corresponding transverse vibration spectra of the cantilever due to the thermal and ambient noise before	

and after antibody immobilization and single cell attachment. (c) Measured frequency shift vs the number of bound E. coli cells for the $l = 15 \text{ um}$ and $w = 5 \text{ um}$. (d) $l = 25 \text{ um}$ and $w = 10 \text{ um}$ [28]..... 26

Figure 1.20 SEM photograph of electro thermally excited disk resonator with Wheatstone-bridge output signal around in-plane resonance frequency of disk resonator in air, in air after parylene coating, and in water [29]..... 27

Figure 1.21 (a) Diagram of interactions between target and probe molecules on cantilever beam which cause the deflection on the cantilever. (b) Cantilever deflection versus time for fPSA detection sensitivity against a background of 1 mg/ml of BSA [31]. 28

Figure 1.22 (a) SEM image of 1000 fg Pt deposited paddle, (b) experimental resonance frequency change before and after 1000 fg Pt deposition [32]. 29

Figure 1.23 Frequency shift after antibody immobilization and virus capture [35]. 30

Figure 2.1 Spring Mass Damper System..... 34

Figure 2.2 Parallel plates forming a capacitor and dimensions 41

Figure 2.3 Electrical model of the electromechanical resonator 48

Figure 3.1 Mechanical structure of the resonator showing comb finger and spring beam dimensions..... 57

Figure 3.2 Different spring arm designs (a) clamped-clamped beam structure, (b) crab leg design, (c) folded flexure design..... 60

Figure 3.3 Device code according to the geometrical parameters 64

Figure 3.4 Electromechanical Simulink[®] model of the gravimetric resonator. 65

Figure 3.5 Simulated transfer function of gravimetric resonator with device code 8015A 1F 20B..... 66

Figure 3.6 Simulated transfer function of gravimetric resonator with device code 4015A 2F 20B..... 66

Figure 3.7 First mode FEM analysis of device with code: 80 15A 1F 20B after including the undercuts and errors coming from lithography and etching, first harmonic at 450.24 KHz 67

Figure 3.8 Effect of stray capacitance on sensor performance 68

Figure 4.1: First generation fabrication flow for gravimetric resonator	77
Figure 4.2 Fabricated first generation gravimetric resonator with SEM photographs of micro channels and device structure	79
Figure 4.3 BHF (20 minutes 1:3 - HF:NH ₄ F) oxide etching and proof mass release process results. (a) Microscope is focused onto the top surface of the wafer, (b) Microscope is focused to the bottom and oxide islands are observed.	80
Figure 4.4 BHF (1:7 - HF:NH ₄ F) oxide etching photograph taken with Idonus IR microscope after 45 min. of etching.	81
Figure 4.5 Idonus IR microscope photograph of device after 48 % HF etching for 90 seconds.	82
Figure 4.6 Sidewall damage (SOI-notch) as a result of the destruction of directionality of SF ₆ ions due to the charged insulator surface at the bottom of a comb electrode array, a flexure beam, and a rectangular etch hole [72].....	83
Figure 4.7 DRIE Lag problem observed at etch holes.	84
Figure 4.8 Cr-Au layer broken during metal etch due to low adhesion onto parylene surface.	86
Figure 4.9 2 nd generation fabrication flow.	87
Figure 4.10 3rd generation fabrication flow	88
Figure 4.11 Metal residue on glass wafer prevents the bonding at this area. Light spectrum at this point shows that bonding is failed at this area.	91
Figure 4.12 Bonding photographs in microscope (a) device photograph, (b) bonding of alignment marks.....	92
Figure 4.13 PDMS channel fabrication flow	93
Figure 4.14 Device photograph with PDMS channels are bonded on top of devices	94
Figure 5.1 PCB photograph with TIA and amplifier stages.....	96
Figure 5.2 Test setup with sensor and test circuit.....	97
Figure 5.3 Effect of stray capacitance on sensor performance for device with code 16030A4F80B	98
Figure 5.4 Test results for devices with code 80 15A 1F 20B on the same die. (a) Magnitude responses, (b) phase responses after stray removal.....	100

Figure 5.5 Magnitude vs. frequency response for each device after stray removal	101
Figure 5.6 Bead attached to device with code 4015A2F20B	105
Figure 5.7 Test results for device 4015A2F20B (a) response of the device when there is not bead attachment, (b) response of the device when one latex bead is attached onto the surface of the proof mass.	106
Figure A.1 Amplitude attenuation of systems for differnt damping ratio.....	121
Figure A.2 Amplitude frequency relations for different damping ratios.	124
Figure A.3 Phase lag of forced vibrations for different damping ratios.	125
Figure B.1 First Mode of device with code 4015A1F20B at 608.16 KHz	130
Figure B.2 First Mode of device with code 4015A2F20B at 2.12 MHz.....	131
Figure B.3 First Mode of device with code 4015A2F40B at 626.57 KHz	131
Figure B.4 First Mode of device with code 8015A1F20B at 450.24 KHz	132
Figure B.5 First Mode of device with code 8015A2F40B at 475.02 KHz	132
Figure B.6 Second Mode of device with code 8015A4F40B at 1.10 MHz	133
Figure B.7 First Mode of device with code 8030A2F40B at 384.69 KHz	133
Figure B.8 Second Mode of device with code 8030A4F40B at 1.09 MHz	134
Figure B.9 Second Mode of device with code 16030A4F40B at 706.00 KHz	134
Figure B.10 Second Mode of device with code 16030A4F80B at 261.19 KHz	135
Figure B.11 Magnitude and Phase Response Simulation in MATLAB for device with code 4015A1F20B	136
Figure B.12 Magnitude and Phase Response Simulation in MATLAB for device with code 4015A2F20B	136
Figure B.13 First Mode of device with code 4015A2F40B at 626.57 KHz	137
Figure B.14 First Mode of device with code 8015A1F20B at 450.24 KHz	137
Figure B.15 First Mode of device with code 8015A2F40B at 475.02 KHz	138
Figure B.16 First Mode of device with code 8015A4F40B at 855.25 KHz	138
Figure B.17 First Mode of device with code 8030A2F40B at 384.69 KHz	139
Figure B.18 First Mode of device with code 8030A4F40B at 861.67 KHz	139
Figure B.19 First Mode of device with code 16030A4F40B at 387.00 KHz.....	140
Figure B.20 First Mode of device with code 16030A4F80B at 228.45 KHz.....	140

CHAPTER 1

INTRODUCTION

After the invention of transistor in early 1950s the miniaturization in the field of microelectronics gained speed year by year. The improvements in this area led to a new approach at early 1980s called micro electromechanical systems (MEMS) and the idea of combining miniature mechanic devices with the dedicated electronics interface and readout circuit is emerged.

Applications of MEMS spread on very different areas thereafter, inertial sensors for both military and commercial applications, vision systems, etc. One of the salient areas in the field of MEMS is biomedical technologies for life sciences. A new area, **Biomedical Micro Electro Mechanical Systems (BioMEMS)**, emerged to study micro mechanical structures for biomedical applications. **Figure 1.1** [3] shows a schematic of research areas resulting from integration of life sciences and biomedical disciplines with micro- and nano-scale systems.

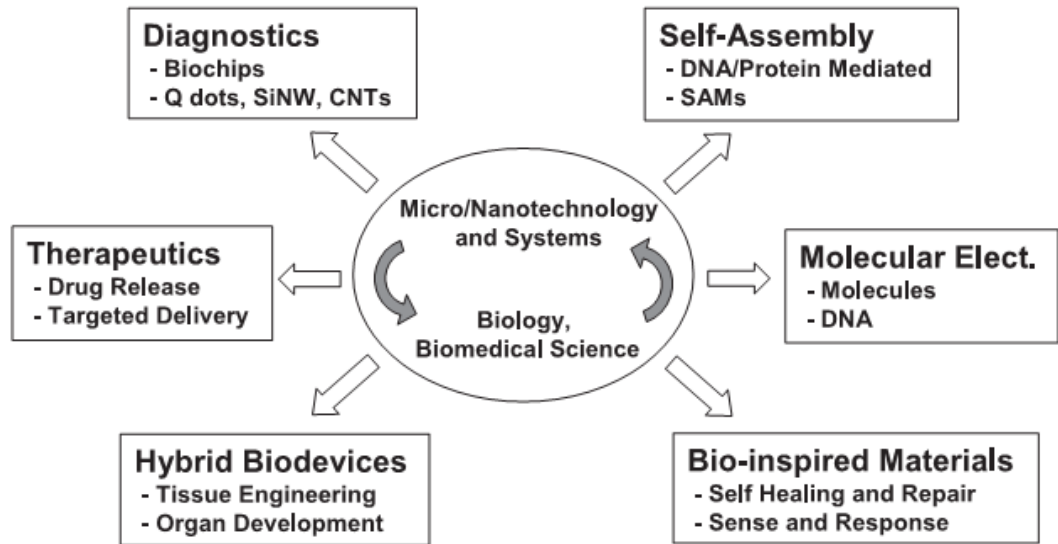


Figure 1.1 Research areas resulting from the integration of micro- and nano-scale systems and biomedical sciences [3].

With improved lithography techniques in micromachining, the minimum feature size of the fabricated structures are decreased. With this decrease in the dimensions of the micro structures it is possible to fabricate much smaller micro channels for bio analysis purposes. This technological down scaling enabled manipulation of micro to atto liter volumes of fluid. This amount of analyte usage comes with some advantages in terms of both analytical and economic viewpoints. Moreover, miniaturization in microfabrication techniques came up with the idea of designing mechanical structures that can effectively analyze the target species which has the dimensions of the microfabricated devices. A general diagram of the biological species and their scaling is given in **Figure 1.2** [4]. The idea of miniaturization put into action but one may ask the question if this approach is feasible or not? To investigate the feasibility and the logic behind the miniaturization we can investigate the advantages of microfluidic devices compared to the commercial macro devices. Some advantages of the microfluidic devices are given in **Table 1.1**.

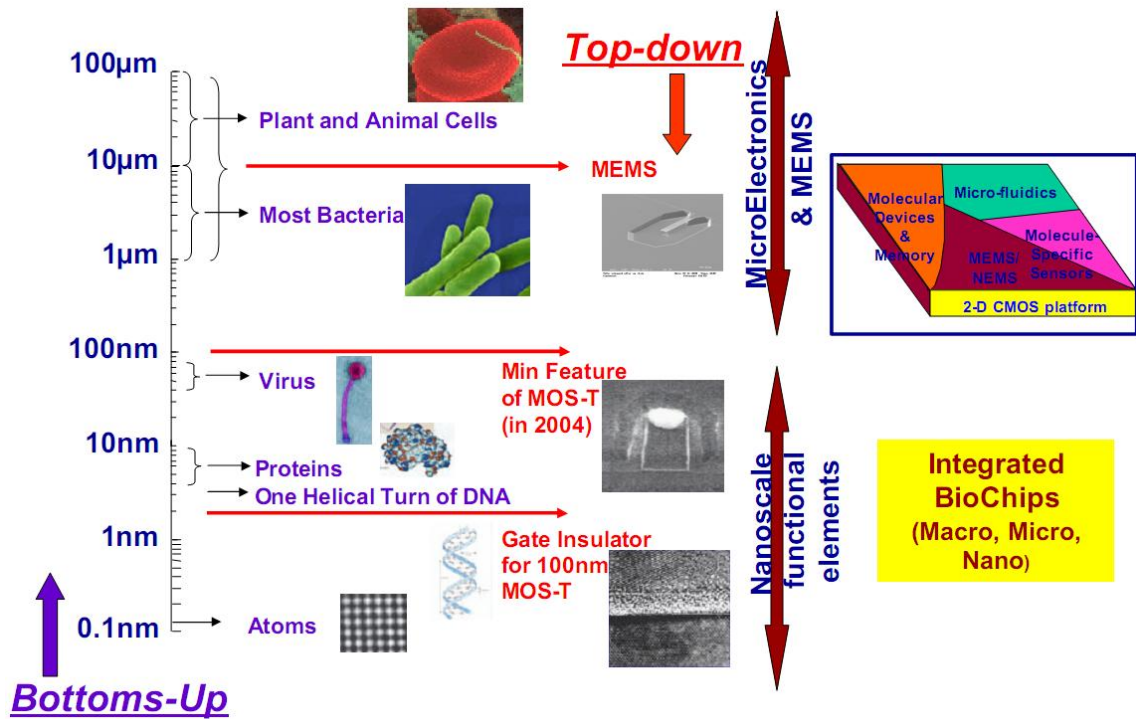


Figure 1.2 Comparison of biological agent dimensions with micromechanical structures [4].

Table 1.1 Advantages of Microfluidic Devices [5].

Microfluidic Advantages	Description
Less Sample and reagent consumption	Microfluidic devices typically require $10^2 - 10^3$ less sample volume than conventional systems. Hence the cost per analysis drops significantly.
Enhanced heat transfer	Higher surface area-to-volume ratio of microfluidic channels increases effective thermal dissipation.
Faster separations	Higher E-fields results in faster sample migration.
Safe experiments	Since chemical analytes are used in trace amounts, the possibility of damaging chemical reactions is very low.

Table 1.1 Continued.

In Vivo and In Vitro Usage	Microfluidic devices have the advantage of usage both in vitro and in vivo applications.
Improved Sensitivity	Miniaturization of the systems to the scale of the target molecules increases the sensitivity of microfluidic systems.
Reduced time	Small volumes of analytes enable higher concentrations that improve the experimentation time.
Laminar flow	Low Reynolds number flows reduce sample dispersion.
Electrokinetic manipulation	Electroosmotic flow enables fluid pumping with flat "plug-like" velocity profiles solely via applied E-fields.
Controllable	Fewer amounts of reagents controlled effectively during the experiments.
Lower power consumption	Fewer components and enhanced thermal dissipation require less power input.
Point of Care	Microfluidic devices enable point of care diagnostic applications.
Parallelization	Several assays can be "multiplexed", or run in parallel on a single chip.
Portability	System integration and reduced power allows for assays to be conducted using portable, hand-held device.

Biosensors find applications in areas of medicine, pharmaceuticals, food safety, environmental monitoring, homeland security, etc. due to their integrated, sensitive, and rapid analysis capabilities. With the increase in demand of such micro systems, the need for new materials in microtechnology also increased and polymer and material sciences became important branches of microtechnology industry. Parylene [6] and PDMS [7] are two important examples of this evolution that these materials are biocompatible, suitable for in vitro applications as well as in vivo studies.

Cell detection is one of the hot topics of state of the art biomedical micro technologies today. Detection of one cell inside millions will enable early diagnosis of diseases like cancer. The dimensions of the miniaturized biomedical devices will enable to capture and analyze one cell and pave the way for single molecule diagnosis.

This thesis reports a gravimetric rare cell detection analysis system to capture single cells on the resonating structures with a novel technique, on lateral resonators. The device will enable in-flow detection of cells and will be the replacement of conventional flow cytometry devices in the literature in near future. The ultimate goal is to detect cancer cells in the blood during the flow.

This chapter gives the necessary background information and literature search of the detection principles. Different micro scale techniques are discussed in Section 1.1 with their topologies advantages and disadvantages. Finally gravimetric related approaches are examined in detail and compared with the proposed system.

1.1 Micro Scale Detection and Separation Techniques

Micromechanical systems find large applications in biomedical microsystems. These miniaturized systems are used to separate or detect cells according to their dimensions, chemical or electrical properties. According to the sensing scheme microfluidic techniques can be separated to four categories; mechanical, electrical, chemical/electrochemical, and optics. Although optic systems are separated from other techniques, lots of the aforementioned techniques use also some optic setup for detection during their post processing. These techniques are examined by giving examples from the literature in next sections.

1.1.1 Mechanical Separation and Detection Techniques

Mechanical separation techniques use mechanical transduction techniques like surface stress change due to capturing of bioagents. The capture mechanism can be enhanced by a chemically modified surface or direct bonding of agents onto surface.

Coating the bio active surface with a pH sensitive layer and detecting the stress change by bending due to pH changes in the media is a reported technique in the literature [8].

Hyun et al. presented a piezoresistive cantilever sensor for detection of liposomes [9]. The cantilever surfaces are functionalized with chemically modified protein C2A which bonds to phosphatidylserine (PS) part of the liposomes. Bonding of liposome to the surface causes bending of the cantilever that produces electrical signals. **Figure 1.3** [9] shows binding of phosphatidylserine (PS) exposed liposomes to phosphatidylserine recognition protein C2A which is chemically immobilized on the gold surface of the cantilever sensor tips.

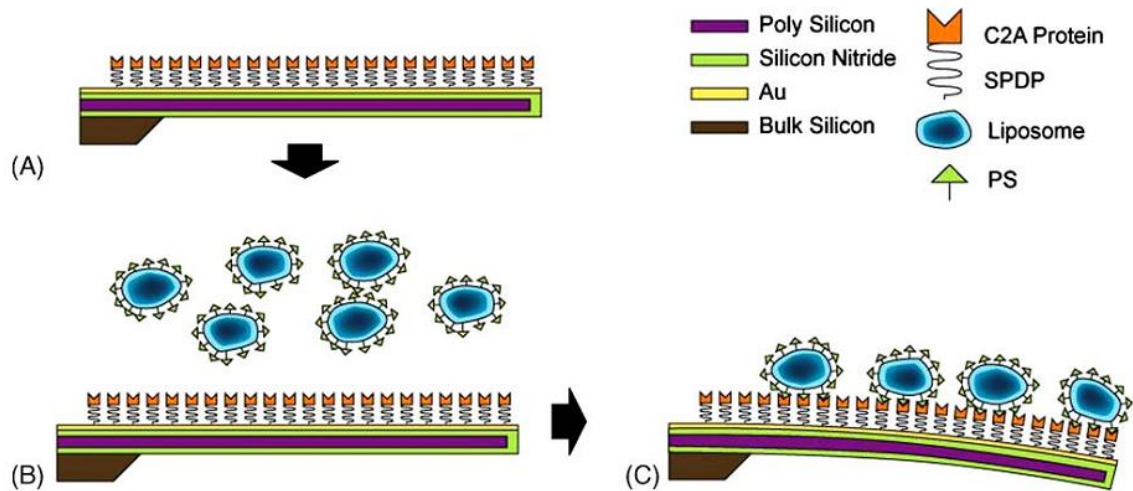


Figure 1.3 Schematic illustration of attachment of liposomes onto cantilever surface [9].

Hilt et al. used cantilevers as pH sensitive structures by coating cantilever surfaces with pH sensitive hydrogels [8]. A UV free-radical photolithography process was used to align and pattern hydrogels onto cantilever surfaces after cantilever structures are released. **Figure 1.4** [8] shows cantilever stress due to polymerization, the focus difference between cantilever tip and substrate shows that there is a deflection of 34.5 μm . When hydrogel film is polymerized, it adhered to the silicon substrate via organosilane coupling agent, but the film was inhibited from shrinking where it was bonded to cantilever surface. This effect results internal stress in the film. This situation causes errors during testing since the bending may result from the internal stress or stress change due to pH change in the media.

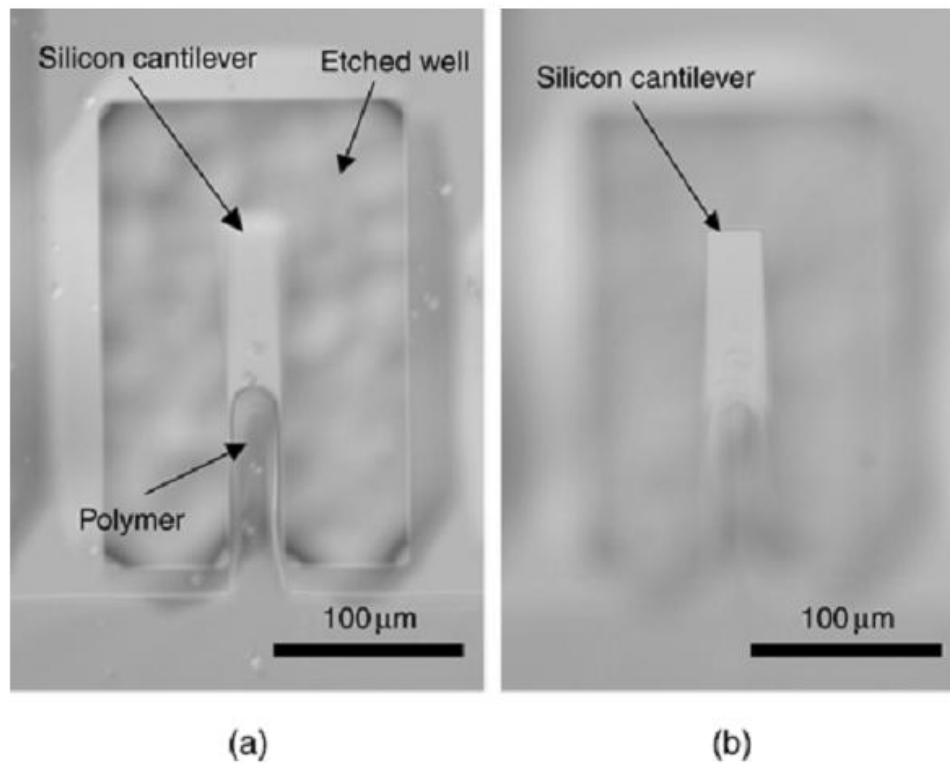


Figure 1.4 Cantilever stress change due to polymerization on the surface. (a) focus is on the substrate, (b) focus is on the cantilever tip [8].

1.1.2 Electrical Techniques

Electrical techniques exploit the change of conductance, impedance or RF matching parameters of the media of the analyte. Change of impedance parameters can be achieved by cell activation or by simply lysing the cells in the media. Using RF matching parameters and analyzing the power loss due to reflected power after agent capturing is another technique.

One of the interesting studies about label free detection is done by Kim et al. [10]. They used a transmission line as an inductive element and fabricated a capacitor by using silicon-based MEMS technology. They use skin effect theory on a micro stub. If a biomolecule, which has some electrical properties (dielectric constant, conductivity, electrical charging, and so on), is on the RF micro strip line, changes will happen in inductive or capacitive effect. They measure these changes to make perform label free detection. RF characteristics for a transmission line type device are shown in **Figure 1.5** [10]. A, B and C means no bio-treatment, after poly dimethyldiallyl ammonium chloride (PDAC) treatment, and after Glucose oxidase (GO_x) treatment, respectively. GO_x and PDAC are used as biomolecule target and probe.

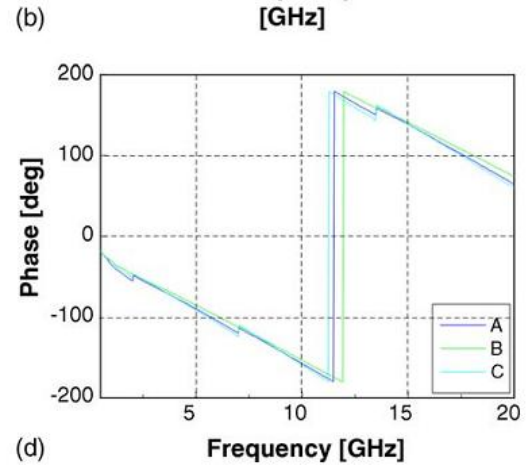
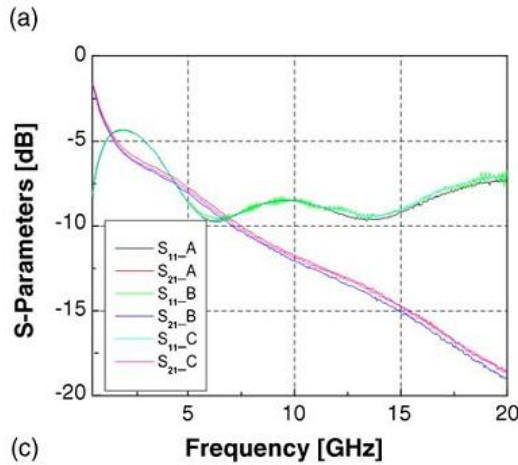
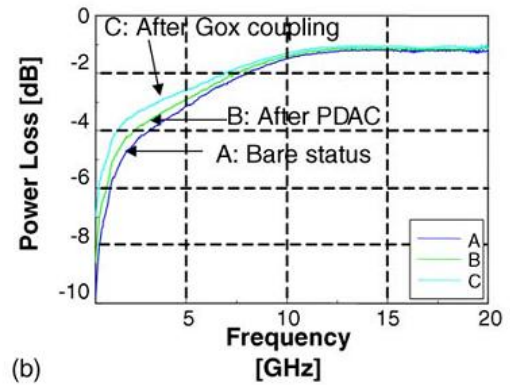
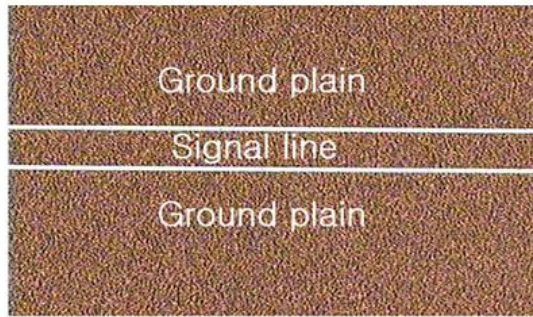


Figure 1.5 RF characteristics for a transmission line type device. (a) fabricated device, (b) power losses, (c) S-parameters, (d) Phase changes [10].

Cheng et al. used describe an electrical method for counting cells based on the measurement of changes in conductivity of the surrounding medium due to ions released from surface-immobilized cells within a microfluidic channel [11]. Immobilized cells are lysed using a low conductivity, hypotonic media and the resulting change in impedance is measured using surface patterned electrodes to detect and quantify the number of cells (**Figure 1.6**). However cell lysis is not a desired technique since the analyte cells will die after this process.

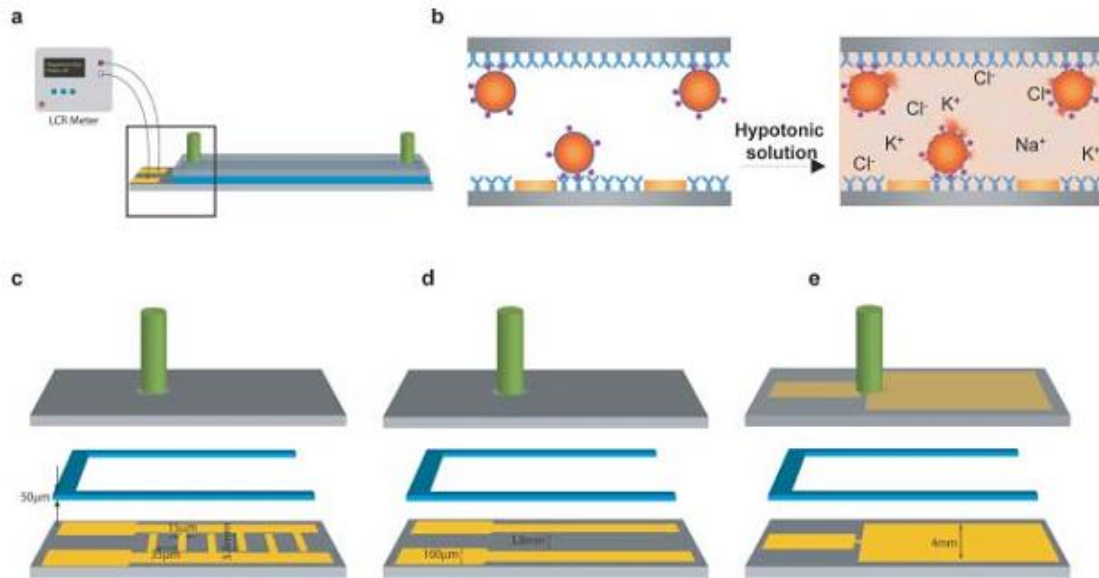


Figure 1.6 Microfluidic devices and the experimental set up for impedance spectroscopy measurements. (a) Schematic drawing of the impedance measurement test setup. (b) Cell isolation and lysis. The lysed cells cause ion increase in the solution. (c) – (e) Different electrode layouts and device assembly [11].

Kim et al. used another configuration like they use previously in the RF based MEMS sensor. They designed an LC resonator using micromachining techniques and tested for biomolecule detection [12]. They use smith charts for analysis, and confirm that the biomolecule acts as a resistance and the increased resistance of the resonator leads to the impedance matching change. The fabricated device and the return loss data for biotin and avidin treatment compared with the bare device is shown in **Figure 1.7** [12].

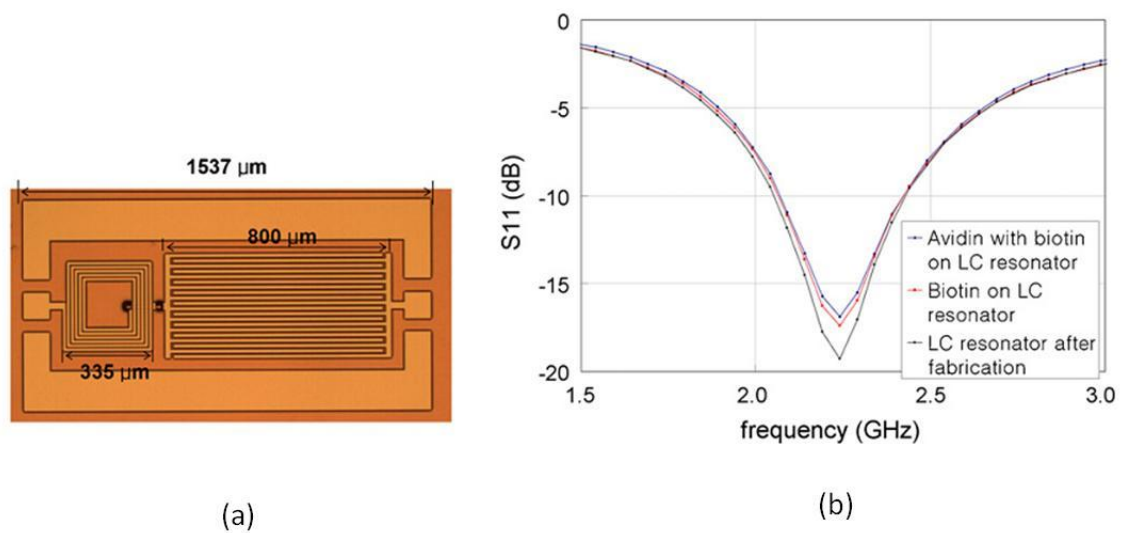


Figure 1.7 (a) Fabricated device. (b) Return loss for (S11) on bare device compared with biotin and avidin treatment respectively [12].

Kanapitsas et al. demonstrated a conductivity and permittivity measurement sensor for detecting apoptosis for Chronic Lymphocytic Leukaemia patients [13]. They exploit the different electrical properties of patient's B-chronic lymphocytic leukaemia (CLL-cells) and healthy cells. The real and imaginary parts of the dielectric permittivity and alternate field specific conductivity as a function of frequency are higher for patient's cells compared with the cells of healthy ones. **Figure 1.8** [13] (a-b) shows dielectric permittivity and conductivity measurements of the leukocytes for different frequencies. PBMC1 and PBMC2 are cells from healthy donors and CLL1 and CLL2 are cells isolated from two patients with the B-chronic lymphocytic leukemia. Figure 1.8 (c-d) also shows the SEM photograph of Normal Human peripheral Blood Cells and cells in early (left in (d)) and late (right in (d)) stage of Apoptosis.

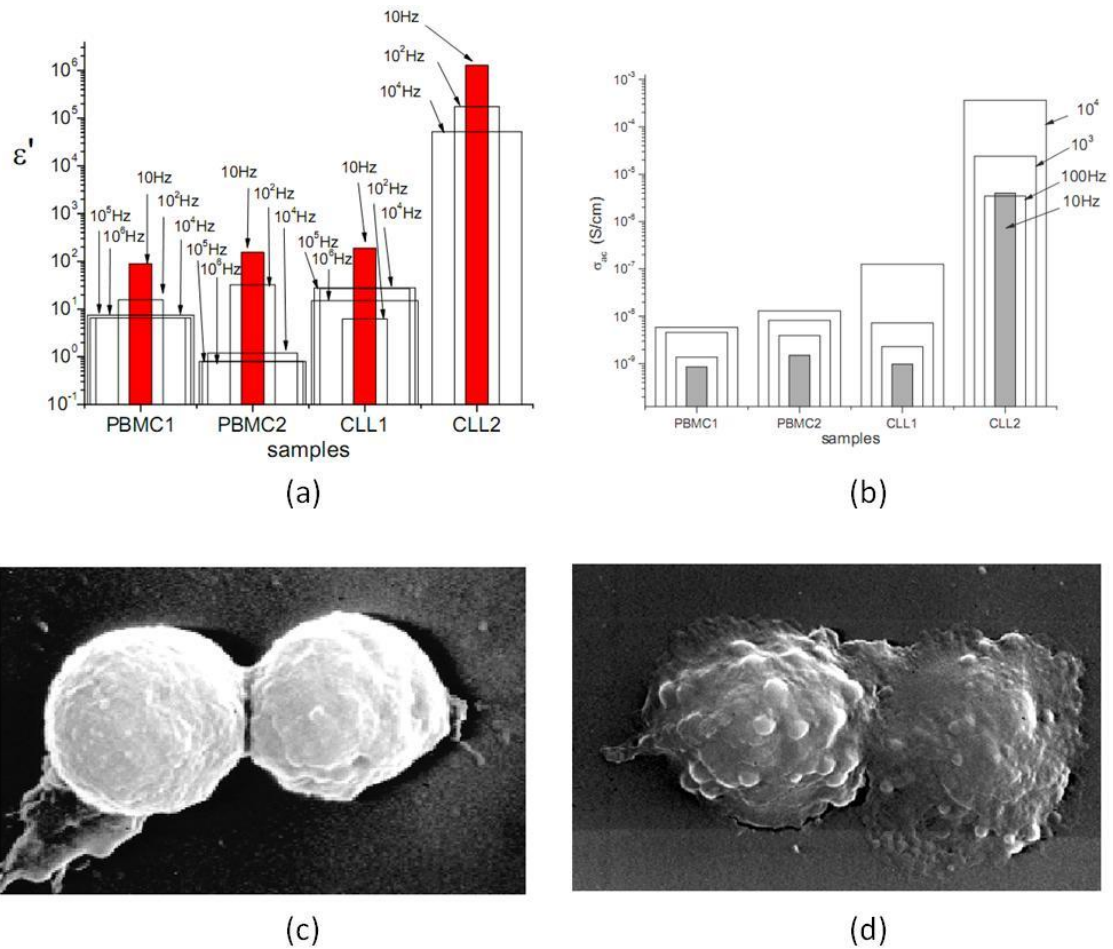


Figure 1.8 (a) Permittivity comparison, (b) Conductivity comparison of healthy and patient cells for various frequencies. (c) SEM photograph of normal human peripheral blood cells, (d) SEM photograph of early (left) and late (right) apoptosis of patient human peripheral blood cells [13].

Suehiro et al. used dielectrophoretic impedance measurement to detect bacteria (*Escherichia coli*) by adjusting the balance between DEP force and the drag force caused by the liquid flow [14]. They used positive dielectrophoretic forces to move the target bacteria between the interdigitated microelectrode array in the form of pearl-chains [15]. When target bacteria are pulled towards the gaps between interdigitated electrodes, the conductivity increases between the electrodes. **Figure 1.9** [14] shows schematic diagram

of DEP trapping and results of conductivity measurements after consecutive trapping and washing steps.

However, DEP trapping of particles cause large electric fields to be applied on particles and this large electric field may harm agents during the application.

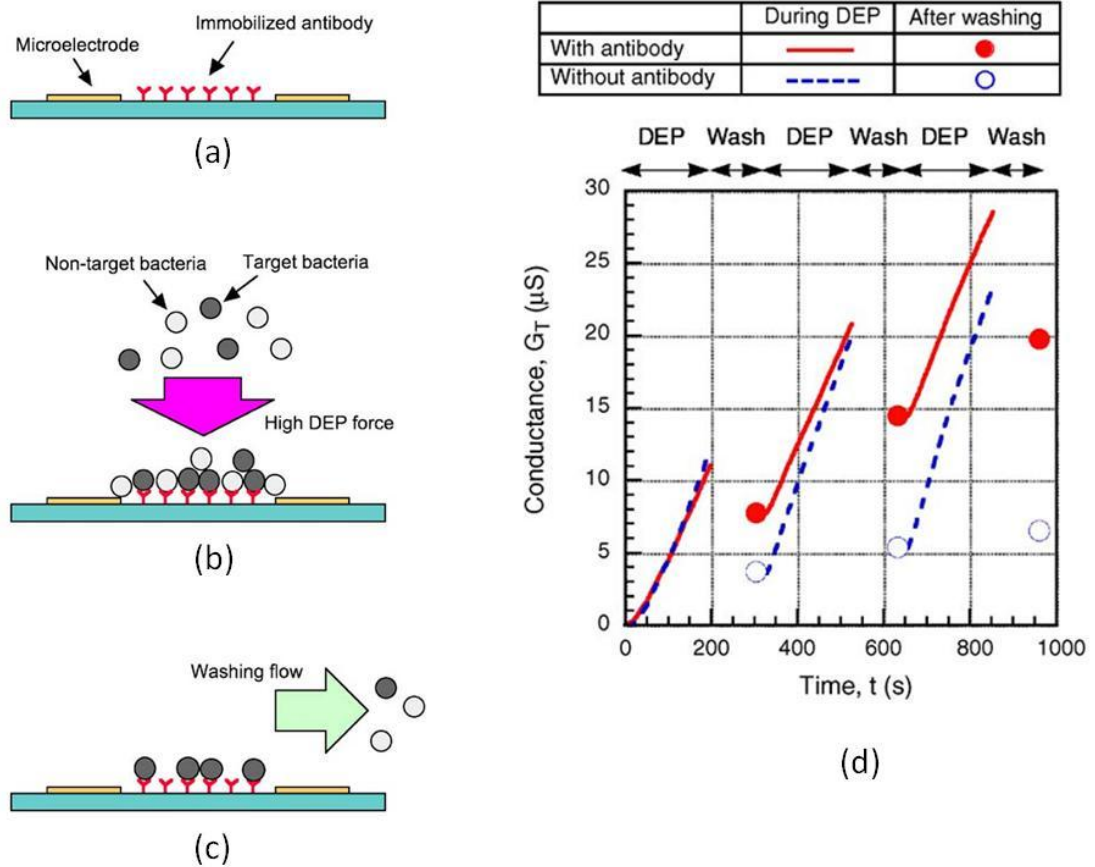


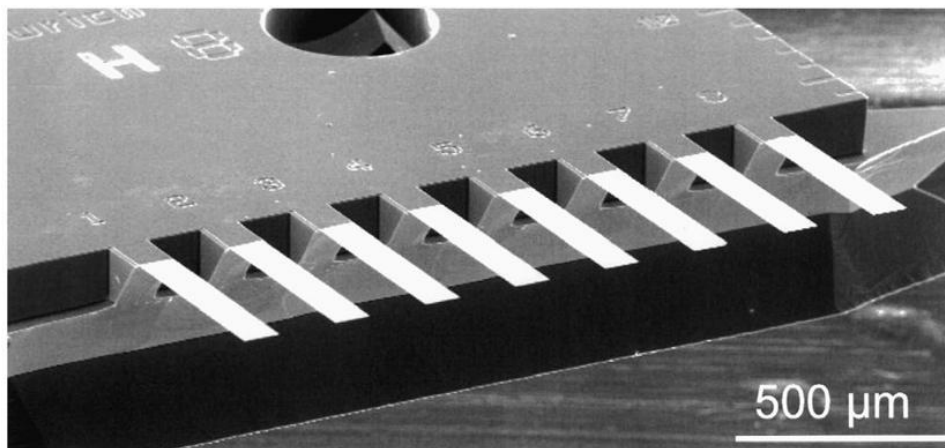
Figure 1.9 Schematic diagram of separation by dielectrophoretic forces (a) antibody immobilization, (b) DEP force applied to manipulate the target particles, (c) Washing out of non-targeted bacteria. (d) Results of detection during consecutive DEP trapping and washing processes [14].

1.1.3 Chemical/Electrochemical Techniques

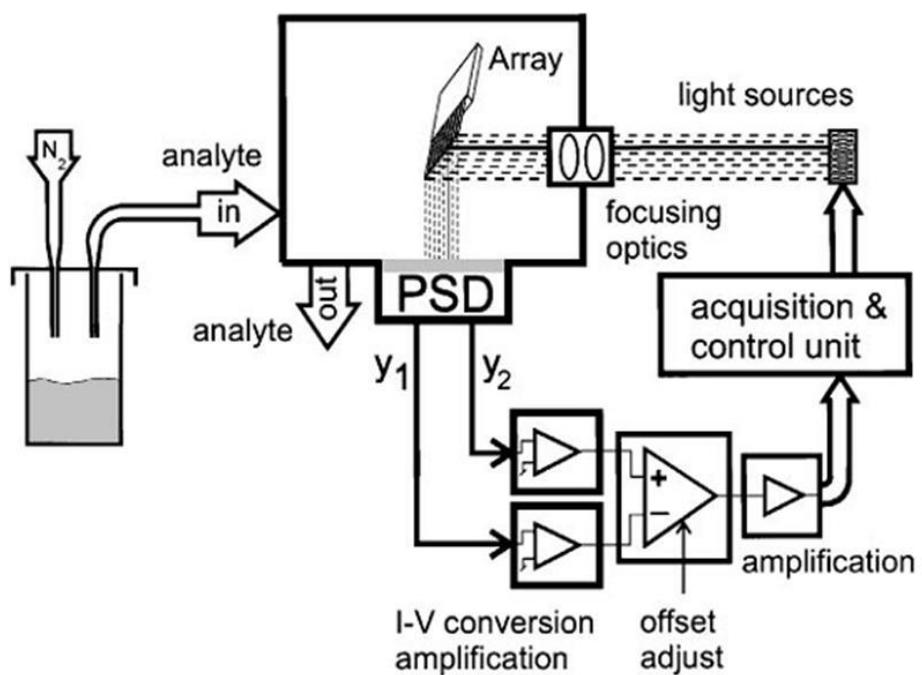
Amperometry, voltammetry, potentiometry, and coulometry are conventional macroscale techniques that are also tried to be adapted to microsystems. Chemical techniques use change of chemical constitution of the analyte media. There are studies that detect redox activities with amperometric techniques.

Baller et al. presented a cantilever sensor with optical readout by using cantilever arrays [16]. They use cantilever arrays as chemical noses by exploiting the swelling of the polymer on top of the cantilevers during exposure of the analyte. SEM image of cantilever arrays and experimental setup is shown in **Figure 1.10**. They need an acquisition and control unit to switch the light sources on and off via a time-multiplexing scheme. The laser light is directed via focusing optics onto the apex of the cantilevers of the array, then reflected and collected by a linear position sensitive detector (PSD). Using such a complex optical setup eliminates the advantages of miniaturization and adds additional cost to the detection system. The photocurrents from opposing electrodes are converted into voltages. The voltage difference is adjusted by an offset to allow optimal amplification and fed into the data acquisition and control unit. Data processing is performed off-line on a personal computer which prevents real time measurement.

Although there is a chemical actuation of the sensor, the technique that Baller et al. [16] used includes also mechanical and optical techniques.



(a)



(b)

Figure 1.10 (a) SEM image of the fabricated cantilever sensor array prior to deposition of sensor coatings. (b) Schematic setup to measure cantilever deflection with optical setup, readout and control units [16].

Amatore et al. demonstrated an electrochemical sensor that shows the release of reactive oxygen species (ROS) or reactive nitrogen species (RNS) [17]. They measure the production of ROS and RNS with amperometry at the surface of a platinized microelectrode. The used oxidative stress analysis device is shown in **Figure 1.11** [17].

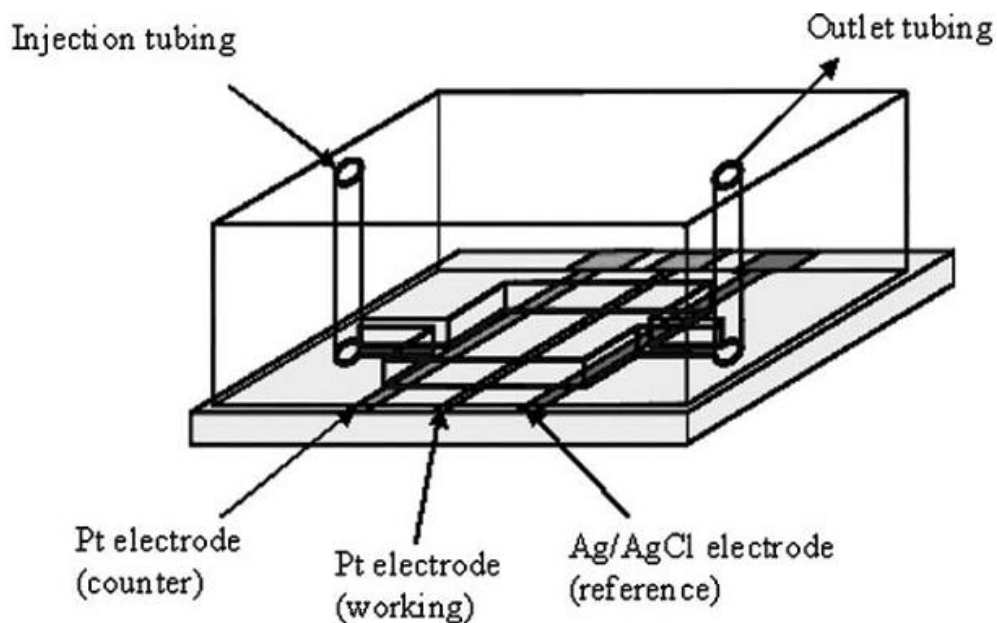


Figure 1.11 Amperometric microfluidic device with PDMS cover, tubings and electrodes [17].

1.1.4 Optical Techniques

DNA, protein, and cell detection are performed on the chip surfaces. They use fluorescent tags for detection and an optical setup consists of high precision microscopes and fluorescent sources are used. There are also studies exploiting the interferometry phenomena due to bioconjugate interactions as antibody/antigen, DNA hybridization and enzyme/substrate interactions [18]. Interferometry in biodetection systems relies on measuring the refractive index change to detect biological moiety on a sensitive film.

Endo et al. presented a localized surface Plasmon resonance (LSPR) based label-free optical biosensor [20]. They used peptide nucleic acids (PNA) to detect the target DNA related to tumor necrosis factor. PNA is used over a gold-capped layer and the optical properties of this layer are characterized through monitoring the changes in the absorbance strength as the thickness of the biomolecular layer increased with hybridization. **Figure 1.12** [20] (a) shows the experimental setup of the optic system and the sensor highlighting the structural layers on the sensor. **Figure 1.12** [20] (b) shows the absorbance of each layers on the sensor. The immobilization of probe oligonucleotids on the sensor and effect of hybridization are show on **Figure 1.12** [20] (c).

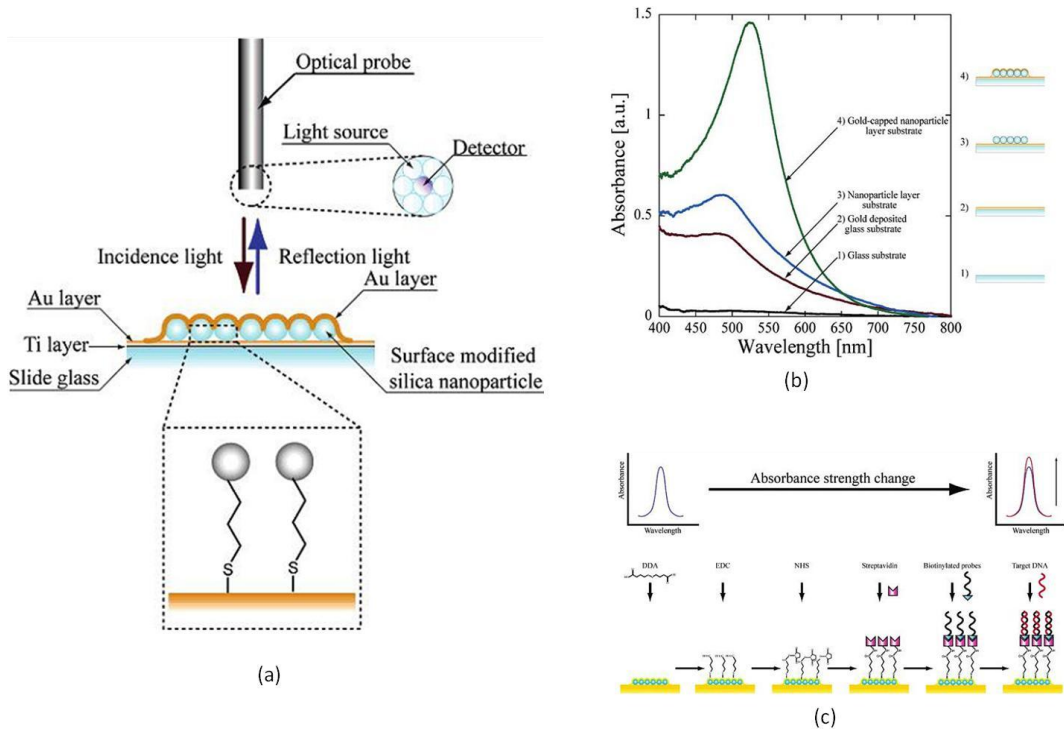


Figure 1.12 (a) Experimental setup of the proposed LSPR system with optics and biosensor, (b) LSPR absorbance data of the layers on the biosensor, (c) Effect of hybridization when probe oligonucleotids are immobilized on the LSPR biosensor surface [20].

Nagrath et al. presented a cancer detection system with optical setup [19]. Although they make successful experiments on capturing and detecting tumor-derived epithelial cells in blood from patients with cancer, they use a post processing optical experimental setup which destroys the real time measurement possibility. Antibody coated microposts are used as capturing mechanism to capture CTCs in the blood. The microfluidic platform does not require a pre-labeling or processing which is the main advantage of the system. They performed analysis on different cancer types including lung, prostate, pancreas, breast, and colon and identified CTCs for these cancer types. **Figure 1.13** [19] shows isolation of the cancer cell on the periphery of the microposts with experimental setup.

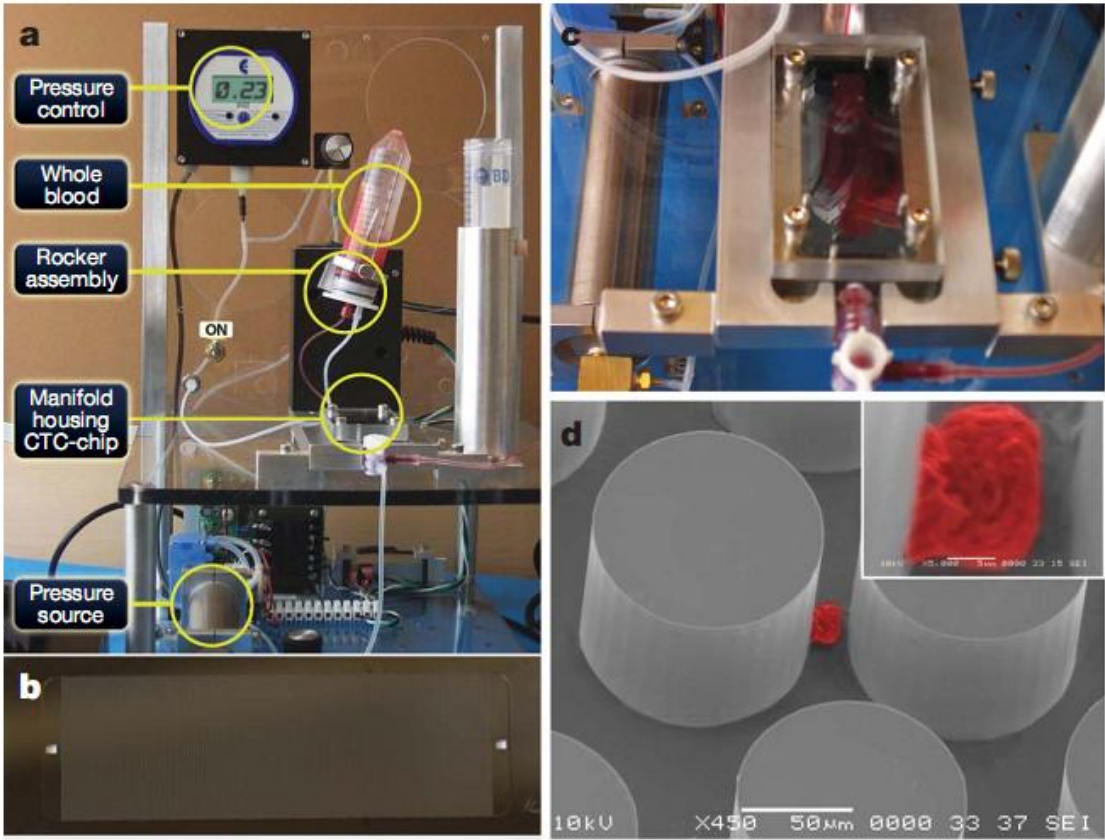


Figure 1.13 CTC isolating pillar type microfluidic device with experimental setup and captured cancer cell on the periphery of the microposts array [19].

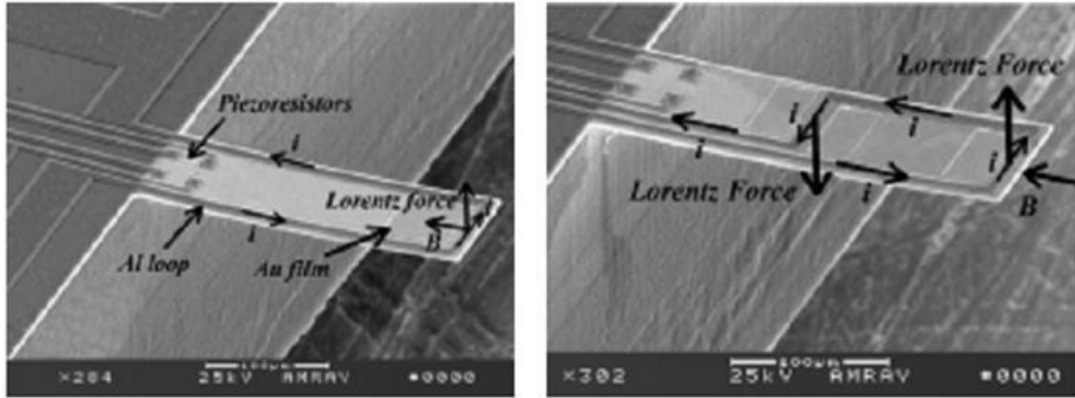
1.2 Gravimetric Techniques

Gravimetric detection technique basically relies on the change of resonance frequency of moving structure, which depends on the spring stiffness and total oscillating mass. When a mass is loaded over the moving structure, the frequency of resonance changes since there is no change in the spring constant of the system (theoretically).

In the literature there are different techniques that exploit this resonance change when a mass is loaded over them. The most common technique in the literature is to use cantilevers. Cantilevers are also used in different ways to exploit resonance phenomena.

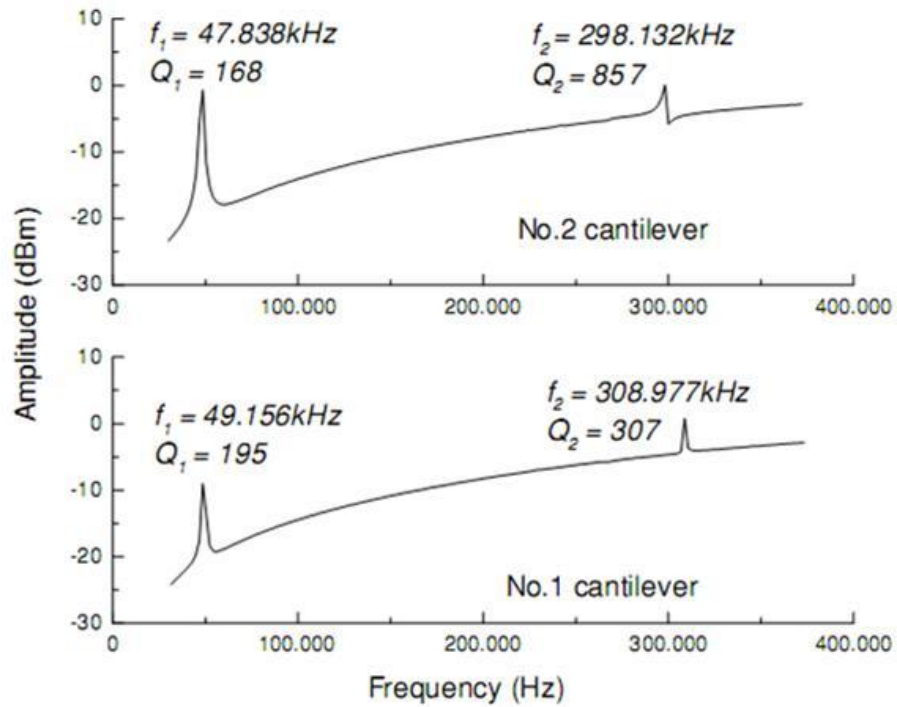
Cantilevers are used with piezoresistive materials for detection. Jin, Li et al. used cantilevers with piezoresistive materials to detect resolvable mass in the air [21]. Both a piezoresistive bridge and a metal coil are integrated in the cantilever for signal sensing and Lorentz-force resonance excitation, respectively. **Figure 1.14** [21] shows both SEM image of the fabricated cantilevers with piezoresistors on them including the effective forces and frequency response of the shown cantilevers.

Dauksaite et al. propose a system using the piezoresistive cantilever biosensor, they can sense the static surface stress that arises when the analytes (the protein) interact specifically with receptor molecules immobilized on the upper cantilever surface [22].



(a)

(b)



(c)

Figure 1.14 SEM images of the integrated resonant piezoresistive cantilevers with the electromagnetic excitation schemes denoted. Parts (a) and (b) are the no. 1 and the no. 2 cantilevers, respectively. Part (c) shows measured amplitude–frequency properties of the no. 1 and the no. 2 cantilevers. The resonant frequency and the Q value for both the first and the second resonant modes are obtained [21].

Gupta et al. show detection of bacteria on the cantilevers with the help of resonance frequency change [23]. The detected bacterium at this work is *Listeria*. *Listeria* bacteria have a cylindrical shape with dimensions of length around 0.5–2 μm and width of around 0.4–0.6 μm . They assume that the density of a bacterial cell is slightly higher than that of water, ($\sim 1.05 \text{ g/cm}^3$) with length of 2 μm and width of 0.4 μm , and that around 70% of the cell mass is due to water. They calculate the dry mass of the bacteria by simply assuming that the water portion of the mass is just lost during drying process and calculate the dry mass of the cell as 79 fg. Drying the cells and making such assumptions considerably decrease the reliability of the sensors. By using this result they assume that the calculated mass change is very close to measured mass change which is 85 fg. Scaling down the cantilever beam dimensions will not solve the problem since the standard deviation will be high and the results will lose their accuracies. **Figure 1.15** [23] shows the released single cantilever and shift of the frequency due to bacteria stiction onto the cantilever surface. Although thinning the cantilevers further will increase the sensitivity, releasing thinned cantilevers require very sensitive critical point drying (CPD) steps to prevent the stiction of the cantilevers.

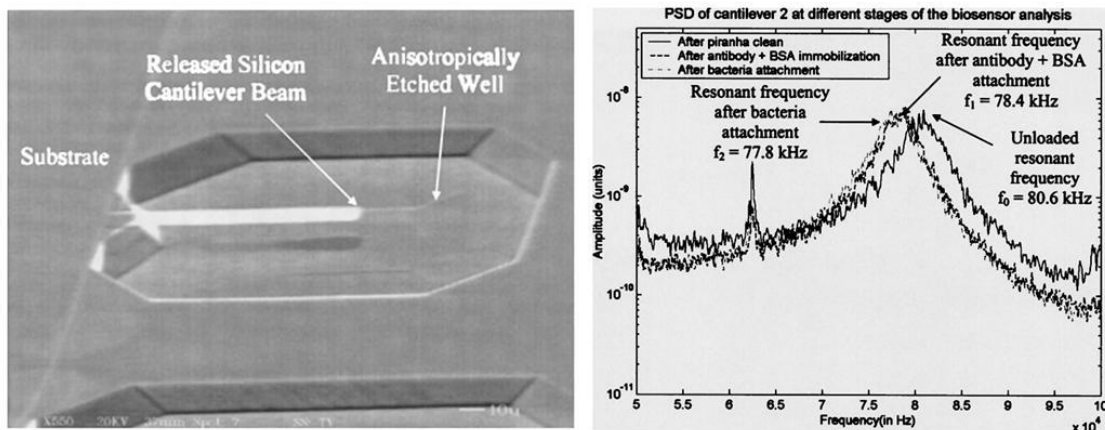


Figure 1.15 Single Cantilever and frequency change after bacteria immobilization on to the cantilever surface [23].

Park et al. demonstrate a new platform for the mass measurement and optical observation of single cells using cantilever arrays. These cantilever arrays are encapsulated with PDMS to form the micro channels as shown in **Figure 1.16** [24]. HeLa cells were captured on the functionalized cantilevers with positive dielectrophoresis, and cultured on the cantilevers for up to 7 days before measuring the resonance frequencies of the cantilevers. However, 7 days for detection and using optical setup after such a long incubation time prevents online monitoring of the cell attachment. Although the sensors cost a little with batch production on Si wafers, using an optical setup costs quite much which contradicts with the aims of the miniaturization.

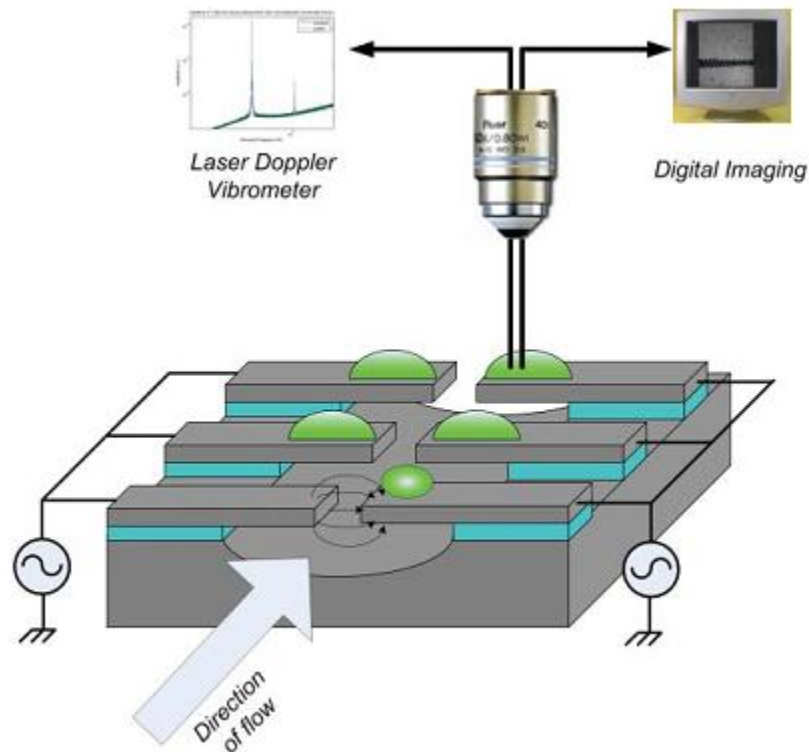


Figure 1.16 Schematic diagram of living cantilever array. Target cells in suspension are captured and immobilized on the cantilever. Then the cells are cultured and the mass of a cell on a cantilever is measured *via* the resonance frequency shift of a cantilever [24].

Davila et al. demonstrate the use of microcantilevers as resonant mass sensors for detection of *Bacillus anthracis* Sterne spores in air and liquid [25]. Mass detection is observed via Laser Doppler vibrometer technique which is again requires an optical setup. They demonstrate that as few as 50 spores on the cantilever can be detected in water using the thermal noise as excitation source. Measurement sensitivity of 9.23Hz/fg for air and 0.1Hz/fg for water were obtained. Decrease of the quality factor can be observed in **Figure 1.17** [25] since the damping is high in the water. Especially squeeze film damping is very effective when cantilevers are used in vertical direction. This squeeze film damping effectively reduces the quality factor in the liquid media and hence prevents in flow detection.

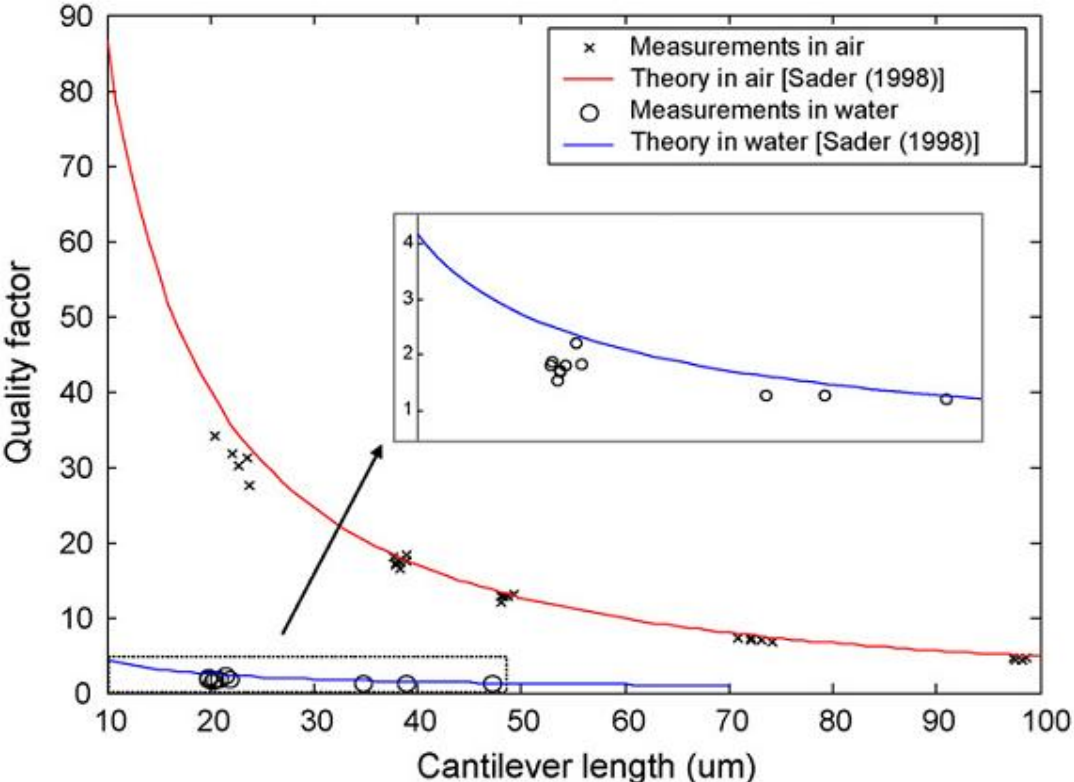


Figure 1.17 Measured quality factors in air and DI water with theoretical calculations [25]

Virus detection and catching by using cantilevers are also studied in the literature. Gupta et al. showed single virus detection by using cantilever resonators [26]. They have demonstrated the detection of a single vaccinia virus particle with an average mass of 9.5 fg. However, the measurement of the cantilever resonant frequency was performed using a microscope scanning laser Doppler vibrometer (MSV-300 from Polytec PI). Loaded cantilever and change of the frequency after loading is observed in **Figure 1.18** [26].

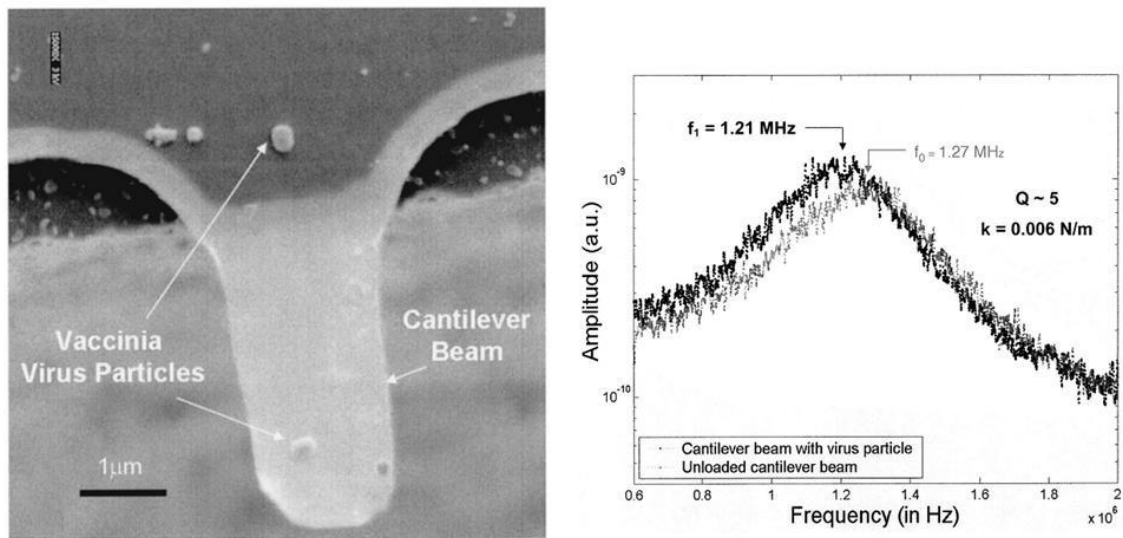


Figure 1.18 Scanning electron micrograph (SEM) showing a cantilever beam with a single vaccinia virus particle and plot of resonant frequency shift after loading of a single virus particle [26].

Gupta et al. were first cleaned the cantilevers beams in a solution of (H₂O₂:H₂SO₄51:1), rinsed in DI water, immersed in ethanol, and dried using CPD. The frequency spectra was then measured in order to obtain the “unloaded” resonant frequencies of the cantilever beams. Next, purified vaccinia virus particles at a concentration of $\sim 10^9$ PFU/ml in DI water were introduced over the cantilever beams

and allowed to incubate for 30 min, following which the cantilever beams were rinsed in ethanol and dried using CPD. The resonant frequencies of the cantilever beams were then measured again in order to obtain the “loaded” resonant frequencies. Loading the cantilevers and drying them again will cause some stress change on the cantilever structures since the cantilevers are nano meter thick. This internal stress will worsen the performance of the sensors which will degrade the resolution. It is shown that the deposited material can change cantilever mechanical properties, like stiffness. It was observed that water adsorption on a gelatin coated cantilever causes an increase of its resonance frequency [27], which is contradiction with the effect of the mass increase. This crosstalk between mass and stiffness changes can be minimized when the sensing layer is concentrated at the free end of the cantilever, but this time side specific adsorption is required. Unless the tip of the cantilever is not the only adsorption point, it is not possible to determine the added mass amount onto the cantilever which means that the resolution is lost.

There are also some studies on pathogenic bacteria that exploit the resonance of the cantilevers. Ilic et al presented a resonant frequency-based mass sensor, comprised of low-stress silicon nitride cantilever beams for the detection of *Escherichia coli* (*E. coli*)-cell-antibody binding events with detection sensitivity down to a single cell [28]. The ambient noise due to temperature prevents to determine the resonance frequency and hence the resolution is lost. SEM picture of a single *E. coli* on the cantilever is shown in **Figure 1.19** [28] with frequency shifts for number of cells for different cantilever dimensions.

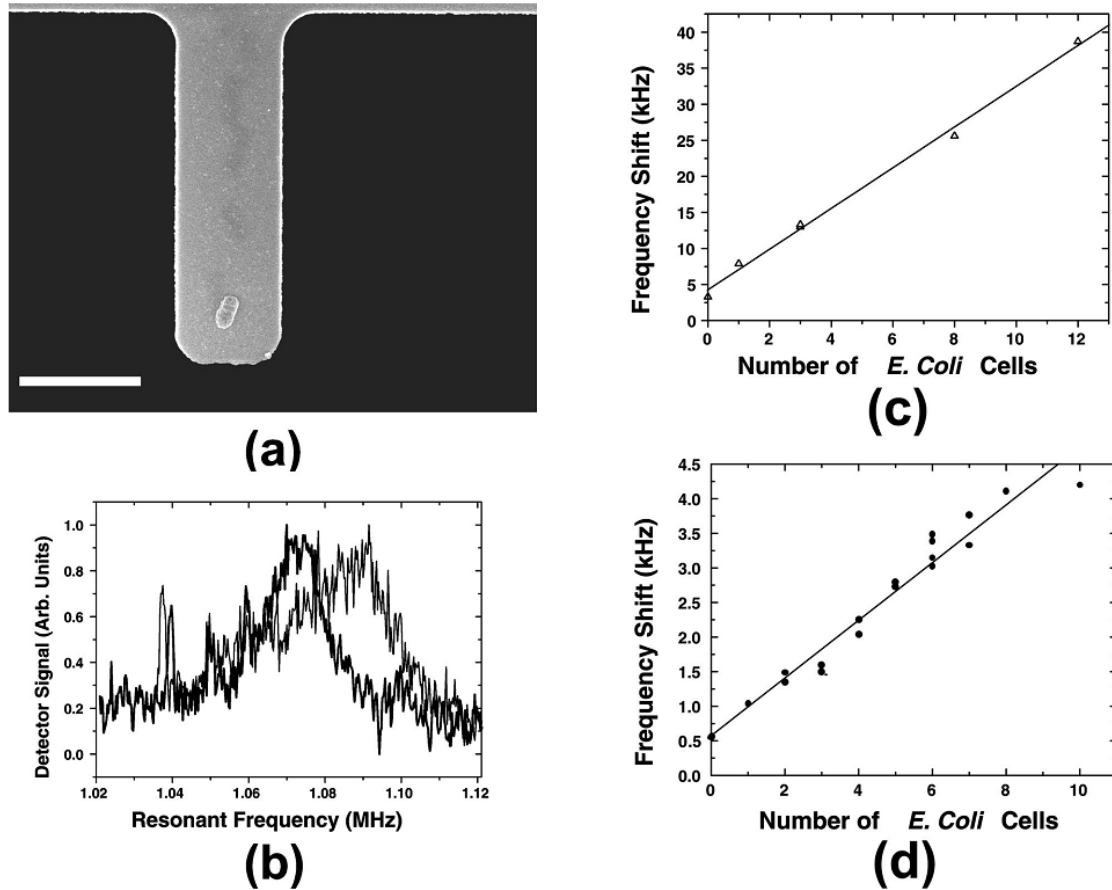


Figure 1.19 (a) Scanning electron micrograph (SEM) of a single *E. coli* O157:H7 cell bound to the immobilized antibody layer on top of the oscillator. (b) The corresponding transverse vibration spectra of the cantilever due to the thermal and ambient noise before and after antibody immobilization and single cell attachment. (c) Measured frequency shift vs the number of bound *E. coli* cells for the $l = 15 \mu\text{m}$ and $w = 5 \mu\text{m}$. (d) $l = 25 \mu\text{m}$ and $w = 10 \mu\text{m}$ [28].

One of the most interesting articles in chemical and biological sensing in gaseous and liquid environment is presented by Seo et al. in 2008 [29]. They use disk-shape microstructure operated in a rotational in-plane mode with typical resonance frequencies between 300 and 1000 kHz. Although they do not give any frequency change data due to mass loading, the study is designed for biological sensing application. **Figure 1.20** [29] shows the SEM picture of the proposed disk resonator and quality factor in air and water

after parylene coating. However, the geometry of the disk resonator does not allow using the resonator inside a microfluidic channel. Moreover, the resonator cannot catch the cells or bio analytes easily since the bioactive site is very small (cross point of the resonator) and there is not any mechanism that guides the analytes onto the bioactive site.

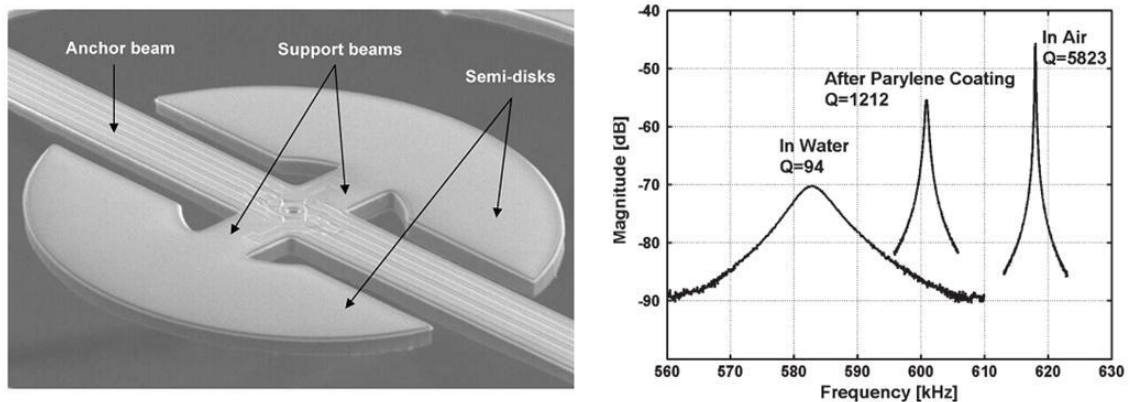
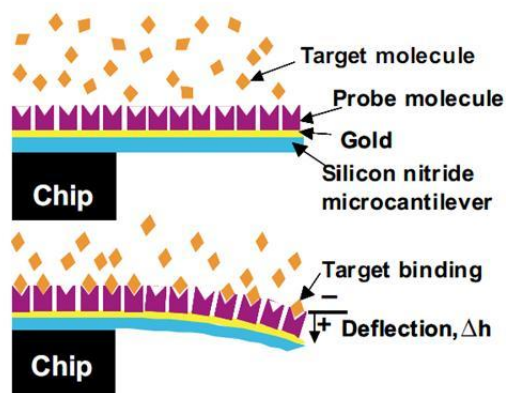


Figure 1.20 SEM photograph of electrothermally excited disk resonator with Wheatstone-bridge output signal around in-plane resonance frequency of disk resonator in air, in air after parylene coating, and in water [29].

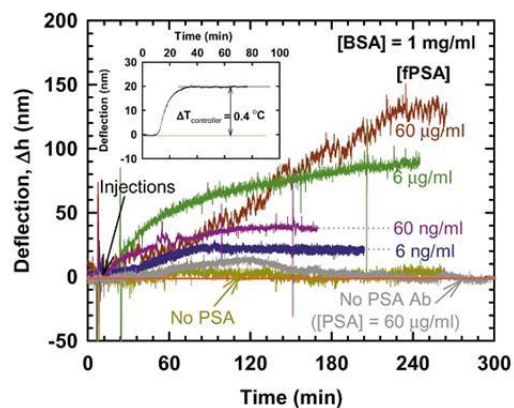
Lee et al. presented a thin film cantilever composed of $\text{SiO}_2/\text{Ta}/\text{Pt}/\text{PZT}/\text{Pt}/\text{SiO}_2$ on a SiN_x supporting layer for simultaneous self-exciting and sensing [30]. They present the resonant frequency change of piezoelectric microcantilevers due to a combination of mass loading and spring constant variation arisen from antigen-antibody interaction of C-reactive protein (CRP).

Wu et al. exploited bending of the cantilevers due to intermolecular nanomechanics due to specific biomolecular binding on the surface of the cantilever [31]. They try to detect PSA in a background of human serum albumin (HSA) and human plasminogen (HP). **Figure 1.21** [31] shows alteration of intermolecular nanomechanical interactions within a

self-assembled monolayer on one side of a cantilever beam due to specific biomolecular interactions between target and probe molecules and experimental result that gives the deflection of the cantilever with time for fPSA detection. The temperature change during the detection will directly affect the deflection magnitude which will cause stress noise during the measurements.



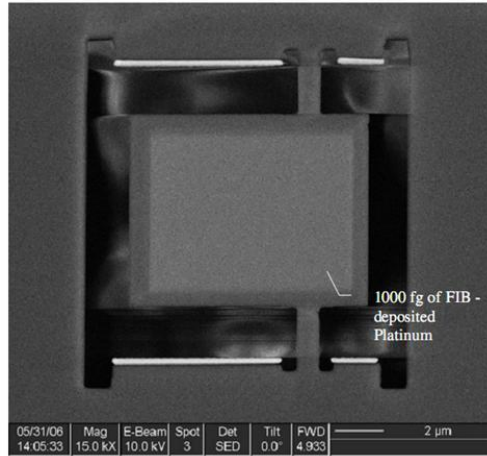
(a)



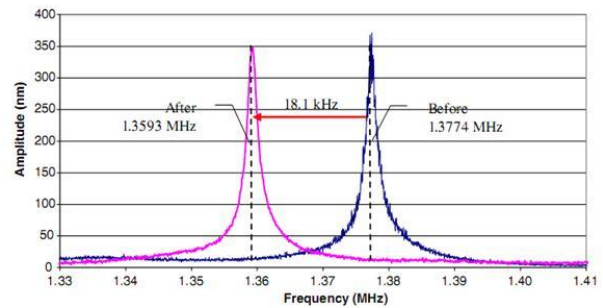
(b)

Figure 1.21 (a) Diagram of interactions between target and probe molecules on cantilever beam which cause the deflection on the cantilever. (b) Cantilever deflection versus time for fPSA detection sensitivity against a background of 1 mg/ml of BSA [31].

Boonliang et al. represented a thin membrane resonator for mass detection but used laser vibrometer for frequency characterization [32]. The fundamental mode of their sensor is torsional which causes some nonlinearity during the operation. The paddle with an added mass of 1000 fg produced a shift in the resonant frequency curve which is shown in **Figure 1.22** [32].



(a)



(b)

Figure 1.22 (a) SEM image of 1000 fg Pt deposited paddle, (b) experimental resonance frequency change before and after 1000 fg Pt deposition [32].

Lee et al. presented a micromachined PZT thin film cantilever for detection of C-reactive protein [33]. They exploit resonance frequency shift for label free detection of C-reactive protein (CRP).

There are also membrane like structures in the literature. Alava et al. presented a silicon-based micro-membrane with piezoelectric actuation and piezoresistive detection for sensing in the liquid [34]. They reached quality factors of 417 in the liquid but did not make any detection on these sensors. The maximum quality factor obtained is measured in DI water and detection related tests are not performed in this study. They used an electronics interface to increase the quality factor.

Gupta et al. used cantilevers in another study to detect virus particles on the cantilever surfaces [35]. **Figure 1.23** [35] shows the test results that show the frequency shift after antibody immobilization and virus capturing.

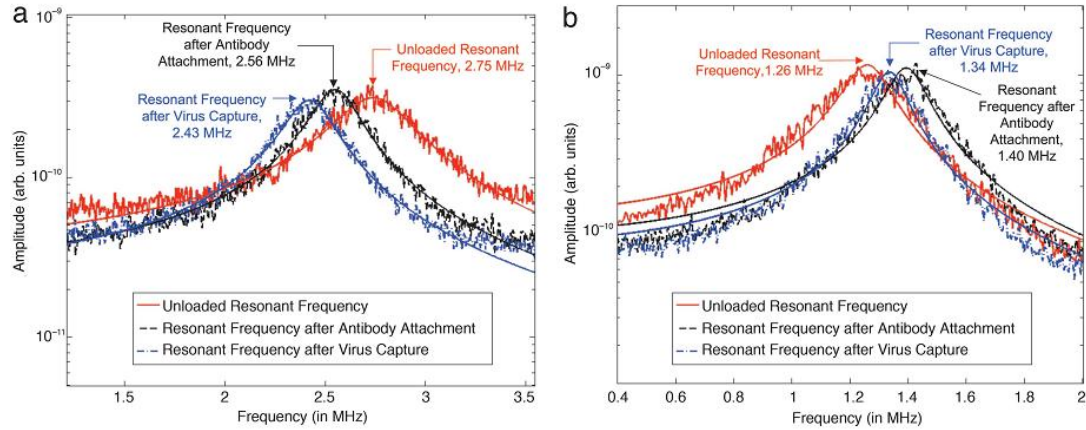


Figure 1.23 Frequency shift after antibody immobilization and virus capture [35].

Different gravimetric techniques are presented and prominent works in the literature are given in **Table 1.2** with their mechanism and sensitivities. The works in the literature either use cantilevers as the mechanical moving structures or use other disk shapes for gravimetric detection. However, cantilevers are not suitable for in-flow detection of agents inside the fluid and also damping is very high since the motion of the cantilever squeezes the fluid. Disk-like shapes have advantages but micro-channel structures are not well suited for these types of devices.

Table 1.2 Prominent gravimetric techniques in the literature with their principles, quality factors, resonance frequencies, and mass sensitivities.

Group	Principle	Quality Factor		Resonance Frequency	Mass Sensitivity
		Air	Water		
Jin, Li et al. [21]	Resonance Piezoresistive	307 to 857	----	---	0.17 pg to 0.06 pg
Gupta et al. [23]	Resonance	56	----	85.6 KHz	65 Hz/pg
Ilic et al. [28]	Resonance	50	----	1 MHz	7.1 Hz/fg and 1.1 Hz/fg
Davila et al. [25]	Resonance	~10 to 80	~4	---	Air: 9.23Hz/fg Water: 0.1Hz/fg

1.3 Research Objectives and Motivation

In this research we aim to design a gravimetric rare cell detector (RCD) system that eliminates the drawbacks of the proposed systems in the literature with capability of in flow analysis.

- The designed sensor will have the capability of working in the liquid media and eliminate the drawbacks due to damping in the liquid. This will be achieved by eliminating the squeeze film damping with changing the resonator geometry. The proposed geometry is the first one in the literature to be used in biosensing systems.
- Especially the cantilever sensors suffer from the site specific adhesion that is, the location of immobilized molecules on the cantilever surface is important for resolution of the sensor. The designed sensors will not be site specific by exploiting the geometry of the structure.
- The overall system will not need any optical setup or post processing step to make analysis but instead will use a close loop electronics interface to sustain the

operation and monitor the results. To achieve this task some CMOS interface and readout circuit will be needed and designed.

- The fabrication flow of the sensors will be planned and some new techniques to fabricate the sensors will be tried. The optimization of the process cycles will be completed during the fabrication.

Thesis chapters are planned to continue as follows:

Chapter 2 gives information about 2nd order spring-mass-damper systems and analyzes such systems for resonance phenomena. After investigating the basic theory behind mechanical structure, actuation and sensing of this mechanical structure is also discussed at this chapter. Moreover, an electrical equivalent circuit model is adapted to the mechanical structure for further analysis of devices. Chapter concludes by investigating the damping behavior of the gravimetric resonators with some design parameters.

Chapter 3 deepens the analysis of gravimetric resonators by modeling and simulating the structures both in MATLAB and COMSOL. MATLAB analyses give information about the injected currents and resonance frequencies of the structures. COMSOL simulations show mechanical modes of motion and give insight about the frequency of resonance.

Chapter 4 explains the fabrication flow of the gravimetric resonators in a time flow and mentions about the problems and solutions to the problems during the fabrication. Optimized fabrication flow with designed devices concludes this chapter.

Test results are presented in Chapter 5 and open loop responses of the mechanical structure are given. Test setup and necessary electronics interface of for open loop tests are also explained briefly.

Chapter 6 concludes this thesis report and mentions about concluded tasks and gives information about future work on the gravimetric cell detector project.

CHAPTER 2

THEORY & DESIGN

This chapter gives information about electromechanical resonance theory and explains the drive and sense mechanisms of the laterally excited mechanical structure. The emphasis behind the theory is mass sensing on this electromechanical structure. The spring mass damper system with detailed analysis on damping and quality factor is given to understand the effective mechanisms in the system. Detailed information about the spring-mass-damper system analysis is given in Appendix A. Gravimetric detection parameters are also examined and minimum detectable mass and mass sensitivity are determined.

Resonators use comb drive actuation technique for various works in the literature [36-41]. Comb drive actuation is also used in designing electromechanical filters [42], voltmeters [40], microgrippers [43], optical shutters [44], and inertial sensors [45-48]. A lateral electrostatic force which is independent of position is exerted by voltage controlled electrostatic comb-drive actuators make them suitable for micropositioning applications [1-2]. Together with nano tools like microtips, integrated systems can be fabricated with applications in scanning microscopy [49]. This work also examines the comb drive actuation and sensing mechanisms to realize a lateral gravimetric detector.

Section 2.1 gives information about basic spring-mass-damper system and explains the forced vibratory systems in detail. Section 2.2 explains the capacitive electrostatic actuation and sensing mechanisms together with electrical equivalent circuit of the resonator. Damping is analyzed separately in section 2.3. Finally, gravimetric performance parameters are questioned and sensitivity of the proposed gravimetric detector is analyzed.

2.1 Theory of Micro Electromechanical Resonance:

An electromechanical sensor is a band pass filter that rejects other frequency except the resonance frequency of the open loop mechanical structure. The electromechanical structure can be analyzed as a spring mass damper system like in **Figure 2.1**. The spring is the pulling back force and the damping is the dissipative force in the system.

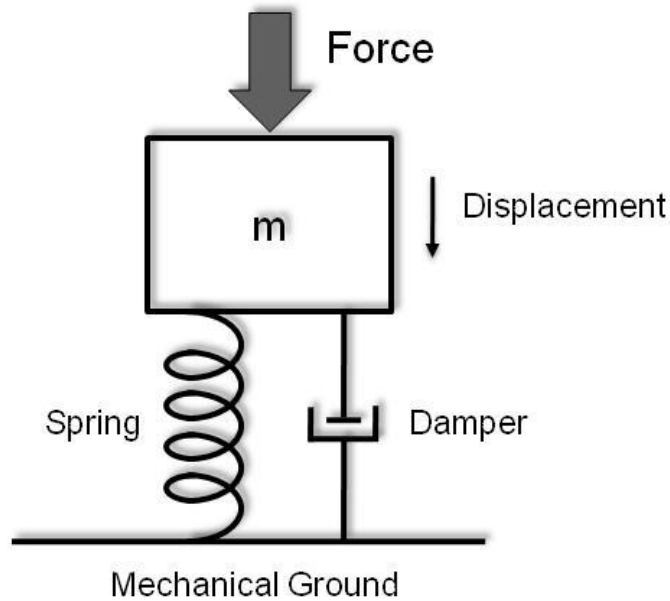


Figure 2.1 Spring Mass Damper System

Forced vibration response of the system is important to understand the driving mechanisms of the resonator for self resonant loop design. The applied force is electrostatic force with a constant frequency. Suppose that a spring-mass system is set to continuous oscillation by applying a sinusoidal force with a frequency of w and amplitude of F_0 , $F = F_0 \sin(wt)$, the differential equation for the system is:

$$m\ddot{x} = -kx - c\dot{x} + F_0 \sin(\omega t) \quad (2.1)$$

The solution to equation (2.1) can be analyzed in two parts: homogenous solution and particular solution.

To solve for homogenous solution, we have to solve the equation (2.2).

$$m\ddot{x}_h + c\dot{x}_h + kx_h = 0 \quad (2.2)$$

The solution to equation (2.2) is known to be damped oscillation (for $n < \omega_0$)

$$x_h = Ae^{-nt} \sin(\sqrt{(\omega_0^2 - n^2)}t + \alpha) \quad (2.3)$$

To solve for the particular solution, a specific solution with stable oscillation characteristic will be used and the parameters of the solution will be determined by using equation (2.1).

$$x_p = B \sin(\omega t - \varphi) \quad (2.4)$$

where B is the amplitude of the resulting vibration and φ the phase lag of the vibration against the sinusoidal force. By substituting equation (2.4) into equation (2.1), and solving the equation leads two equations:

$$B(\omega_0^2 - \omega^2) - f \cos \varphi = 0 \quad (2.5)$$

and

$$2nB\omega - f \sin \varphi = 0 \quad (2.6)$$

Therefore the amplitude B and the phase lag φ are found in equations (2.7) and (2.9) respectively.

$$B = \frac{f}{\sqrt{(w_0^2 - w^2)^2 - 4n^2w^2}} \quad (2.7)$$

For $w/w_0 = \lambda$ and $B/B_0 = \beta$ and equation (2.7) can be written as

$$\beta = \frac{1}{\sqrt{(1 - \lambda^2)^2 + 4\zeta^2\lambda^2}} \quad (2.8)$$

$$\varphi = \tan^{-1} \frac{2nw}{w_0^2 - w^2} \quad (2.9)$$

Thus, the solution to equation (2.1) is,

$$x = Ae^{-nt} \sin(\sqrt{(w_0^2 - n^2)}t + \alpha) + B \sin(wt - \varphi) \quad (2.10)$$

The solution given in equation (2.10) indicates that, in the early stages, beats occur due to forced vibration and damped vibration, giving rise to transient oscillations, which are usually short-lived and can be ignored in most cases. We will only consider what happens at steady state.

There is a phase lag of φ between the driving force frequency and resonance frequency of the mechanical structure. For very small w , φ is close to zero. φ increases with w , passes $\pi/2$ at the natural frequencies of the system and approaches π at very high frequency.

Amplitude of the response also changes with excitation frequency. For low excitation frequencies $\beta \approx 1$. This means that the amplitude is the same as the displacement caused by the static force F_0 . When excitation frequency comes closer to the natural frequency of the system than equation (2.8) states that the amplitude has a maximum at $w = w_0\sqrt{1 - 2\zeta^2}$. If the damping is light ($\zeta < 0.7$), w is very closer to w_0 and β is approximately equal to $1/2\zeta$, which can be very large for small ζ . The resonance peak disappears at $\zeta \geq 0.7$. In this case, the curve for $\beta \sim w$ relation has the largest flat region (i.e., the largest bandwidth). Therefore, $\zeta = 0.7$ is often referred to as an optimum damping condition. For higher excitation frequencies the amplitude decays very fast since $\beta \approx 1/\lambda^2$.

To find the resonance frequency of mechanical system we will use the condition of $d\beta/d\lambda = 0$ and find that the resonant frequency of a forced vibration is $\lambda_r = \sqrt{1 - 2\zeta^2}$ or $w_r = w_0\sqrt{1 - 2\zeta^2}$. As the natural vibration frequency (without damping) of the system is w_0 and the damped vibration frequency of the system is $w_d = w_0\sqrt{1 - \zeta^2}$ we find that, for slight damping, w_0 , w_d and w_r are all close to each other.

At resonant frequency the relative amplitude reaches a maximum value

$$\beta_r = \frac{1}{2\zeta\sqrt{1 - \zeta^2}} \quad (2.11)$$

For slight damping, we have the amplitude at resonance: $\beta_r \approx 1/2\zeta$.

By substituting w_r into equation (2.9), we have the phase lag at resonance

$$\varphi_r = \tan^{-1} \frac{\sqrt{1 - 2\zeta^2}}{\zeta} \quad (2.12)$$

For slight damping, $\varphi_r = \tan^{-1} 1/\zeta = \pi/2$ or $\zeta = 1/\tan \varphi_r$.

Quality factor of the resonator determines the sharpness of the designed resonator, that is, it determines the sharpness of a filter and resonators are band pass filters. Q -factor determines how under-damped an oscillator or resonator is. Higher Q indicates a lower rate of energy loss relative to the stored energy of the oscillator; the oscillations die out more slowly.

For a system vibrating at its resonant frequency w_r , the displacement is given as

$$x = A \sin w_r t \quad (2.13)$$

The total energy of the system is calculated by using equation (2.14).

$$E = \frac{1}{2} m \dot{x}^2 = \frac{1}{2} m A^2 w_r^2 \quad (2.14)$$

The energy dissipation in one cycle is calculated by taking integral over one period and given as,

$$\Delta E = - \int_0^T F_d \dot{x} dt \quad (2.15)$$

where F_d is the damping force, i.e., $F_d = -c\dot{x}$. Therefore, we have

$$\begin{aligned} \Delta E &= \int_0^T c \dot{x}^2 dt = \pi c A^2 w_r \text{ and} \\ Q &= 2\pi \frac{E}{\Delta E} = \frac{m w_r}{c} \end{aligned} \quad (2.16)$$

By using $n = \frac{c}{2m}$ and $\zeta = \frac{n}{w_o} \cong \frac{n}{w_r}$ we have $Q \cong \frac{1}{2\zeta}$

Quality factor is important for gravimetric detectors since it gives information about minimum detectable frequency and mass. To increase the quality factor in mass detection systems, natural frequency can be increased with expense of reduced injected current. Another way is to reduce damping over the structure and the design at this study uses both alternatives to increase the quality factor and mass sensitivity of the gravimetric resonators.

Although trade offs between quality factor and injected current seems trivial, control of the mechanical structure at higher frequencies put some constraints on the design. Dedicated electronics will also have difficulties with higher resonance frequencies. The more stiff the mechanical resonator, the more higher the frequency. However, injected current decreases due to reduced displacement of the mechanical structure. Decreased displacement stems from the increased stiffness due to increased spring constants.

2.2 Capacitive Electrostatic Actuation and Sensing

Actuation and sensing mechanisms of micro mechanical structures can be performed by using different techniques like thermal, mechanical, optical, and electrostatic. Thermal actuation uses thermal expansion most of the time to cause a deflection in the actuation part of the micro mechanical structure which is not suitable for lateral comb drive resonators. Sustaining mechanical actuation through the operation of resonator requires a dedicated complex control system, the motion of the lateral resonator is in the range of nano-meters and hence the control of the mechanical actuation is difficult. Optic techniques prevent the system to be used without need of any additional setup. Due to above mentioned reasons, electrostatic is the most suitable and adaptive technique since it does not require any additional setup like in the optics or need for complex control mechanisms.

2.2.1 Electrostatic Capacitive Actuation

Electrostatic actuation is the most effective method among these aforementioned techniques due to its capacitive actuation scheme which is desired for comb drive actuation of lateral resonators. The force developed by the electrostatic actuator is proportional to the change in capacitance between the two combs, increasing with driving voltage, the number of comb teeth, and the gap between the teeth.

Capacitive actuation is the result of Coulomb's rule of electrostatic attraction. A parallel plate capacitor is represented in **Figure 2.2**. The moving plate has three degree of freedom in x , y , and z directions. l_0 , h_0 , and d_0 are stationary dimensions when there is not any movement of the plate. Variable dimensions of the plates for different directions can be written as:

$$l(\mathbf{x}) = l_0 + \mathbf{x}, \quad d(\mathbf{y}) = d_0 + \mathbf{y}, \quad h(\mathbf{z}) = h_0 + \mathbf{z}$$

To calculate the capacitance these variables are used and the capacitance between parallel plates is calculated as:

$$C(\mathbf{x}, \mathbf{y}, \mathbf{z}) = \eta \varepsilon_r \varepsilon_0 \frac{l(\mathbf{x})h(\mathbf{z})}{d(\mathbf{y})} \quad (2.17)$$

where η is the fringe field factor, ε_r is the relative permittivity of the medium between parallel plates and ε_0 is the permittivity of vacuum. Fringing fields become more dominant when plate periphery to gap ratio gets smaller.

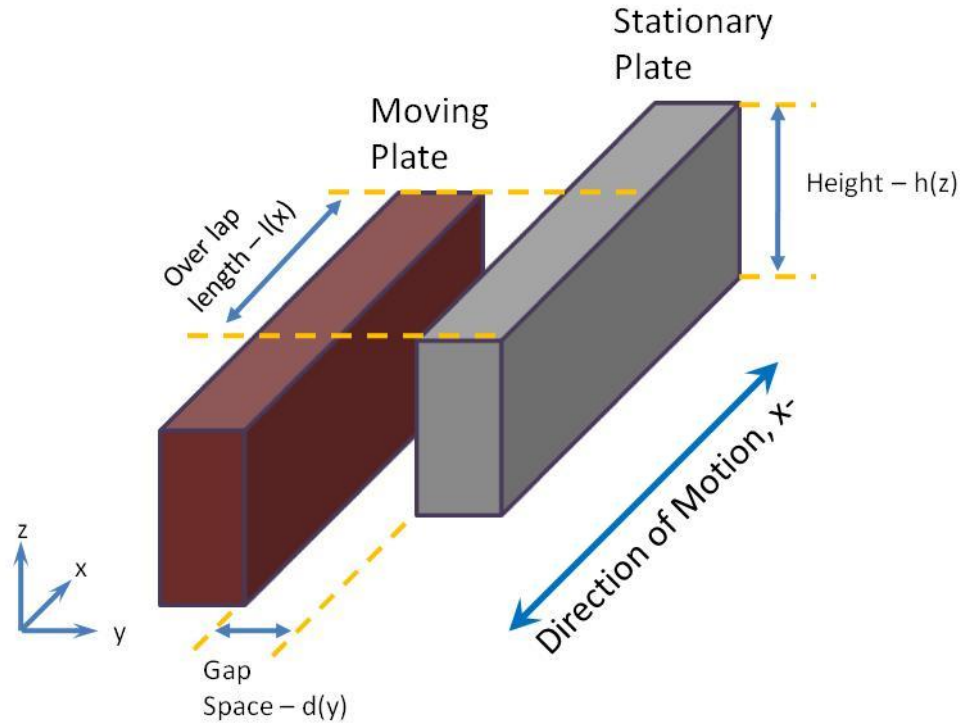


Figure 2.2 Parallel plates forming a capacitor and dimensions

There are active two actuation mechanisms to create electrostatic force: varying gap and varying overlap area. Although varying gap structures have more voltage to force gain, they suffer from nonlinearity and side instability due to pull-in effects. Therefore a more linear mechanism is selected for actuation that is varying overlap area actuation.

The electrostatic energy stored in a capacitor C, with a potential difference of V applied, is given by below formula:

$$W_e = \frac{1}{2} CV^2 \quad (2.18)$$

The force between the parallel plates is the gradient of the energy stored in the parallel plate capacitance. Hence, the force is calculated and found in equation (2.20) when the applied potential is given like in equation (2.19) in the lateral direction only. We are not

interested in the force in other directions for the moment. In fact the motion in other directions can be neglected by designing the springs of the mechanical structure properly.

$$V = V_{DC} + V_{ac} \sin(\omega t) \quad (2.19)$$

$$F_e = \frac{1}{2} \eta \epsilon_r \epsilon_0 \frac{h_0}{d_0} \left[\left(V_{DC}^2 + \frac{V_{ac}^2}{2} \right) + 2V_{DC} V_{ac} \sin(\omega t) - V_{ac}^2 \cos(2\omega t) \right] \quad (2.20)$$

Equation (2.20) gives some idea about the behavior of the system when an AC and DC voltage is applied to the proof mass. Applying pure AC signal will result in a force with twice the excitation frequency. This situation is not desired due to lose of linearity during excitation. Applying only DC potential will not cause any actuation since the plates will try to pull each other until they stick together or the spring force that holding the plates comes equilibrium with the electrostatic force. To prevent problems due to 2ω in equation (2.20) one can choose that $V_{DC} \gg V_{ac}$. Therefore the term with 2ω can be ignored in the force equation in x-direction and force equation turns into the below formula:

$$F_e \cong \frac{1}{2} \eta \epsilon_r \epsilon_0 \frac{h_0}{d_0} \left[\left(V_{DC}^2 + \frac{V_{ac}^2}{2} \right) + 2V_{DC} V_{ac} \sin(\omega t) \right] \quad (2.21)$$

2.2.2 Electrostatic Capacitive Sensing

The principle in the previous section is based on the actuation of the mechanical structure and electrostatic actuation theory is examined. Capacitive sensing is the sense

of the physical motion of the sensor and does not depend on the actuation mechanism. The electrostatic actuation of parallel plates causes a fluctuating motion of the plates and this fluctuation also induces energy. Since the motion of the resonator is assumed to be in the x-direction only, the sense part will generate a current due to mechanical fluctuations in the x-direction only.

The capacitance of the parallel plates can be written as:

$$C(\mathbf{x}) = \eta \epsilon_r \epsilon_0 \frac{l(\mathbf{x})h_0}{d_0} \quad (2.22)$$

If we write the stored charge on the capacitor when a voltage of V is applied,

$$Q(\mathbf{x}) = \eta \epsilon_r \epsilon_0 \frac{l(\mathbf{x})h_0}{d_0} V \quad (2.23)$$

If the case when one of the plates is moving is considered then the capacitance changes due to change of varying overlap area or varying distance between the plates. This capacitance change also changes the charge amount which means that current induction occurs. This injected current can be converted to voltage on a high impedance node with impedance of Z .

The current injected is the time derivative of the stored charge on the plates. The injected current is calculated in equation (2.24).

$$i(t) = \frac{\partial Q}{\partial t} = \frac{\partial C}{\partial t} V + C(t) \frac{\partial V}{\partial t} \quad (2.24)$$

Equation (2.24) has two parts one is coming from the change of the capacitor and the other from the excitation voltage. Excitation voltage given in equation (2.24) has a time component and hence the derivative is significant. But if we take the $V_{DC} \gg V_{ac}$ then we can assume that the AC term can be neglected and equation (2.24) turns into

$$i(t) \cong \frac{\partial C}{\partial t} V_{DC} = \left(\frac{\partial C}{\partial x} \frac{\partial x}{\partial t} \right) V_{DC} \quad (2.25)$$

If we continue in the Laplace domain, then

$$I(s) \cong V_{DC} \frac{\partial C}{\partial x} sX(s) = V_{DC} \epsilon_r \epsilon_0 \frac{h_0}{d_0} sX(s) \quad (2.26)$$

Since we will use a comb drive actuation and sensing system the injected current for one parallel plate couple will be multiplied by N , where N is the number of total comb drive pairs in the sense side of the resonator.

The injected current is converted to voltage in the high impedance node of the resonator output. The voltage is given in Equation (2.27).

$$V_{ac}(s) = NI(s) \left[\frac{1}{sC_0} // Z \right] \quad (2.27)$$

where C_0 is the stationary capacitance of the resonator that is the capacitor that there is no excitation. Z is the impedance at the output of the resonator due to electronics interface following the resonator.

2.2.3 Electrical Equivalent Circuit of Gravimetric Resonator

After deriving actuation and sensing equations, we can now model the resonator as an equivalent electrical model. Modeling the mechanical structure as an electrical circuit gives the advantage of fast analyzing the structure by using standard SPICE tools. Interfacing the mechanical structure with the designed electronics interface circuit and modeling the closed loop response of the resonator is another advantage of modeling mechanical sensor as electrical equivalent circuits.

The parameter that consumes energy in an aforementioned spring-mass-damper system is the damping. Hence we can model the damping as a resistor in the electrical

equivalent circuit. Force is the parameter that is stored in the spring and consumed on the damper and can be represented as a voltage source on the model. Velocity of the rotor comb drives causes a current injection at the sense port of the resonator that the velocity can be modeled as current source in the model. When velocity is represented with current, the displacement is represented with the total charge that velocity can be replaced with derivative of displacement and current can be replaced with time derivative of the injected charge. If we write Hook's law and model this law in electrical domain:

$$F = kx \text{ where } F \leftrightarrow V \text{ and } x \leftrightarrow Q \quad (2.28)$$

If we rearrange the equation for electrical model and let the parameter "A" as the electrical equivalent of the spring constant:

$$V = A \int I$$

rearranging again,

$$I = \frac{1}{A} \frac{dV}{dt} \quad (2.29)$$

Equation (2.29) shows that spring constant can be modeled as reciprocal of capacitor in electrical equivalent model.

Equivalently, if we write Newton's 2nd law and represent the mass as "B" during the derivation, rearranging equation gives:

$$F = ma \leftrightarrow V = B \frac{dI}{dt} \quad (2.30)$$

It is seen in equation (2.30) that B is equivalent to inductance (L) in the electrical model.

After obtaining the parameters in electrical domain we will investigate the relationships of these parameters to construct the whole model.

The electrostatic force in the x-direction is given in equation (2.31).

$$F_x(t) \cong 2N\epsilon_r\epsilon_0 \frac{h_0}{d_0} V_{DC} V_{ac} \sin wt \quad (2.31)$$

If we rearrange the equation and form a relation between the force exerted in x-direction and applied AC excitation in Laplace domain, than

$$\frac{F_x(s)}{V_{exc}(s)} \cong 2N\eta\epsilon_r\epsilon_0 \frac{h_0}{d_0} V_{DC} = N_{ac} \quad (2.32)$$

When equation (2.32) is investigated, the force can be represented as a voltage source therefore equation (2.32) turns to be a voltage transformer with winding ration of N_{ac} . At his point we modeled the drive port of the resonator and modeled the applied electrostatic actuation applied to proof mass.

We will continue with current, equation (2.33) gives the relation between injected current and comb displacement in Laplace domain.

$$I_x(s) \cong 2N\eta\epsilon_r\epsilon_0 \frac{h_0}{d_0} V_{DC} sX(s) \quad (2.33)$$

rearranging,

$$\frac{I_x(s)}{sX(s)} = 2N\eta\epsilon_r\epsilon_0 \frac{h_0}{d_0} V_{DC} = g_{sns} = N_{ac}$$

$sX(s)$ term refers to time derivative of the displacement in time domain and displacement in mechanical domain is modeled as charge in the electrical domain. Therefore, time derivative of displacement will be the current in electrical domain. Hence we can deduce that g_{sns} in equation (2.33) can be modeled as the gain of a current controlled current source.

Electrostatic actuation and sensing is modeled in electrical domain. The remaining part of the model is the resonator model. After taking the electrostatic actuation, model converts the input AC excitation to electrostatic force. Sense port of the resonator takes the displacement and converts this information to injected current. Therefore the

resonator will take the electrostatic force as the input and will convert it to displacement. The overall structure can be visualized as three blocks of systems cascaded each other: drive port, resonator, and sense port.

The relation between displacement and electrostatic force is the solution to the spring-mass-damper system and given in equation (2.34).

$$\frac{X(s)}{F_x(s)} = \frac{1}{ms^2 + bs + k} \quad (2.34)$$

Overall transfer function of the open loop resonator is given in equation (2.35).

$$G_x(s) = \frac{F_x(s)}{V_{exc}(s)} \frac{X(s)}{F_x(s)} \frac{I_x(s)}{X(s)} = \frac{s(g_{sns} N_{ac})}{ms^2 + bs + k} = \frac{s \left(2N\eta\epsilon_r\epsilon_0 \frac{h_0}{d_0} V_{DC} \right)^2}{ms^2 + bs + k} \quad (2.35)$$

The parasitic capacitance C_p present in any system with electrostatic transduction may be incorporated at the electrical model as shown in **Figure 2.3**. The admittance of the resonator at resonance is given by

$$Y_{eq} = \frac{1}{R_m} + j\omega_0 C_p \quad (2.36)$$

where R_m is the motional resistance of the resonator.

For sufficiently large values of $\omega_0 C_p$ relative to $1/R_m$, the parasitic capacitance term dominates, resulting in a feedthrough current that effectively masks the motional current derived from R_m . Furthermore, this parasitic capacitance creates a parallel-resonance at the frequency given by

$$\omega_p = \omega_0 \sqrt{1 + \frac{C_m}{C_p}} \quad (2.37)$$

The electrical model is completed and the overall electrical model of the electromechanical resonator is given in **Figure 2.3**.

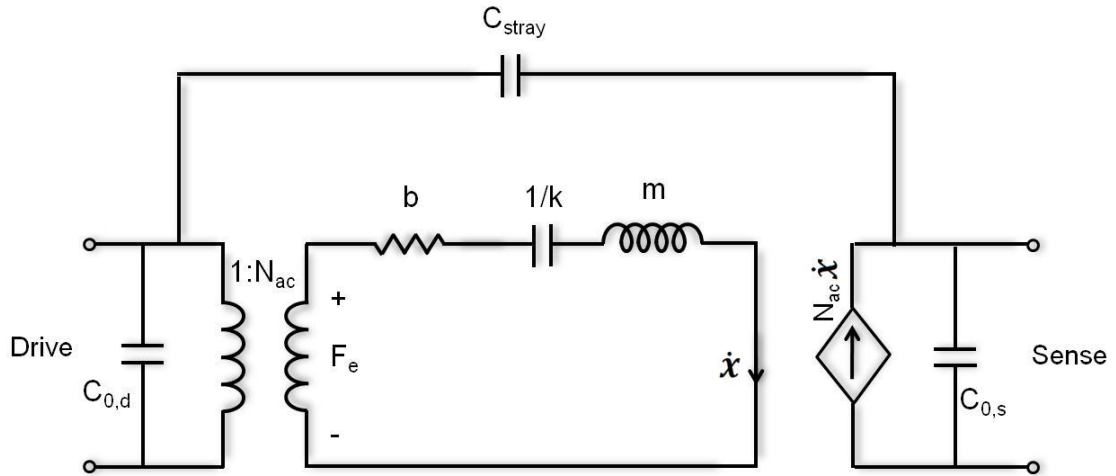


Figure 2.3 Electrical model of the electromechanical resonator

2.3 Damping Analysis

There are several active mechanisms that cause damping during lateral motion of the resonators. The fluid squeezed under the proof mass, the fluid sliding over the surface and bottom layer of the proof mass and squeezing and sliding fluid on the sidewalls between rotor and stator cause damping.

All of the effective mechanisms are dependent on the geometry parameters of the structure, the type of the fluid, area and volume of the fluid, and the distance between top and bottom plates over and under the proof mass respectively. At this point effective decay distance becomes dominant to decide type of the damping and make some assumptions over damping.

Analysis of damping is very important in electromechanical resonators since the quality factor, hence the sensitivity of the resonator, is dependent on the damping introduced to the system.

The air behaves like a thin film that damper the movement of proof mass and this is called slide film damping. Damping over the proof mass is calculated by using Navier Stokes equations in the literature [5].

For an infinite plate assumption the Navier Stokes equation turns into equation (2.38) for the x-direction if there is no external force or pressure gradient in the fluid.

$$\frac{\partial u}{\partial t} + u \frac{\partial u}{\partial x} = \frac{\mu}{\rho} \frac{\partial^2 u}{\partial z^2} \quad (2.38)$$

where ρ is the density of the fluid and μ is he coefficient of viscosity. u is the velocity of the plate in the x-direction. The 2nd term in the left hand side can be neglected if plate is infinite and oscillation amplitude is much smaller than the plate area.

To neglect the 2nd term in the above equation, the geometric dimensions of the plate should satisfy Equation (2.39), further analysis of the derivations can be found in [5].

$$l \gg 2 \frac{d^2}{\delta^2} A$$

where

$$\delta = \sqrt{\frac{2\mu}{\rho\omega}} \quad (2.39)$$

δ is the effective decay distance, the distance in the z-direction where velocity of the fluid decays from the plate by a factor of e .

Effective decay distance for fluidics is important since the fluid flow characteristic is determined according to the relations between effective decay distance and the plate dimensions.

Two damping models are concerned,

- Couette Damping Model: When frequency w and the distance between plate and the substrate, d , are small and so that δ is much larger than d .
- Stokes Damping Model: It is a more generalized solution and will be used in conditions where Couette model cannot be satisfied [50].

2.3.1 Damping of a comb Drive Resonator:

After examining the flow and damping models we can analyze the damping on a comb drive resonator. For the sake of simplicity of analysis, Couette flow model is used during comb-drive damping calculations. The squeeze film damping is ignored since the motion of the resonator is in lateral direction.

(a) Slide-film Damping Force on the Bottom Plate

When the gap distance between the plate and the substrate, d_p , is much smaller than the effective decay distance δ , that is the damping is Couette than the force can be calculated as in equation (2.40).

$$F_{btm} = \mu \frac{A_p}{d_p} \frac{dx}{dt} = c_{btm} \frac{dx}{dt} \quad (2.40)$$

where A_p is the effective plate area including the areas of plates, beams and fingers and c_{btm} is the damping coefficient for bottom plate damping.

(b) Slide-film Damping Force on the Top Plate

If the channel height, h_{chn} , above the resonator is not much smaller than the effective decay distance, than we cannot use Couette flow model but use Stokes flow model. The damping force calculated using stokes model is given in equation (2.41) [5].

$$F_{top} = \mu \frac{A_p}{\delta} \frac{dx}{dt} = c_{top} \frac{dx}{dt} \quad (2.41)$$

(c) Slide-film Damping Force on the Side Walls

Since the gap distance between the rotor and stator fingers is very small we can assume that the damping is Couette and equation (2.42) gives the damping on the side walls of the structure.

$$F_{wall} = \mu \frac{A_s}{d_s} \frac{dx}{dt} = c_{wall} \frac{dx}{dt} \quad (2.42)$$

where A_s is the side wall area of the rotor fingers and d_s is the distance between the rotor and stator.

(d) Air Drag Force

The air drag force calculations can be found in the literature [give ref or Analysis book]. The air drag force is given in equation (2.43) [Analysis or give ref.]

$$F_{drag} = \frac{32}{3} \mu l \frac{dx}{dt} = c_{drag} \frac{dx}{dt} \quad (2.43)$$

where l is the characteristic dimension of the moving plate and can be taken as half of the width of the plate.

Total damping force can be calculated by simply adding the above mentioned forces. These damping forces are dominant forces for a lateral resonator and slide film damping on top plate will be the dominant force during operation of the gravimetric detectors since a fluid flow will cause the damping over the plate.

2.4 Gravimetric Detection and Performance Parameters

The mechanical analysis for a resonating structure including damping and quality factor analysis are given in section 2.1. Required electrical equivalent circuit is also constructed and details are given in section 2.2.

There are also some limitations on the motion of the oscillation for a resonator due to external effects for a resonator. The minimum detectable mass (MDM) is calculated theoretically at this section and analyzed to gain insight about effect of changing design parameters on MDM.

There are two dominant noise sources for the gravimetric resonator:

- Thermal vibration of the mechanical structure.
- Noise generated in the control and interface electronics.

Although the external electronics noise is the dominant noise force, the thermal vibration of the mechanical structure puts a theoretical limit on the minimum detectable mass. Because, the noise of the interface electronics is controlled externally and different architectures can be utilized to decrease interface noise.

By using equipartition theorem and thermal energy and spectral noise calculations the mean-square frequency modulation due to thermal noise is calculated and given in equation (2.44) [51].

$$\langle(\Delta w)^2\rangle = \frac{1}{2\pi} \int_{\Delta w} \frac{2E_\phi}{E_{osc}} (\Delta w)^2 d(\Delta w) \quad (2.44)$$

where E_ϕ is the phase noise energy and E_{osc} is the oscillation energy of the resonator. $\Delta w = w_0 - w$ and equation (2.44) is valid if $w_0/2Q \ll \Delta w$. By taking the integration and arranging equation (2.44), minimum detectable force gradient is calculated in equation (2.45).

$$\Delta F_{min} = \frac{2k_x \Delta w}{w_0} = \sqrt{\frac{4k_x k_B T}{w_0 Q \langle x_{osc}^2 \rangle} BW} \quad (2.45)$$

Where k_x is the spring constant in the x-direction, $\langle x_{osc}^2 \rangle$ is the mean square amplitude of the oscillation of the resonator and BW is the band width. Minimum detectable frequency and minimum detectable mass are calculated using equation (2.45) and given in equations (2.46) and (2.47) respectively.

$$(\Delta\omega)_{min} = \frac{2}{x_{osc}} \sqrt{\frac{k_B T}{k_x Q} w_0 BW} \quad (2.46)$$

$$(\Delta m)_{min} = \frac{4m}{x_{osc}} \sqrt{\frac{k_B T BW}{k_x Q w_0}} = \frac{4}{x_{osc}} \sqrt{\frac{mb_x k_B T}{k_x} BW} \quad (2.47)$$

Calculated minimum detectable mass in equation (2.47) sets a theoretical base limit for mass detection. The above analysis are based on the thermal noise of the mechanical structure, but the interface noise coming from the electronics part also sets a boundary for the minimum detectable noise.

Equation (2.47) shows that decreasing damping and mass of the resonating structure will decrease minimum detectable mass and increasing the spring constant will also decrease the minimum detectable mass. Increasing the oscillation amplitude via increasing electrostatic force will also enhance the minimum detectable mass of the gravimetric resonator.

Decreasing mass of the resonating structure requires the minimization of the geometric dimensions of the structure. Decreasing proof mass dimensions will also decrease the slide film damping since the area in equations (2.40), (2.41), and (2.42) will also decrease. Smaller springs also come with stiffness and hence the spring constant will increase that also reduces the minimum detectable mass (MDM). However increasing the spring constant will result a decrease in the oscillation amplitude and will cause increase in MDM. Moreover, decrease in oscillation amplitude will decrease the injected

current in sense port that can be inferred from Hook's law. Decreasing in injected current may cause the current to be buried in the noise at the sense port which sets a lower bound for minimum injected current.

Decreasing the dimensions will decrease the electrostatic force to displacement gain which means higher gains are required in electronics circuit will be needed to sustain the oscillation of the resonator.

Decreasing the dimensions will also decrease the effective proof mass area that will decrease the number of attached cells on the proof mass.

2.4.1 Mass sensitivity in Gravimetric Resonators

Added mass on the resonator surface will cause change in effective spring constant of the resonator. By neglecting this effect and assuming that added mass is very small compared with mass of the resonator we can write equation (2.48) in terms of added mass Δm , and frequency shift Δf .

$$f_n - \Delta f_n = \frac{1}{2\pi} \sqrt{\frac{k}{\Delta m + m_{PM}}} \quad (2.48)$$

where m_{PM} is the resonator mass and f_n is the resonance frequency of the resonator. The mass sensitivity of the gravimetric resonator can be defined as the mass derivative of the resonance frequency and given in equation (2.49).

$$\left| \frac{\partial f_n}{\partial m} \right| \approx \frac{f_n}{2m} \quad (2.49)$$

As can be seen in equation (2.49), to increase the mass sensitivity of a gravimetric resonator, the natural resonance frequency of the resonator has to be increased meanwhile mass of the resonator should be kept small. The upper limit for the increase

of resonance frequency is the specifications of the interface electronics and readout circuit.

2.5 Summary

At this chapter first a 2nd order spring mass damper system analyzed with no force condition. The proposed gravimetric resonator will have a driving electrostatic force and hence forced vibrations and oscillation is analyzed in detail. System behavior for different damping conditions are questioned and explained since the damping is one of the most effective parameters during analysis of resonating structures.

Electrical equivalent drive and sense mechanisms are derived for further analysis of the whole system. Mechanical resonator is also modeled in electrical domain which will enable SPICE or MATLAB analysis during design and simulation of the system.

Finally, minimum detectable mass is calculated theoretically. This calculation gives only information about noise equivalent mass difference of the gravimetric resonator theoretically. The actual minimum detectable mass will be few orders of this calculated value. The sensitivity of the gravimetric detector is analyzed and need for higher frequency operation and frequency limitation is discussed at the end.

Although there are also some other 2nd order forces that effect the performance of the resonator as electrostatic levitation and side instability problem, they are not discussed here. Literature can be investigated for further analysis of these effects [52-55]

CHAPTER 3

DESIGN AND SIMULATION OF GRAVIMETRIC RESONATORS

The mechanical model and equations are explained in Chapter 2. Excitation voltage to injected current gain is given in equation (2.35). This gain expression tells the effect of geometric and electrical parameters on the mechanical gain. However, these equations do not give insight about the design parameters out of this equation. Moreover, equation (2.35) is not the only parameter that determines the performance of the design.

Gravimetric resonator design is simply divided into subsections and each part is investigated separately. First, the body of the resonator including the device footprint, comb fingers and proof mass is studied and design parameters and effect of these parameters on device performance are questioned. Another important mechanical structure that will affect resonator performance is the architecture of springs that holds the proof mass. Finally, some concerns about microfluidic operation of the resonator inside a channel are given and solutions are discussed. A final discussion over trade offs on the design parameters are discussed.

The performed simulations in MATLAB which enables to model all mechanical structures and electrical actuation and sensing on the model are given and compared with the performed FEM analysis in COMSOL.

3.1 Mechanical Structure of Gravimetric Resonator

A lateral electrostatic actuation and sensing is adopted for the design of the gravimetric resonator and mechanical body of the resonator with geometric parameters is given in **Figure 3.1**.

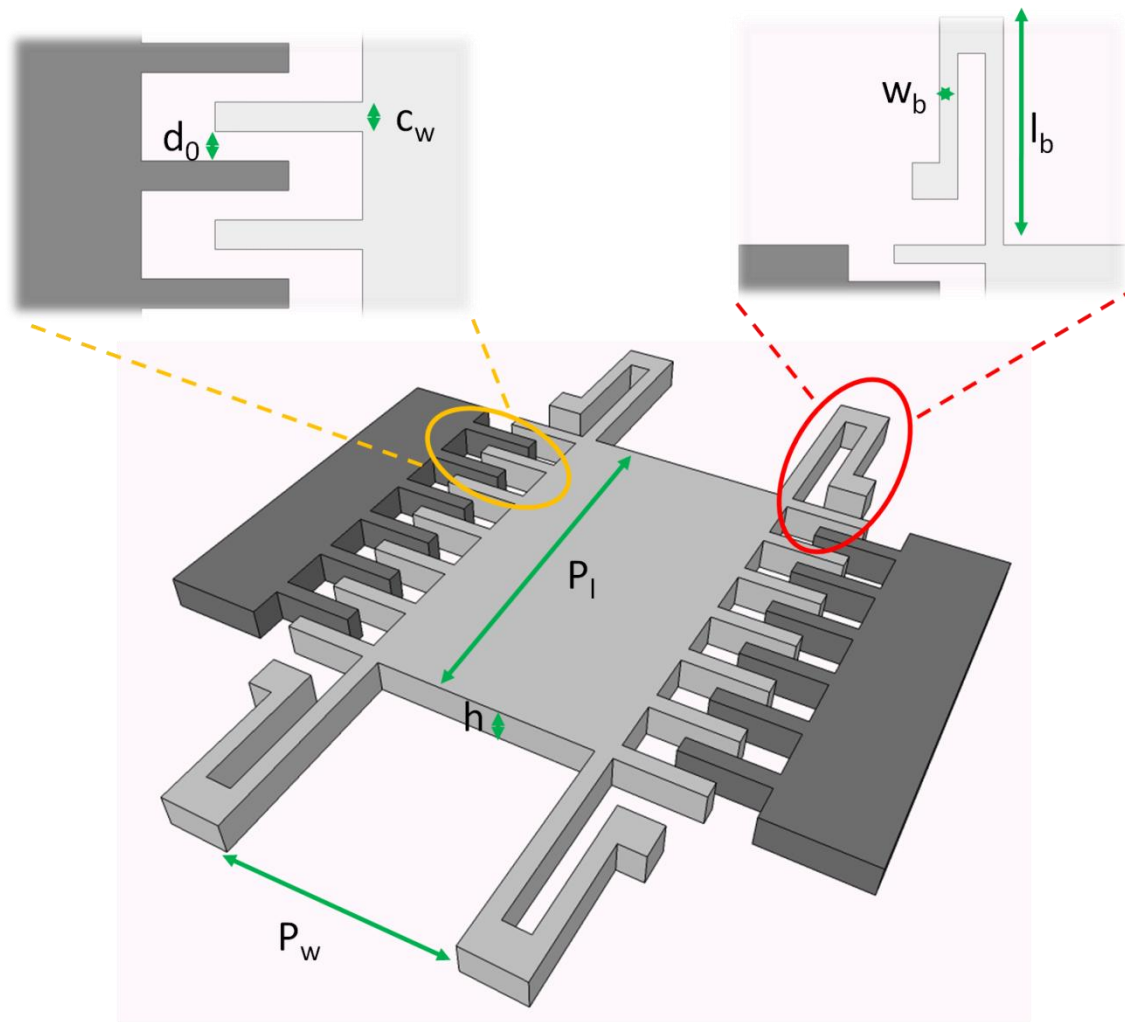


Figure 3.1 Mechanical structure of the resonator showing comb finger and spring beam dimensions.

To eliminate the drawbacks of cantilevers in the fluid media, lateral oscillation principle is exploited and comb drive actuation and sensing is decided as the driving mechanisms for the operation of the resonator. By this way, the damping in vertical direction, squeeze film damping, will be eliminated.

- The resonator width, P_w , is determined in accordance with minimum channel width and comb length. The resonator width is not that critical and can be decided after determining other parameters. Similarly, resonator length will also be determined at the end. However, do not forget that an unbalanced choice of width and length will cause different harmonics to emerge.
- Total area of the stationary anchors should be kept small to decrease stationary capacitance at the drive and sense ports of the resonator. However, the main concern here comes from the undercuts during fabrication. Therefore anchor dimensions are not critical design parameters.
- In varying overlap area capacitance change, the force is not dependent on varying overlap length, c_l , of the capacitive plates (see equation (3.1)). However, the comb length must be chosen larger than the spacing to maintain a proper geometry for lateral resonator.
- The height of the resonator structure, h , is determined with SOI device layer thickness. The height directly affects the electrostatic force as can be seen in equation (3.1). The height also changes the mass of the resonator. Hence there is a tradeoff between mass increase and force decrease.

$$F_e \cong \frac{1}{2} \eta \epsilon_r \epsilon_0 \frac{h_0}{d_0} \left[\left(V_{DC}^2 + \frac{V_{ac}^2}{2} \right) + 2V_{DC} V_{ac} \sin(\omega t) \right] \quad (3.1)$$

- Comb space also changes electrostatic force as can be seen in equation (3.1). Therefore decreasing comb space is desired but the fabrication limitations prevent to decrease comb spaces below 1 μm . Comb width also determined by fabrication considering the undercuts and notching effects. Decreasing comb space and comb width will also enable to fit more comb fingers into a defined

proof mass length, therefore increases comb number $N(d_0, c_w, P_l)$ which will increase injected current at the sense port of the resonator.

Displacement between stationary anchors and comb finger tips should be determined by displacement of the proof mass. The pull in phenomena also should be considered during the design. This parameter is chosen to be equal with comb space, d_0 , due to hydrophobicity concerns that will be mentioned later.

After investigating the mechanical body structure of the gravimetric resonator some effort is also given to the design of flexure beams.

3.1.1 Design of Spring Beams

During the design of the spring arms it is important to have a desirable compliance in the direction of motion while to have an almost infinite stiffness in other directions. If this condition is satisfied most of the harmonics will also be eliminated. As a rule of thumb, if $k_y, k_z > 10k_x$ is intended, then the proof mass motion can be assumed to be only in x-direction. Spring beam compliance also determines the frequency of resonance. Operation frequency determines the minimum detectable frequency and minimum detectable mass. However, care should be taken since a high compliance in the direction of motion will decrease displacement and cause a reduction in the injected current through sense port of the resonator.

Different spring designs are available in the literature for comb drive actuators, clamped-clamped structure, crab leg architecture and folded flexures are some of the examined designs in the literature and shown in **Figure 3.2**.

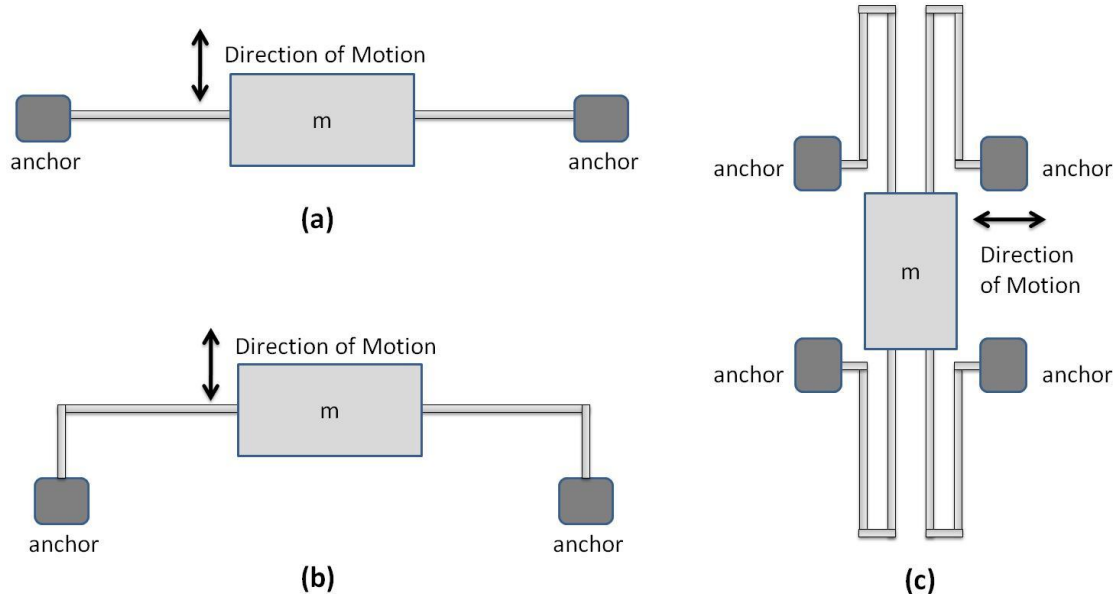


Figure 3.2 Different spring arm designs (a) clamped-clamped beam structure, (b) crab leg design, (c) folded flexure design.

For a clamped-clamped beam structure shown in **Figure 3.2** (a), the spring constant can be very high. However, for large displacements clamped-clamped structure suffers from nonlinearity. Behavior of this type of beam structure under small and large displacements can be found in the literature [56]. Crab like structures also suffer from buckling problems since there is not any way to release the stress on the spring arms.

To decrease the effect of axial forces on spring flexures, crab leg architecture can be used as shown in **Figure 3.2** (b). Although the crab leg flexures are more linear than the clamped-clamped beam structure there is a tradeoff between linearity and spring stiffness that stiffness decreases in crab leg design. To eliminate the drawbacks of smaller spring constants in crab leg design, folded spring design is proposed.

The folded structure releases the stress on the arms without buckling since the truss shown in **Figure 3.2** (c) will allow elongation or contradiction along y-direction and buckling will be prevented. Folded spring beams behave linearly during the deflection

and spring constants are as high as clamped-clamped structures without losing linearity. Spring constants along x-, y-, and z-directions are given in equations (3.2), (3.3) and (3.4) for the folded beam structure given in **Figure 3.2** (c).

$$k_x = \frac{1}{2} E_x \frac{h w_b^3}{l_b^3} \quad (3.2)$$

$$k_y = \frac{1}{2} E_y \frac{w_b h}{l_b} \quad (3.3)$$

$$k_z = \frac{1}{2} E_z \frac{w_b h^3}{l_b^3} \quad (3.4)$$

where l_b is the length, w_b is the width of the spring arm and h is the thickness.

For $k_y, k_z > 10k_x$, $l_b > h \gg w_b$ is chosen.

3.1.2 Micro channel design and constraints

Using resonators inside microfluidic channels is a big challenge in gravimetric detection. Damping is a big problem in fluid media and this problem is partially eliminated by using lateral resonator inside the fluid hence eliminating squeeze film damping. However, the possibility of fluid to fill the trenches will cause squeeze film damping in between the gap spaces. To eliminate fluid filling inside the trenches a polymer with hydrophobic properties will be used on the finger structures. This polymer is parylene and has superior hydrophobic properties [57-58].

Another problem is the biocompatibility issue. Biocompatibility can be defined as the ability of material not to harm biological species when used in vivo or in vitro applications in biology. Not harming single cell is not the indicator of biocompatibility but the material should not cause any reaction in the immune system when used for in

vivo application. One of the reasons that parylene is selected as coating polymer is biocompatibility of parylene [59-61].

The ions inside buffer solution or analysis media will cause some current to pass between isolated comb fingers and hence harm the cells and the device. To prevent this effect the electrical properties of parylene is exploited [62]. Parylene coating will enable online monitoring inside the fluid since no current can pass over parylene.

A conformal coating of parylene layer causes capacitance change between comb fingers. Equivalent dielectric permittivity increases due to parylene coating and calculated in equation

$$\varepsilon_r = \left[\frac{(d_0 - 2t_p)}{\varepsilon_f} + \frac{2t_p}{\varepsilon_p} \right]^{-1} \quad (3.5)$$

where ε_r is equivalent dielectric permittivity, d_0 is the gap distance between fingers, t_p is the parylene thickness, ε_p is parylene dielectric permittivity, and ε_f is fluid dielectric permittivity filled between fingers. This change of equivalent permittivity increases the electrostatic force as can be seen in equation (3.1).

Coating of parylene should be performed carefully, since thick parylene will cause proof mass to stick anchors and not move. This effect is experimentally observed and thinner coatings are optimized during the fabrication.

3.1.3 Design Parameters Summary

Aforementioned design parameters are put together to increase the resonator performance and a figure of merit (FOM) is constructed. Since the transducer has to be integrated with electronics, it cannot be conceived only in terms of its mass sensitivity but also in electrical terms. For this purpose, the FOM finally proposed can be used to compare the performance of different mass resonant transducers. In particular, the

expressions of these FOMs are expressed for a lateral resonator in terms of its physical parameters.

The excitation voltage to injected current gain of the resonator should be increased as mentioned before. While increasing the gain, the minimum detectable mass should be decreased to increase the resolution. In mass sensing applications with readout electronics, a high value of the resonance frequency may be a disadvantage and ones want to minimize it in order to relax the readout circuit specifications. Calculated figure of merit is given in equation (3.6) according to the design parameters.

$$FOM = \frac{[\delta \epsilon_f \epsilon_0 h]^3 \sqrt{l_b^3 l V_{dc}^4}}{\eta^3 w^{3.5} d_{min}^{10.5} t_p^3} \quad (3.6)$$

Quality factor for a resonator structure is another figure of merit and care should be taken. When we analyze equations, we see that increase in natural frequency decreases the first figure of merit which is not desirable but increases quality factor. Therefore resonance frequency should be selected properly for electrical interface limitations and quality of the resonator in air should not decrease below 1000 during this selection.

It is clear in (3.6) that minimum space between comb fingers is the most effective parameter for the performance of the resonator. Moreover, decreasing thin parylene layer thickness will also increases the resonator performance but the limitation for this condition is minimum parylene coating in SCS parylene coater. Increasing spring beam length will increase the oscillation amplitude and hence the injected current. Effect of other parameters can be examined in equation (3.6).

Device codes are determined according to the geometric parameters and explained on **Figure 3.3**.

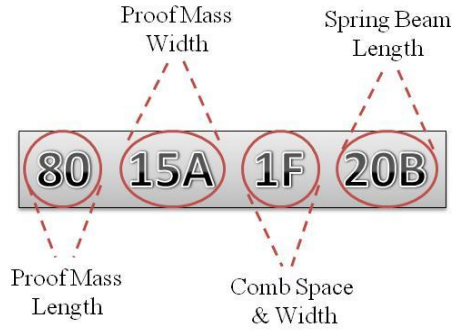


Figure 3.3 Device code according to the geometrical parameters

3.2 Simulations

Simulation is important for optimization of design parameters to reach the final device design. The MATLAB model is constructed by using SIMULINK tool of MATLAB and linearization is used to obtain the bode response of the resonators. The model is shown in **Figure 3.4**. The damping values are calculated by using the information in theory chapter. Electrostatic force is calculated and included into the model. FEM modal analyses of the designed mechanical resonators are performed to determine the harmonics of the motion.

Resonator electro mechanical model is designed in MATLAB[®] Simulink[®] tool as a 2nd order system. The inputs to the system are mechanical dimensions and electrical voltage. Damping, spring constants and external forces are calculated separately and included into model. The model is given in **Figure 3.4**. Electrostatic sensing and actuation are also included to model and therefore it is possible to perform open loop analysis and closed loop analysis of the system together.

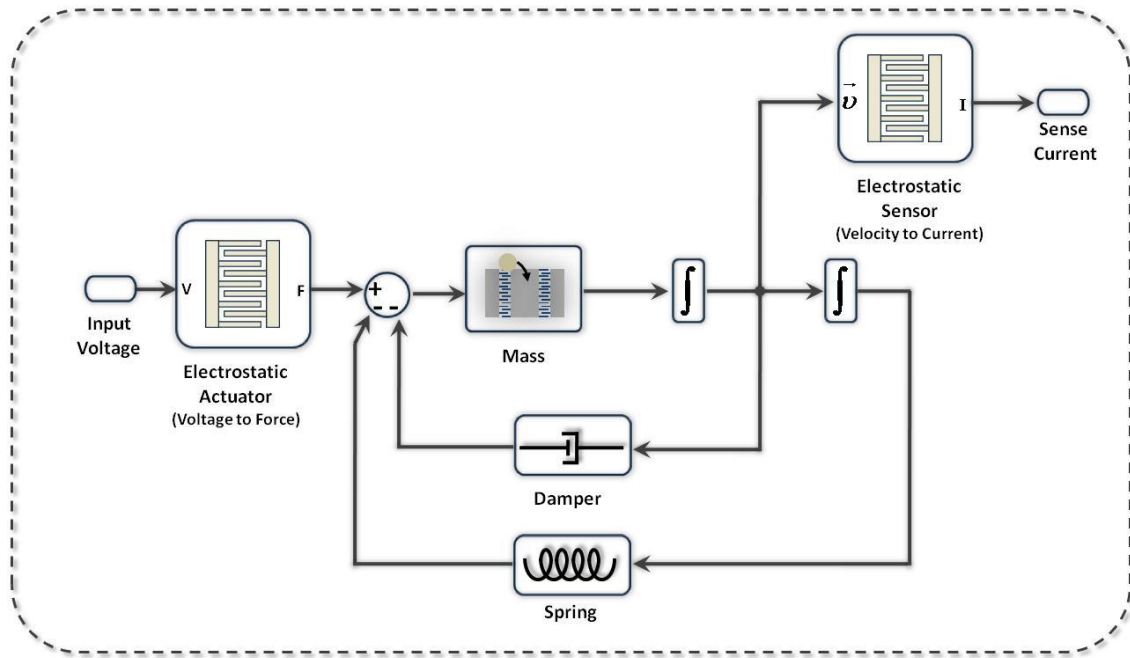


Figure 3.4 Electromechanical Simulink[®] model of the gravimetric resonator.

Resonator open loop responses are simulated for each device. **Figure 3.5** shows the simulated response of the resonator with device code 80 15A 1F 20B. The expected frequency of resonance for device 80 15A 1F 20B is about 335 kHz. However, the simulations of another device with code 40 15A 2F 20B shown in **Figure 3.6** demonstrates that the frequency ranges of devices are far separated and each device should be handled separately to achieve minimum mass detection. Therefore each simulation is performed and presented separately and results are given in Appendix B.

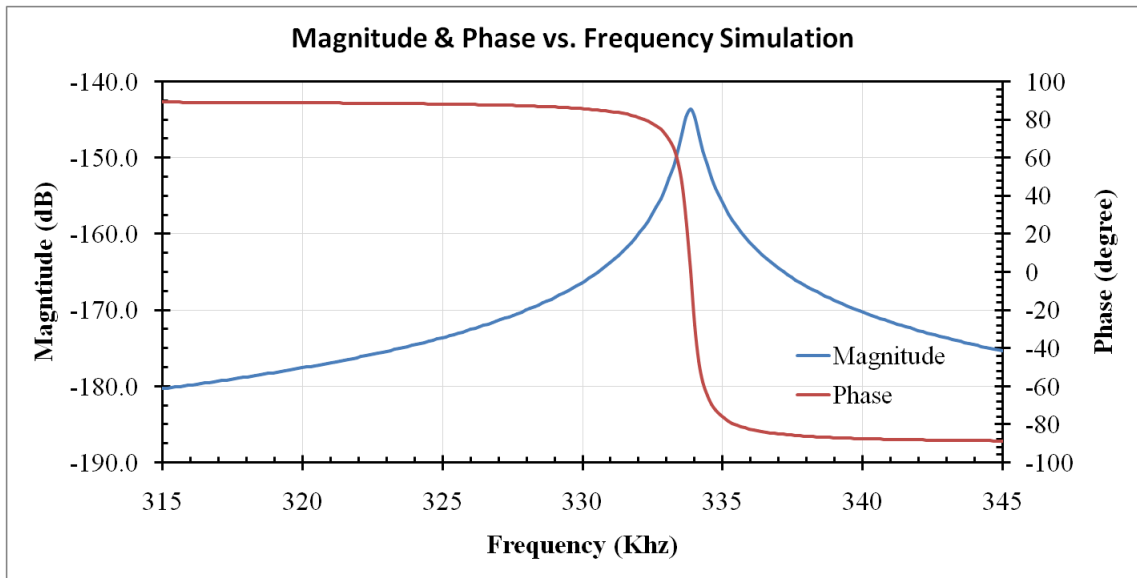


Figure 3.5 Simulated transfer function of gravimetric resonator with device code 8015A 1F 20B

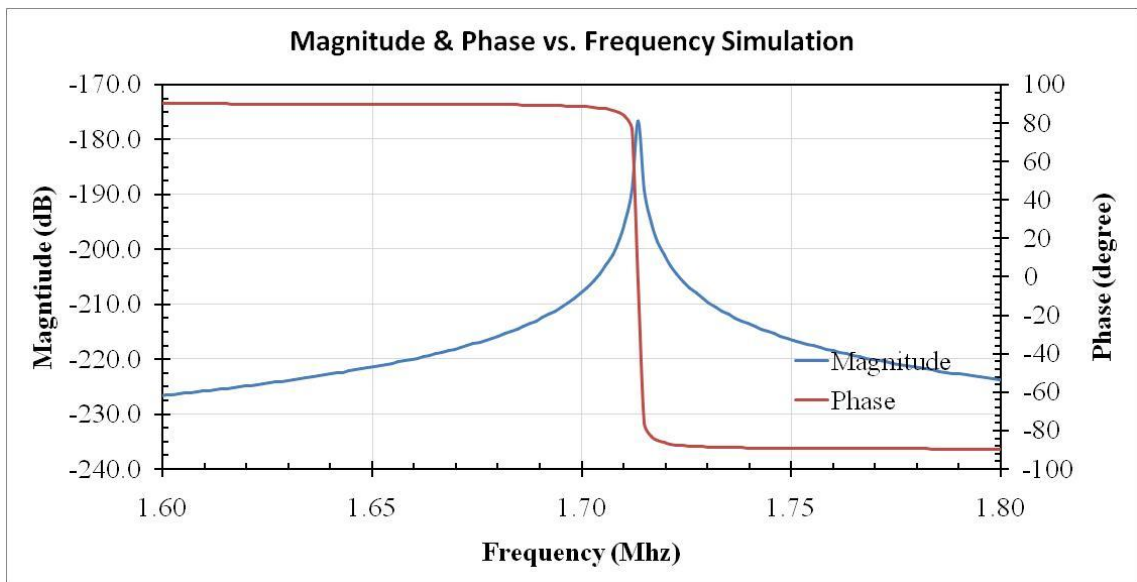


Figure 3.6 Simulated transfer function of gravimetric resonator with device code 4015A 2F 20B

3.2.1 FEM Analysis

COMSOL Mutiphysics is used during FEM analysis of structures. FEM analyses show different behaviors of the geometric structure and also gives harmonics of the motion. The geometry of the device is directly imported from mask layouts. The analysis for the first mode of device with code 80 15A 1F 20B is given in **Figure 3.7**. The resonant frequency is 476.26 kHz for this type of device. Since the comb finger width is at the limit of the fabrication capabilities, some undercuts and thinning on the comb fingers and spring widths are observed. Therefore the FEM model is rearranged to adapt these changes. The drawing is directly imported from the mask layout and the fabrication problems are added to the model including spring thinning. Other simulation results are given in Appendix B.

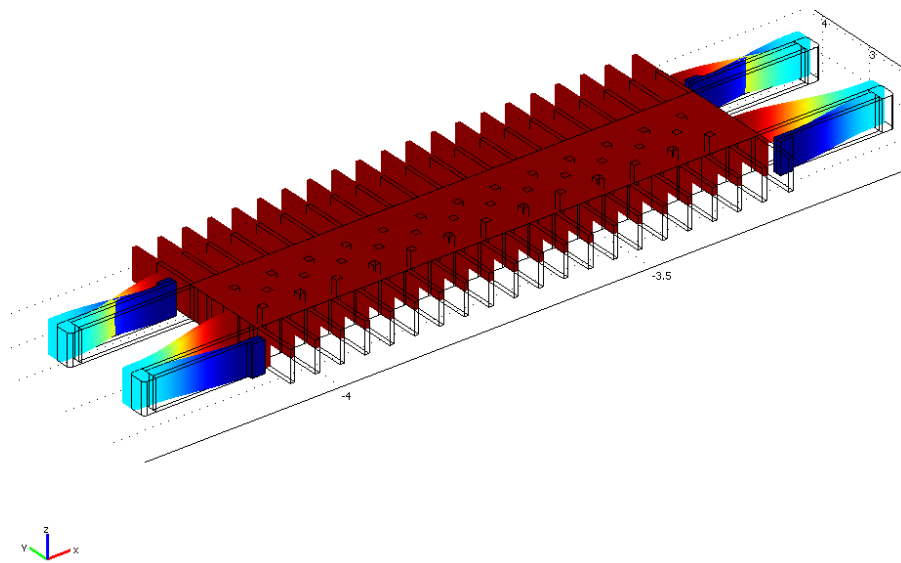


Figure 3.7 First mode FEM analysis of device with code: 80 15A 1F 20B after including the undercuts and errors coming from lithography and etching, first harmonic at 450.24 KHz

3.2.2 Spice Analysis of Stray Capacitance on Resonance Behavior

The electrical equivalent circuit designed in section 2.2.3 is constructed in LT spice and stray analysis is performed on SPICE circuit. Effect of stray capacitance on resonant behavior is given in **Figure 3.8**.

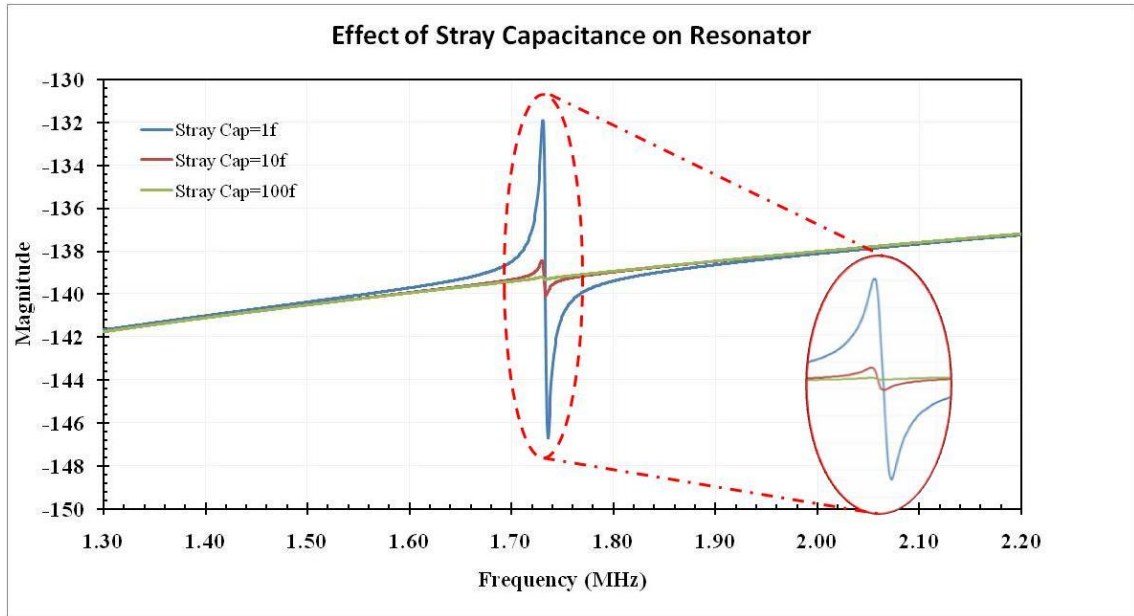


Figure 3.8 Effect of stray capacitance on sensor performance

To decrease the stray capacitance the stationary drive and sense port areas are limited. The area is upper bounded by stray capacitance but lower bounded with fabrication specifications. Effect of stray capacitance is eliminated during tests after some post processing of the data that will be explained in test chapter.

3.3 Summary of Design and Simulation

Design considerations for gravimetric detector are given at this chapter. The design cycle includes design of mechanical resonator with spring flexures. Different spring flexure architectures are discussed and folded spring beam structure is selected as the most appropriate design due to superior effects compared with clamped-clamped beam and crab leg structures.

Micro channel design concerns are discussed and effect of parylene coating is examined. Capacitance change due to change of effective permittivity is introduced and a final figure of merit is constructed to understand the degree of effects of parameters on the resonator.

Simulations performed in MATLAB and COMSOL are presented and results are given. These results are used to finalize the device design and optimization of geometric parameters. Effect of stray capacitance is also modeled in SPICE and results are presented.

Table 3.1 shows MATLAB and COMSOL results for different device types according to resonance frequencies. According to the COMSOL results some devices have their first modes out of the plane, we do not have the chance to control this effect in MATLAB. Also any mismatch between spring arms will promote or prevent out of plane motion.

Table 3.1 COMSOL and MATLAB results for all device types.

Device Code	COMSOL Results	MATLAB Results
16030A4F40B	706.36 kHz *	688 kHz
16030A4F80B	387.00 kHz	243 kHz
8030A4F40B	1.09 MHz *	973 kHz
8030A2F40B	384.69 kHz	315 kHz
8015A4F40B	1.10 MHz*	1.28 MHz
8015A2F40B	475.02 kHz	383 kHz
8015A1F20B	450.24 kHz	334 kHz
4015A2F40B	626.57 kHz	608 kHz
4015A2F20B	2.12 MHz	1.71 MHz
4015A1F20B	608.16 kHz	472 kHz

* The given responses are belong to 2nd mode, the 1st mode is out of plane

CHAPTER 4

FABRICATION

In this chapter fabrication of the gravimetric rare cell detector is explained. The problems during the fabrication and the solutions to the problems are examined. The optimization of the design cycles and fabrication are discussed briefly.

Gravimetric detectors at this study require conductive layers for capacitive actuation and sensing, therefore a highly conductive Si layer is selected as the resonator material. The Si layer thickness is important for the mass and resonance frequency of the resonator and designed to be 5 μm to increase the quality factor and mass sensitivity. The fabrication cycles does not allow using thinning steps since thinning up to 5 μm thickness with acceptable uniformity will be problematic.

Micro channel fabrication is another concern during the design of detectors. Micro channels on the device require a base to seal the device and hence Si wafer cannot be completely etched away outside the device area. This constraint also puts limit on the selection of fabrication technique.

Parylene coating and shaping the parylene for biocompatibility and electrical contacts may require lithography steps over suspended structures. Surface topologies on the wafer bigger than few microns may cause problems during lithography at this step.

Different fabrication techniques are examined by taking the above mentioned constraints into account and the most suitable technique is selected for the fabrication. Dissolved wafer silicon micromachining (DWSM), silicon on insulator (SOI), silicon on glass (SOG), and SOI on glass are the techniques that are discussed in this chapter.

4.1 Fabrication Techniques for Gravimetric Resonator

4.1.1 Dissolved wafer Process

Dissolved wafer silicon micromachining (DWSM) exploits different etch rates of silicon structures based on their doping level. Technique also uses anodic bonding of Si to micromachined glass substrate. Structural part of the Si wafer is processed by using deep reactive ion etching (DRIE) technique. After bonding, undoped Si is etched away via chemical techniques and doped-silicon sensors remain on the substrate [63].

The glass wafer is micro machined with HF solution and trenches necessary for proof mass suspension are formed on the glass substrate. Si and glass wafers are organically cleaned in piranha solution (1:1 - H₂SO₄:H₂O₂) prior to anodic bonding. Cleaned wafers are aligned and bonded together using an EVG 620 Precision Alignment System and an EVG 501 Universal Bonder respectively. The ambient temperature is 400 °C during the bonding and a 1000V bias voltage and 1500 N force on wafers are applied for bonding to occur.

The final step is to dissolve the undoped Si layer in EDP solution and releasing of the mechanical resonator in the solution. The suspended structure are cleaned with standard Aceton-Alcohol-Methanol cleaning and dried on hot plate. At this point the structures are suspended and should be handled with care.

However DWSM process is not suitable for fabrication of gravimetric detectors as device layer is designed to be 5 μm thick. The control of wafer thickness is crucial when working on high frequency applications since the mass will severely change with small changes in the thickness. DWSM requires doping of Si wafers which is not desirable for our process and also requires EDP wet etching of Si layer which is also not desirable. The anchor points of the gravimetric resonators are not large areas to decrease the capacitance at the sense port and hence doping at small areas will be required for this

fabrication flow. Therefore, DWSM process is not selected as a possible fabrication technique.

4.1.2 SOI process:

SOI technology gain importance in machining mechanical structures on Si wafers. The technology is attractive for inertial sensors or resonator applications since a high quality structural Si layer is on top of a thin insulating oxide layer with a thick handle wafer beneath the oxide layer. Buried oxide (BOX) can be used as sacrificial layer during the fabrication to release or suspend devices on the thin structural Si layer. Moreover, buried oxide is used as an etch stop during dry and wet etching processes. SOI technology is also compatible with current CMOS technology. There are several commercialized techniques in the literature like SOI MUMPS[®] [64], Micragem[™] [65] and Tronics [66].

The SOI multi-user MEMS process (SOIMUMPs) offered by MEMSCAP company is a 4 mask process for pad metallization, anchor and trench formation, structural layer formation on Si and an optional additional metallization with shadow mask process [64]. Metallization is performed by using lift off technique. Back side processing with DRIE is required to release the structures which is problematic and may cause some notches under anchor points.

The main advantage of SOI MUMPS over DWSM process is its high aspect ratio structures with small capacitive gaps compared with DWSM. Trench opening under the microstructures to be suspended decreases the damping on the bottom side and also prevents electrostatic stiction or levitation problems during resonator fabrication.

Although SOI process has advantages over DWSM process, it has problems during the suspension of devices and channel formation on top of fabricated devices with this technique is not possible. Back side etching for suspension of the devices will vanish the air trapping under the proof mass. This situation increases the damping by letting the

fluid flow between comb fingers. However SOI process is not completely given up, instead a modified SOI process is adopted and will be explained soon.

4.1.3 SOG Process

Silicon on glass process is based on through etching of Si wafer that is anodically bonded to a glass wafer to form resonating microstructures [67]. It is possible to fabricate high-aspect-ratio thick structures by using SOG process yielding highly-sensitive capacitive sensors with low mechanical-thermal noise and small parasitic capacitances.

SOG process starts with anodically bonding Si wafer onto a glass substrate. After bonding, Si wafer is etched in DRIE by using Bosch process. However, thorough etching of Si requires lots of time to be able to etch Si wafer controllably. Increase in time comes with heating problems since glass will prevent to cool down the Si wafer during etching. This problem can be solved by arranging successive etching and waiting times during etching process but it will not be controllable. After forming the microstructure over glass substrate the bonded wafers are put into HF solution to etch away the glass and suspend the structures. The isotropic nature of the glass etching will cause undercutting and will narrow anchor points. Moreover, the field will also be etched to form the undercuts which is not desirable for micro channel formation.

Gravimetric resonator in this study requires thin layer of device layer due to aforementioned design criteria in theory and design chapter. Therefore SOG process is not suitable for fabricating gravimetric resonators since handling of such thin wafers is impossible. Thinning of the Si wafer after bonding is another option but achieving 5 μm thick Si layer is not possible with acceptable uniformity.

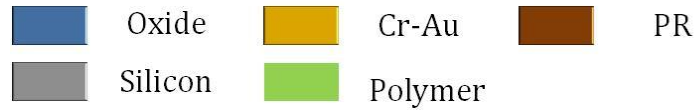
4.2 Fabrication Steps of Gravimetric Resonator

Since the aforementioned processes are not well suited for the fabrication of the gravimetric detectors, a different flow is adopted based on SOI and SOG technology with polymer (polyarylene) for electrical insulation, hydrophobicity, and biocompatibility.

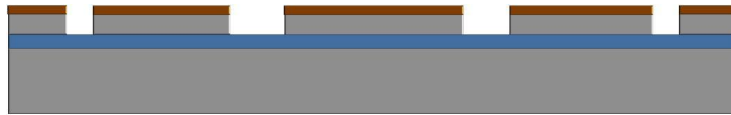
Different fabrication flows evolved over time during the project will be given in this section and solutions to the problems will be examined. The change of flow after each enhancement is presented and the optimum flow is generated at the end.

4.2.1 1st Generation Fabrication Flow

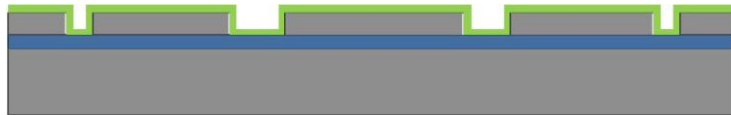
The process flow for first envisaged fabrication of gravimetric resonators is given in **Figure 4.1**. Fabrication starts with lithography on a polished SOI on the device layer. Prior to spin coating of photo resist (PR) the wafer is dehydrated to improve adhesion of photoresist onto Si surface and exposed to nitrogen flow inside nitrogen desiccators. S1813 [68] is used as photoresist since the aim is to fabricate structures with 1 μm feature size. Following the development of PR the wafer is processed inside STS Multiplex ASE HRM DRIE system. Comb fingers, spring arms, and active area with anchors are formed at this step. Etching of Si structures inside DRIE continues up to oxide area, buried oxide layer beneath structural Si layer is an etch stop during DRIE process. However, care should be taken since over etching inside DRIE will cause notches and may cause thinning of comb fingers and springs which will change mechanical properties of the resonator.



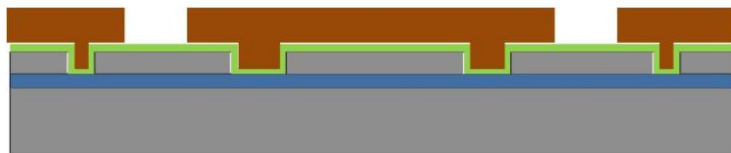
1. Lithography and pattern PR



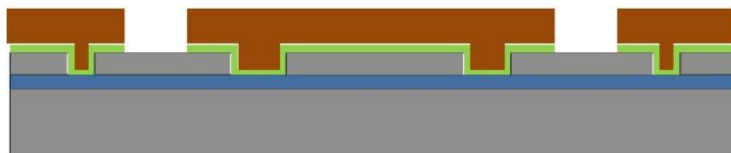
2. Active Layer pattern by DRIE with oxide as an etch stop



3. Strip PR and coat polymer with LPCVD



4. Lithography and pattern PR for polymer etching

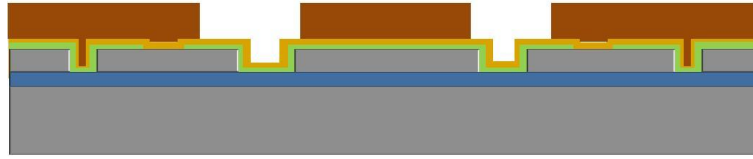


5. Polymer etching with Reactive Ion Etching (RIE)

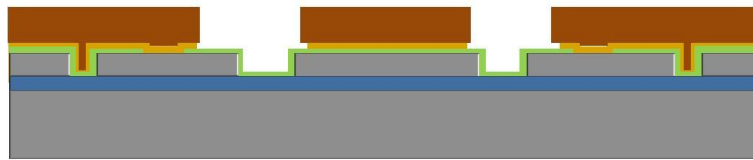


6. PR strip and Cr-Au coating with sputtering

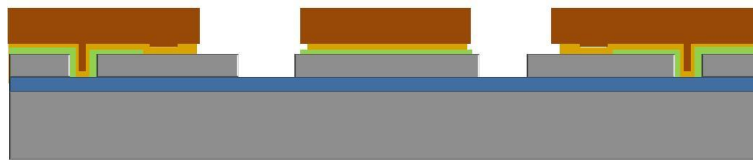
Figure 4.1 First generation fabrication flow for gravimetric resonator



7. Lithography and pattern PR for metal etching



8. Wet etching of Cr-Au metallization



9. RIE etching of parylene between comb fingers



10. Strip PR and devices are ready for wafer level tests



11. BHF release of the resonating structures

Figure 4.1 Continued.

After DRIE of SOI wafer, an insulating layer of polymer is coated over the structures to electrically separate the conductive Si surfaces prior to metallization. The coated polymer is parylene and has superior properties for electrical isolation that is, used in IC

technology to protect circuits against electrostatic discharging effects (ESD protection) [69]. Parylene is coated conformably by using LPCVD techniques onto the substrate.

Parylene is shaped to form via points to make electrical connections from the substrate. Etching of parylene requires lithography process. Parylene is a hydrophobic polymer and does not require use of HMDS [70], a solution to improve PR adhesion onto hydrophilic surfaces. Thickness of PR must be arranged according to the thickness of the parylene layer. PR etch rate to parylene etch rate is optimized and found that PR is etched three times faster than the parylene inside RIE. Therefore a thick PR with high aspect ratio is selected, AZ 9260 [71]. Etching of parylene is performed inside STS Multiplex RIE System. It is important to completely remove the parylene at via contact points to decrease the contact resistance after metallization.

After shaping the parylene, a thick Cr-Au deposition (300 Å – 4000 Å) is performed inside Bestec Magnetron Sputtering System. The thick metal is required for wire bonding on metallization pads. Cr layer serves to supply adhesion for Au layer. Ti is not used since there will be an HF process at the end and HF etches Ti layer. Metal is shaped with lithography techniques, masking the metal with PR and etching the remaining metal layer inside metal etchants.

The PR layer to shape the metal layer is also used to shape the parylene layer between comb fingers. The filled parylene between the fingers is etched in RIE system.

After metallization is finished the wafer is ready for suspending resonating structures. HF is used for suspension of devices in different concentrations. The results are inspected with the help of Idonus IR microscope and regular optic microscope.

The first generation fabricated devices are given in **Figure 4.2**. Electrical connections and SEM photographs of micro channels with comb fingers are given in **Figure 4.2**.

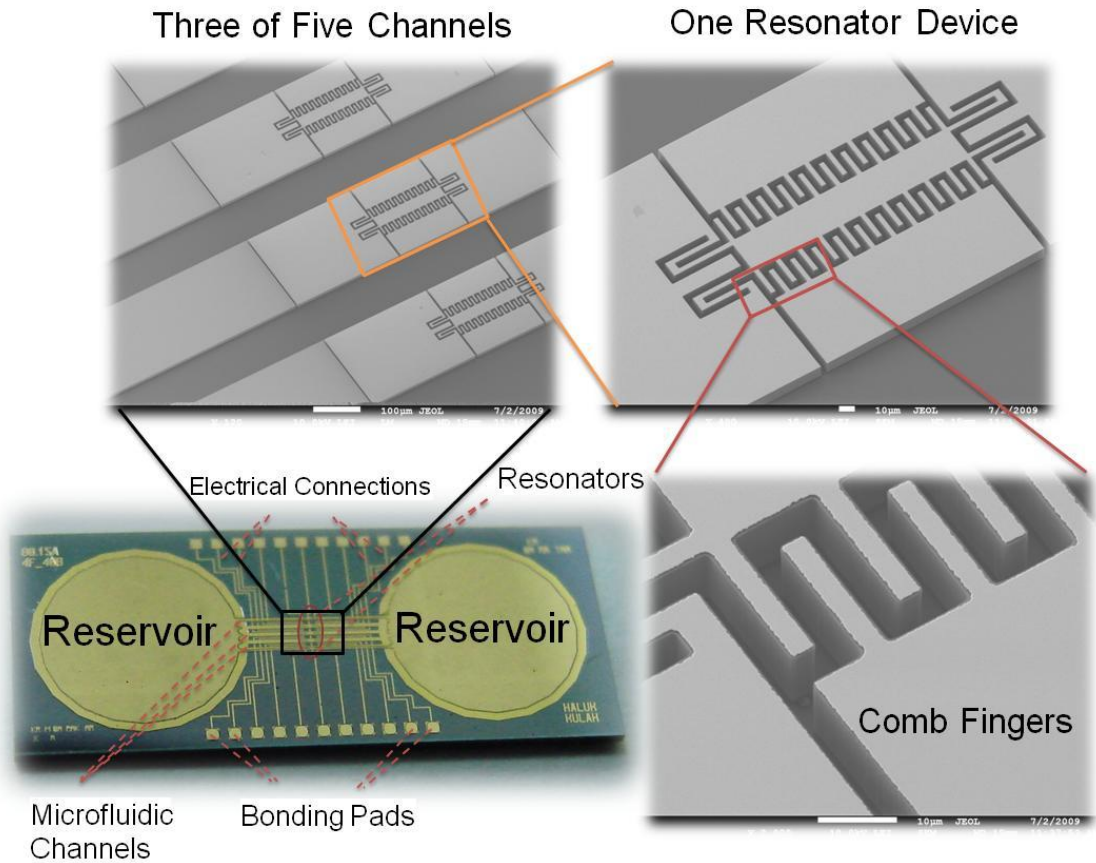


Figure 4.2 Fabricated first generation gravimetric resonator with SEM photographs of micro channels and device structure

Figure 4.3 shows the photograph of the device after BHF (1:3 – HF:NH₄F) etching of 20 minutes. The proof mass is broken intentionally with the help of “tape check” method to inspect remaining oxide under the proof mass. Focus of the microscope is changed and oxide islands are observed. It is clear that this amount of time is not enough to release the resonators.

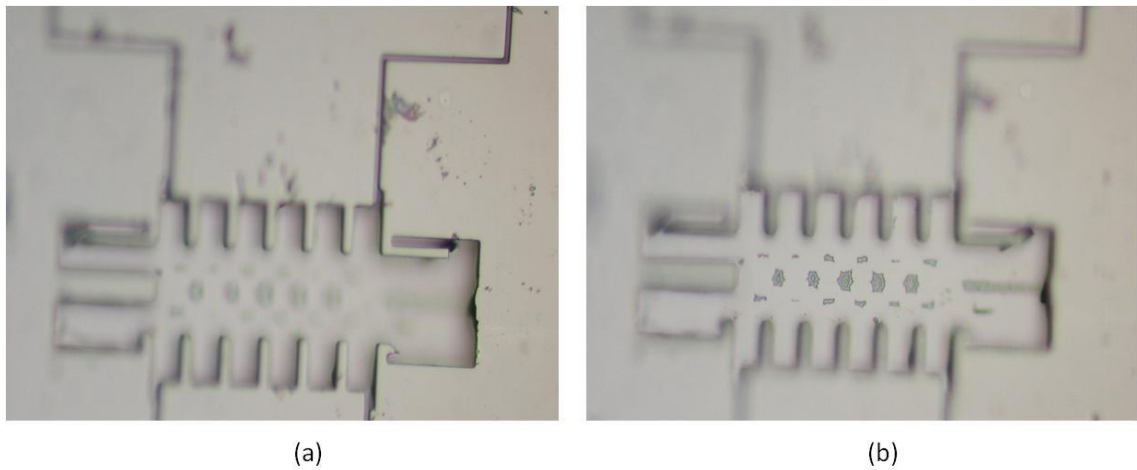


Figure 4.3 BHF (20 minutes 1:3 - HF:NH₄F) oxide etching and proof mass release process results. (a) Microscope is focused onto the top surface of the wafer, (b) Microscope is focused to the bottom and oxide islands are observed.

However, it is not possible to observe the beneath oxide etching without breaking the proof mass with optic microscope. We use IR microscope to inspect the oxide layer beneath the proof mass. **Figure 4.4** shows photo of two devices taken with IR microscope. Oxide under proof mass still remains after BHF (1:7 - HF:NH₄F) etching of 45 min.

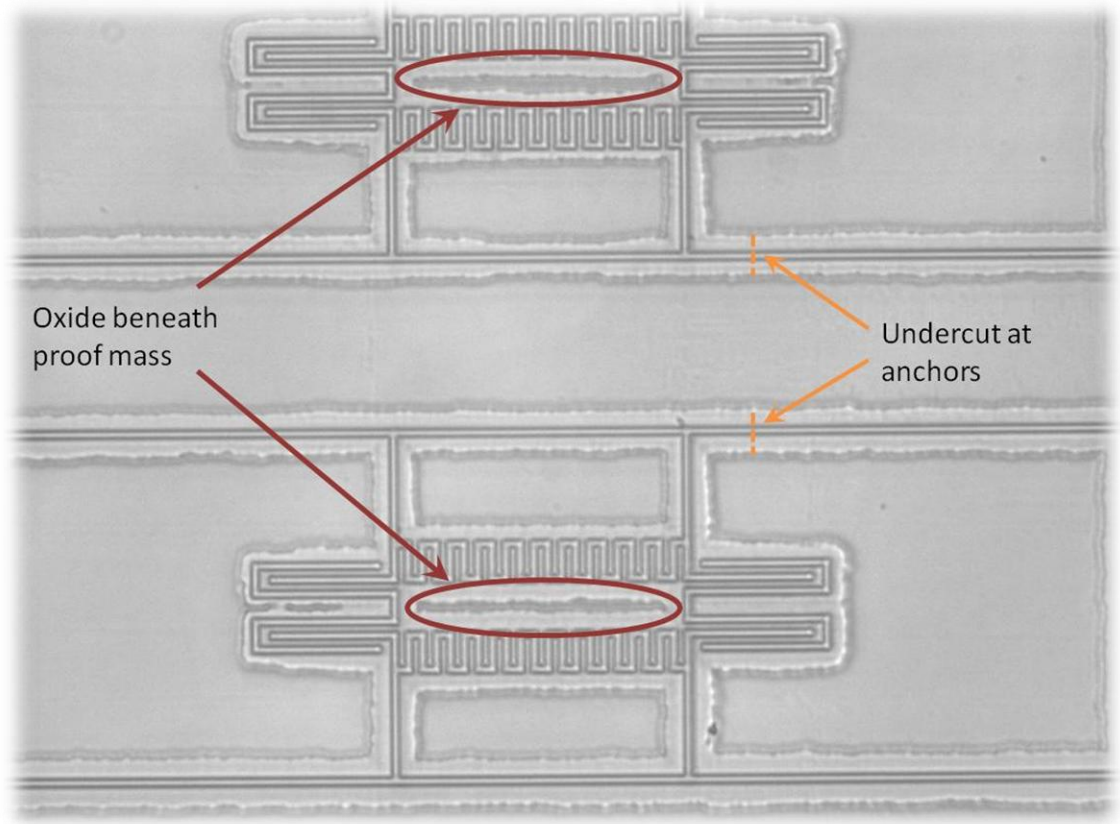


Figure 4.4 BHF (1:7 - HF:NH₄F) oxide etching photograph taken with Idonus IR microscope after 45 min. of etching.

Although fabrication steps for 1st generation flow are all optimized, lots of problems emerged and some problems cause us to give up this flow. Problems during the fabrication are given with SEM and microscope photographs and possible solutions are also discussed below.

4.2.1.1 HF Etching Problems

Although oxide etch rates for different concentrations of HF solutions are given in the literature, it is observed that these etching rates are not directly applicable for fabrication of gravimetric detectors. Because the HF solution enters beneath the proof mass through

the gaps between the comb fingers and these gaps are small that may prevent pass of solution under the proof mass. Repeatability of HF etching is also a problem that is encountered which requires serious inspection for each batch and puts limit on the yield of devices after etching. The anchors are broken randomly as shown in **Figure 4.5**, although the oxide layer still remaining under the anchors in 48 % HF after 90 seconds of etching time.

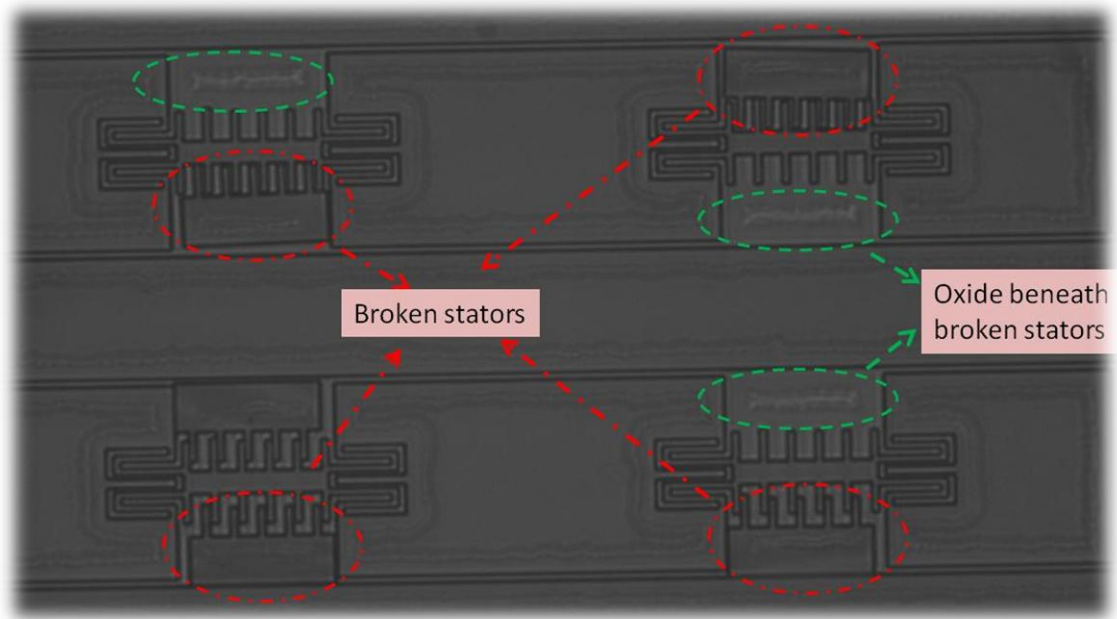


Figure 4.5 Idonus IR microscope photograph of device after 48 % HF etching for 90 seconds.

4.2.1.2 DRIE Notching and Lag

A serious problem during DRIE is notching at the bottom of the device on the oxide layer. Notching will decrease comb width and this will cause less current to be injected at the sense port of the gravimetric resonators. The destruction due to notching at the bottom of a comb electrode array, a flexure beam, and a rectangular etch hole are shown in **Figure 4.6** [72].

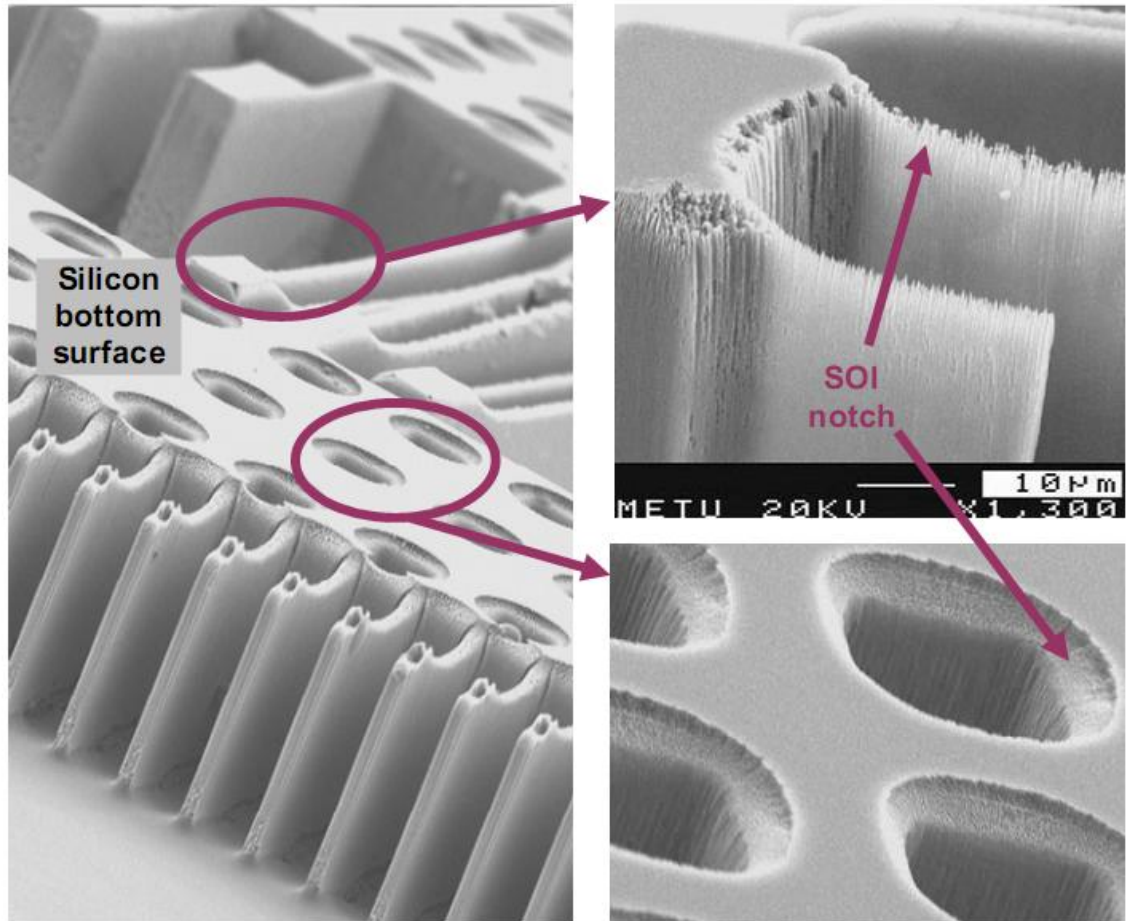


Figure 4.6 Sidewall damage (SOI-notch) as a result of the destruction of directionality of SF₆ ions due to the charged insulator surface at the bottom of a comb electrode array, a flexure beam, and a rectangular etch hole [72].

A common technique in the literature for suspending devices is to make etch holes on the proof mass. However using etch holes will decrease the bioactive area on the proof mass which is not desirable. We used etch hole technique but limited the numbers and dimensions of these etch holes to effectively release the resonators inside HF solutions. Adding etch holes on the proof mass cause a phenomena called DRIE lag during etching of Si wafers with this technique [73]. The etch holes for the release of the structures in the 1st generation fabrication flow are not etched away in the DRIE although the finger

spaces are etched. This effect causes some notching effects shown in **Figure 4.6** if DRIE is continued further to etch away all the spaces. The DRIE lag problem is shown in **Figure 4.7** that the etch holes are not etched up to oxide etch stop although the finger spaces are.

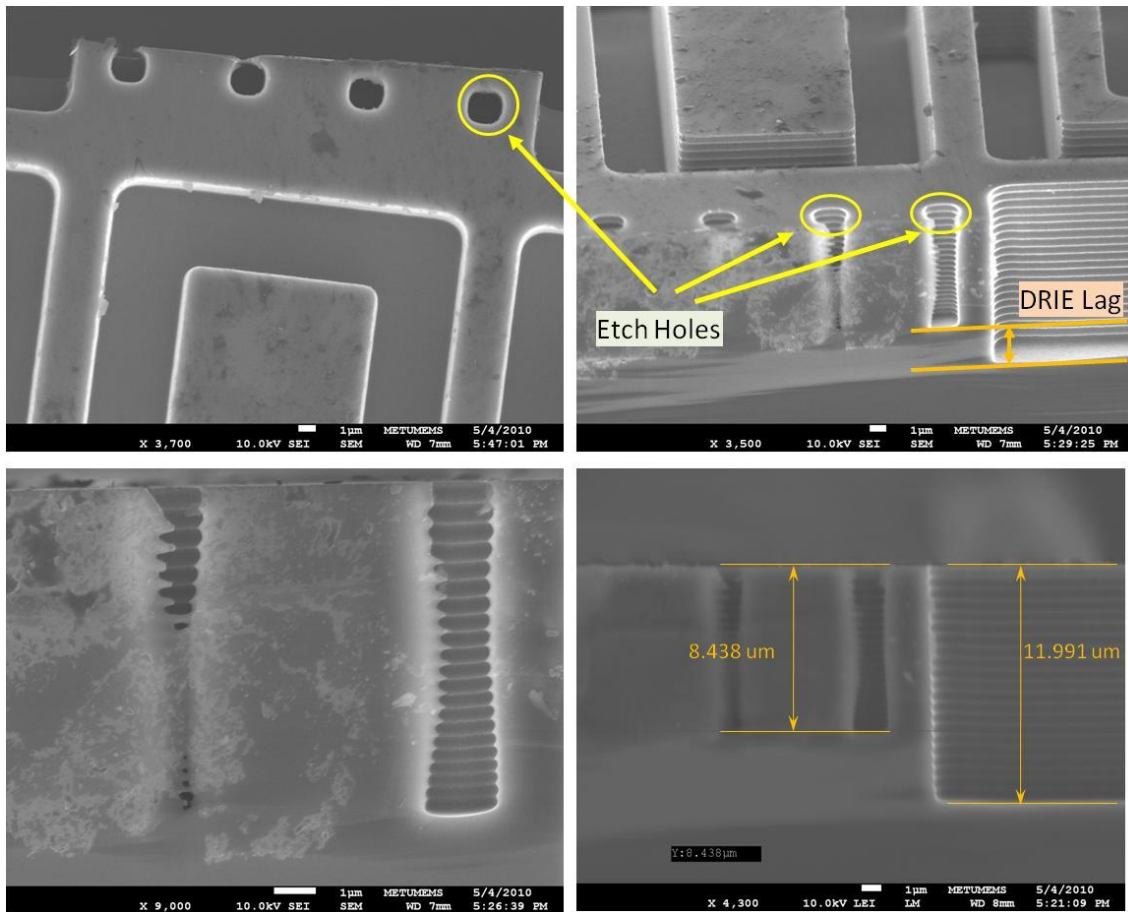


Figure 4.7 DRIE Lag problem observed at etch holes.

4.2.1.3 Parylene Coating and Etching Problems

Although parylene is a perfect material for fabricating biosensors with its biocompatible properties and isolation behavior, coating and etching of parylene cause problems during

fabrication of the gravimetric detectors. Problems during at 1st generation fabrication flow given in **Figure 4.1** arose at steps 3 and 9 respectively. In step three, the coating of the parylene is performed by LPCVD techniques and the coating is very conformal. Hence the gap spaces between rotor and stator combs are filled with parylene. To suspend the structure this filled parylene layer has to be removed but the reactive plasma during polymer removal cannot reach to these trenches. If the parylene cannot be removed effectively in step nine, the BHF step at step eleven also be prevented.

Another problem in flow in **Figure 4.1** is that the parylene is peeled off inside BHF solution. BHF attacks the interface between polymer and the silicon surface and peels the parylene off the Si surface. Since metal layers are on parylene layer, metal connections of devices are also lost.

4.2.1.4 Parylene to Metal Adhesion Problem

Metal coating onto parylene layers has adhesion problems. **Figure 4.8** show adhesion problem on parylene surface. Metal layers are broken during etching of Cr layer due to low adhesion of Cr onto parylene surface. To solve this problem oxygen plasma treatment of parylene surface is applied to roughen and activate the parylene surface prior to Cr-Au sputtering [74].

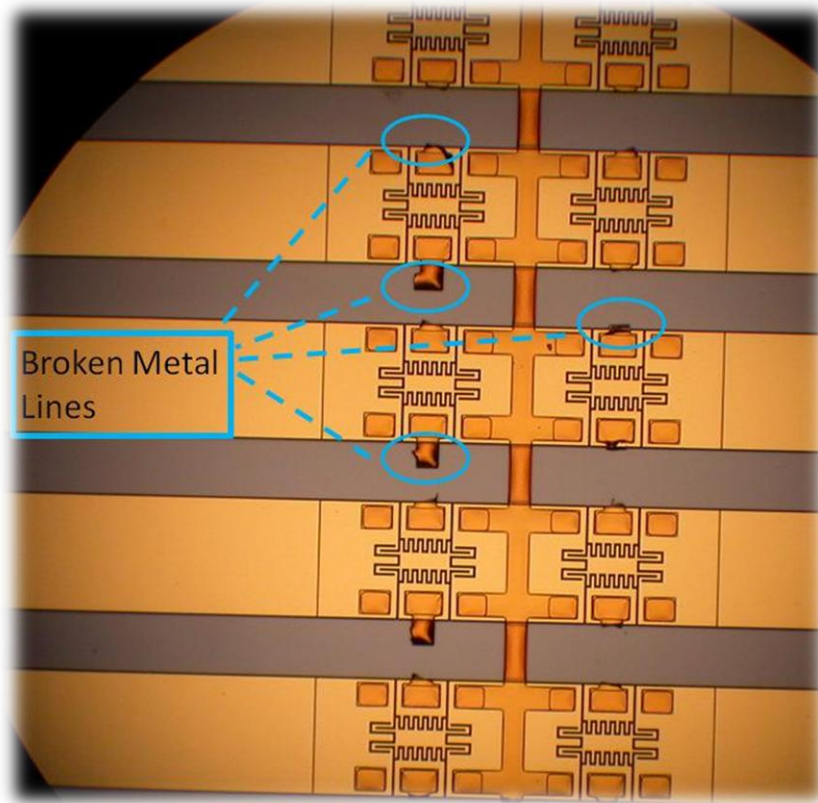
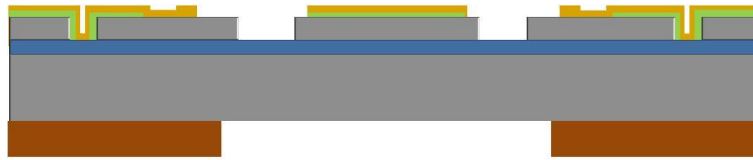


Figure 4.8 Cr-Au layer broken during metal etch due to low adhesion onto parylene surface.

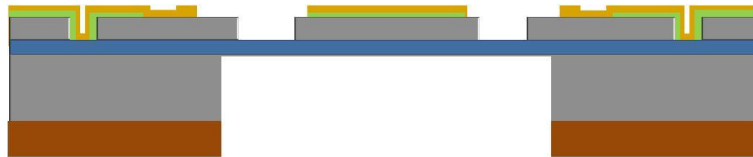
4.2.2 2nd Generation Fabrication Flow

Successful release of structures couldn't be achieved and 1st generation process flow is given up. A new mask for back side DRIE is designed for etching the handle layer beneath the microstructures to be suspended. The idea is to suspend the proof mass by etching the buried oxide layer from the back side with HF. The process flow for this 2nd fabrication flow is given in **Figure 4.9**.

The 2nd generation has also some disadvantages that the sealed area beneath the proof mass will expose to atmosphere since the back side will be removed. We also gave up this process but used the designed back side DRIE mask to realize a process similar to MicragemTM [65] process.



11. Lithography and shape PR on the back side of the wafer



12. DRIE etching of the handle wafer up to buried oxide



13. Etching oxide in BHF and PR removal devices are ready for tests

Figure 4.9 2nd generation fabrication flow.

4.2.3 3rd Generation Fabrication Flow

The designed back side DRIE mask is used to etch trenches on the glass substrates for wafer bonding. The modified fabrication flow for 3rd generation is given in **Figure 4.10**. The glass wafer is coated with Cr-Au to be used as mask for HF etching of glass during trench etching. SOI wafer is etched with DRIE mask to realize proof mass, comb fingers and springs on the substrate as before. The machined glass and SOI wafer are cleaned in

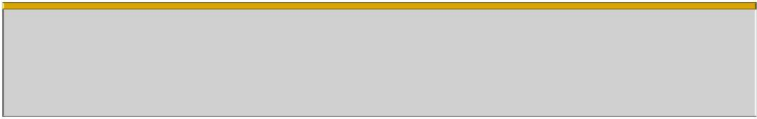
piranha solution to remove organic residues both coming from environment and DRIE Bosch process prior to wafer bonding. Sulphuric acid inside the piranha solution is hard to clean and wafers should be cleaned in DI water tanks and dried prior to wafer bonding.



1. Lithography and pattern PR



2. Active Layer pattern by DRIE with oxide as an etch stop



3. Coat metal on glass wafer

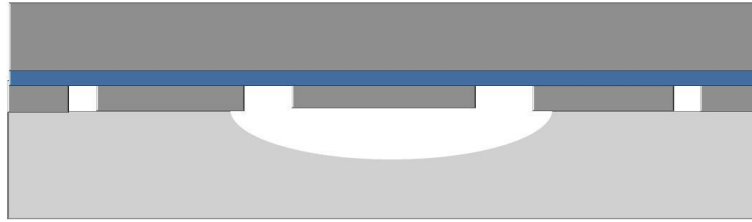


4. Lithography and pattern metal



5. HF etching of glass

Figure 4.10 3rd generation fabrication flow



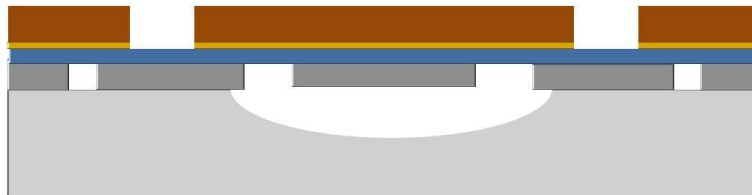
6. Anodic Bonding



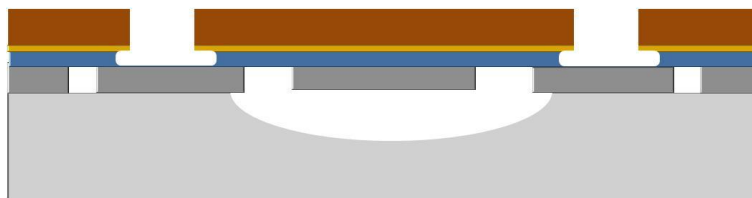
7. Dissolve handle wafer with DRIE



8. Metal coating on oxide layer



9. Lithography and pattern metal for contact opening

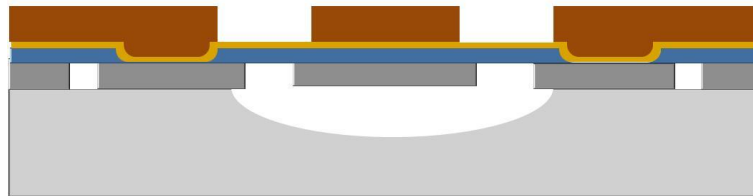


10. Oxide Patterning in BHF

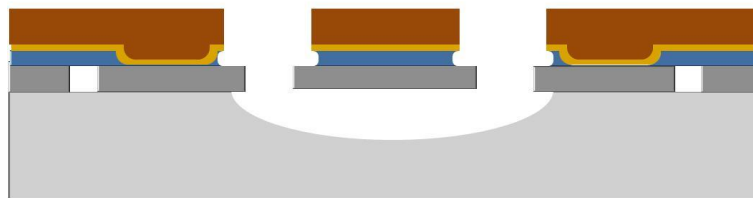
Figure 4.10 Continued.



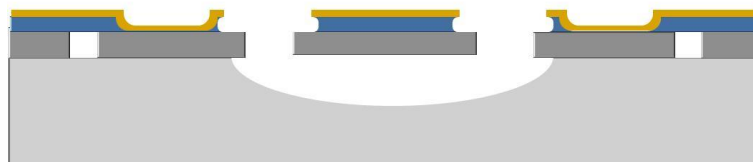
11. Remove PR and metal



12. Metallization with good step coverage and lithography for metal routing



13. Metal etch and BHF for oxide patterning



14. PR removal and devices are ready for tests

Figure 4.10 Continued.

Bonding quality is directly related with surface cleanliness of the wafers. The wafers are bonded in EVG wafer bonder at 1000V bias voltage and 1500 N force exerted on them. The bonding temperature is 400 °C. The residue after Cr-Au stripping that used for

masking HF on the glass substrate caused defect on the wafer during bonding and the bonding is prevented at this point that is shown in **Figure 4.11**.

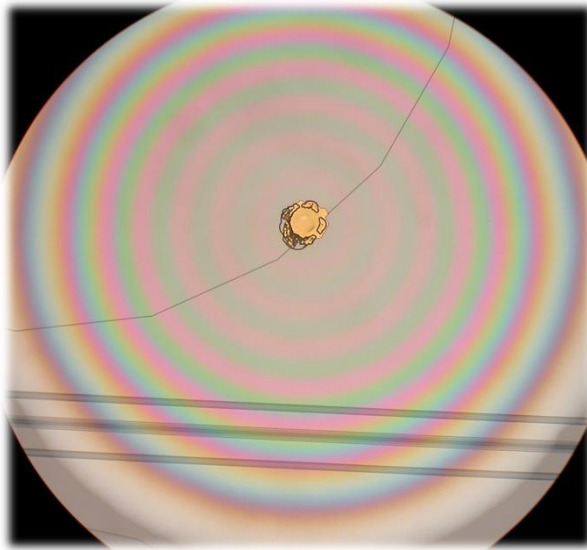


Figure 4.11 Metal residue on glass wafer prevents the bonding at this area. Light spectrum at this point shows that bonding is failed at this area.

After wafer bonding, the handle wafer on back side of the SOI wafer is etched away completely in PEGASUS DRIE system. The buried oxide is also removed completely for the first tests of the resonators on probe station without any metallization. After tests give hopeful results, at the new fabrication of the resonators the oxide layer is patterned and used as insulating layer for metallization shown in **Figure 4.10**.

The bonded devices and alignment marks are shown in **Figure 4.12** to represent the bonding quality.

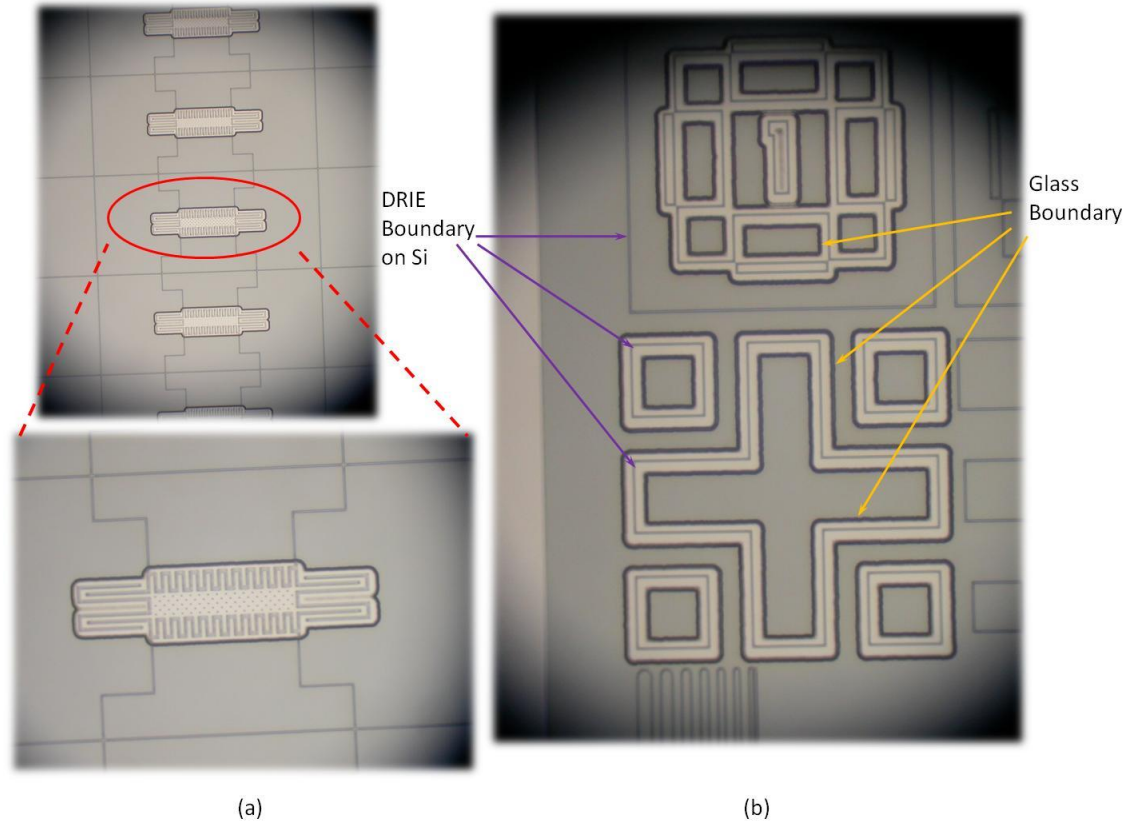


Figure 4.12 Bonding photographs in microscope (a) device photograph, (b) bonding of alignment marks.

After finishing the device layer and metallization of the structures, possible micro channel fabrication techniques are investigated and PDMS [75] is decided to be used as micro channel structural layer. PDMS is also biocompatible as parylene and used extensively in biosensors. For fabrication with PDMS, a mold layer is required and this mold is created by patterning Si test wafer with DRIE process. The patterned PDMS layer is peeled off from the Si wafer and will be bonded to patterned process wafer to form microfluidic channels. The fabrication of the top PDMS layer is given in **Figure 4.13**.

	PDMS		Glass		PR
	Silicon		Gold		



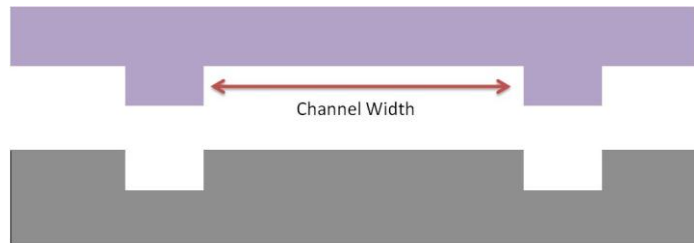
1. Lithography and pattern PR



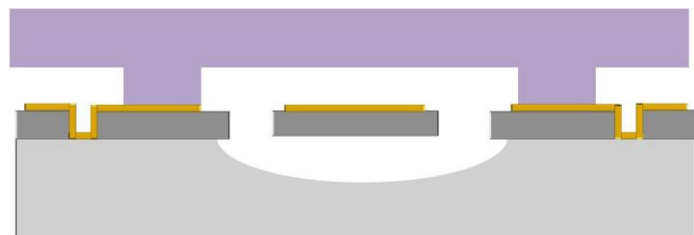
2. DRIE for channel mold



3. Remove PR and pour PDMS



4. Peel off the PDMS from Si substrate



5. Bond PDMS channel to devices

Figure 4.13 PDMS channel fabrication flow

4.3 Summary

The successful fabrication of gravimetric resonators is given at this chapter. The optimization procedure during the fabrication is given step by step and changed fabrication flows are also inserted to follow up the duration. The most suitable fabrication flow is chosen and reasons are explained for this choice of flow.

The required micro channel formation is also handled and procedure for PDMS based micro channel fabrication is given with fabricated channels.

The complete device is presented in **Figure 4.14**. The PDMS micro channel is bonded to device and the gravimetric resonators are on the channel floor.

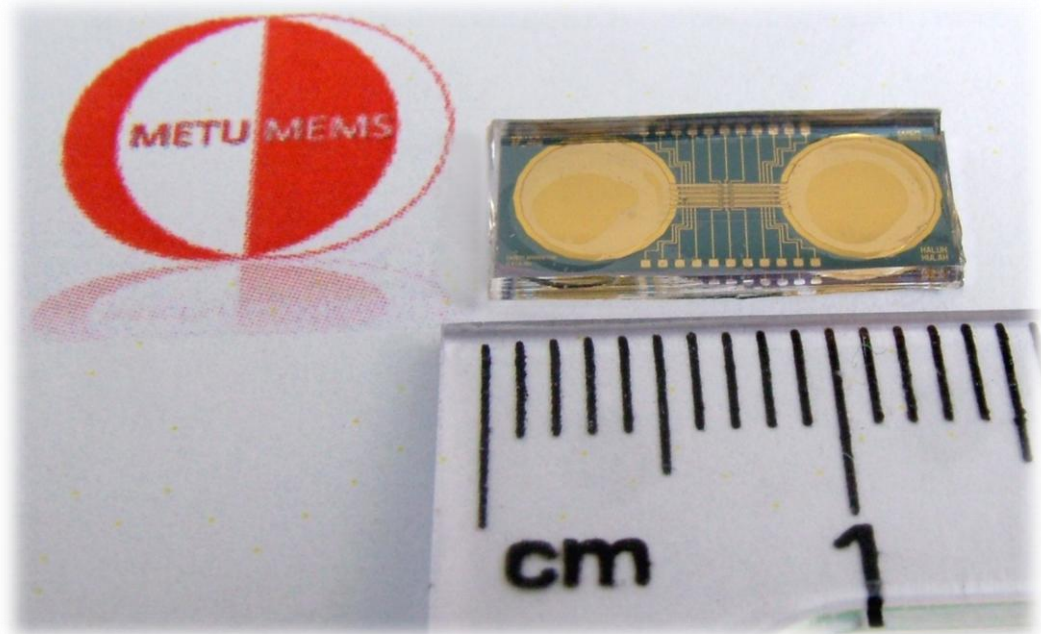


Figure 4.14 Device photograph with PDMS channels are bonded on top of devices

CHAPTER 5

TESTS AND RESULTS

This chapter presents the preliminary results of gravimetric resonator. The open loop resonance behaviors of the resonators are examined with and without stray capacitances. The interface circuit to amplify the injected current and achieve current to voltage conversion is also given.

5.1 Test Circuit and Setup

During open-loop resonance characterization tests, a stage which will be used to convert the current injected by the resonators to voltage is needed. There are two main topologies with which this task can be performed. Unity gain buffer and transimpedance amplifier. Unity gain buffers are not very suitable for relatively high frequency applications since, the input impedance of the OPAMP (usually on the order of pF) limits the maximum value of the resistor severely and hence, the noise performance.

Because of the small dimensions of the resonators fabricated for this study, their injected current magnitudes are on the order of nanoamperes. As a result, current noise performance of the TIA is quite important to have reasonable signal-to-noise ratio. To maximize the noise performance, the current noise of the opamp used should be as low as possible and the value of the resistor used as the transimpedance should be as high as possible ($i_{\text{noise}}=4kT/R$). For this purpose, an opamp with superior current noise performance and also high bandwidth has been obtained from the market (OPA 656 from Texas Instruments) and 1 MOhm was selected as the transresistance value, which is actually the maximum permissible resistance value for the required bandwidth for the

devices. The designed PCB with transimpedance amplifier and additional amplifier stages are shown in **Figure 5.1**.

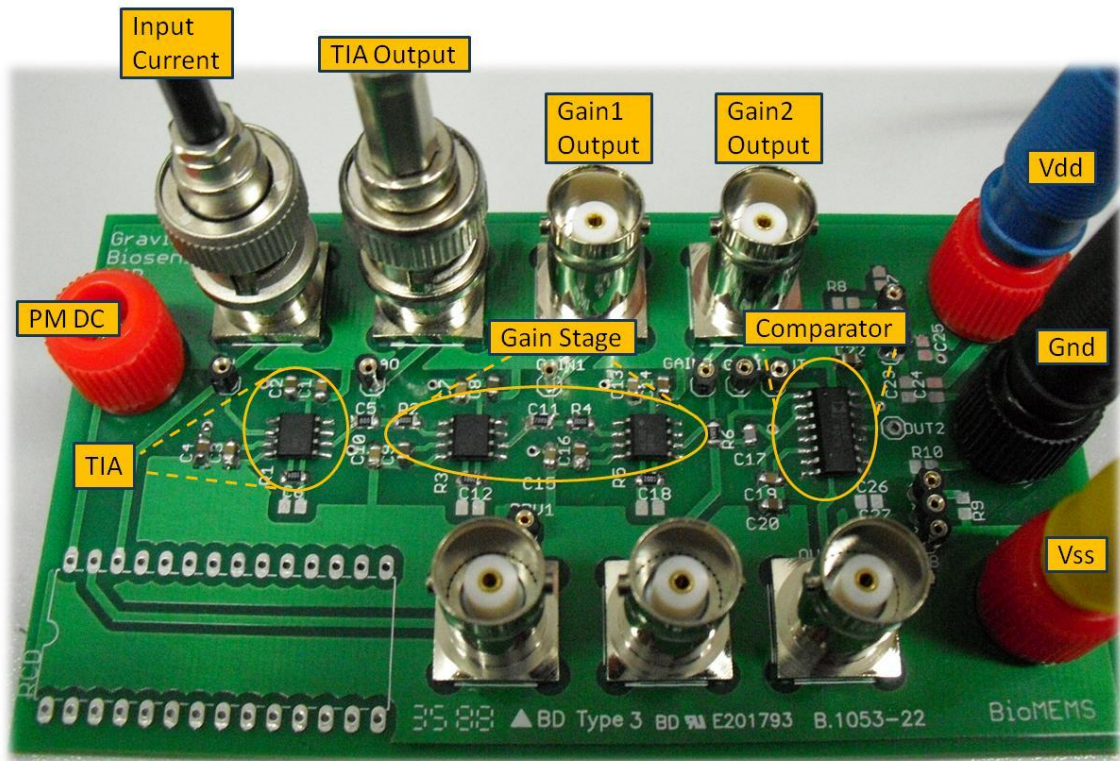


Figure 5.1 PCB photograph with TIA and amplifier stages

The test setup including the sensor and test circuit is shown in **Figure 5.2**. 4395 A Network analyzer is used during tests to show the AC response of the resonator. An AC signal with 15 dBm power (1.25 V for 50 Ω matching) is applied from the drive port of the resonator and a DC voltage of 50 V is applied to the proof mass. The sense output current of the resonator is fed to the transimpedance amplifier. The output of the amplifier is connected to the input port of the network analyzer. Network analyzer sweeps the frequency and meanwhile plots the magnitude and phase responses of the resonator. Total gain of the transimpedance amplifier stage is approximately 115 dB.

This means that actual resonator magnitude will be 118 dB lower than the obtained results during the tests.

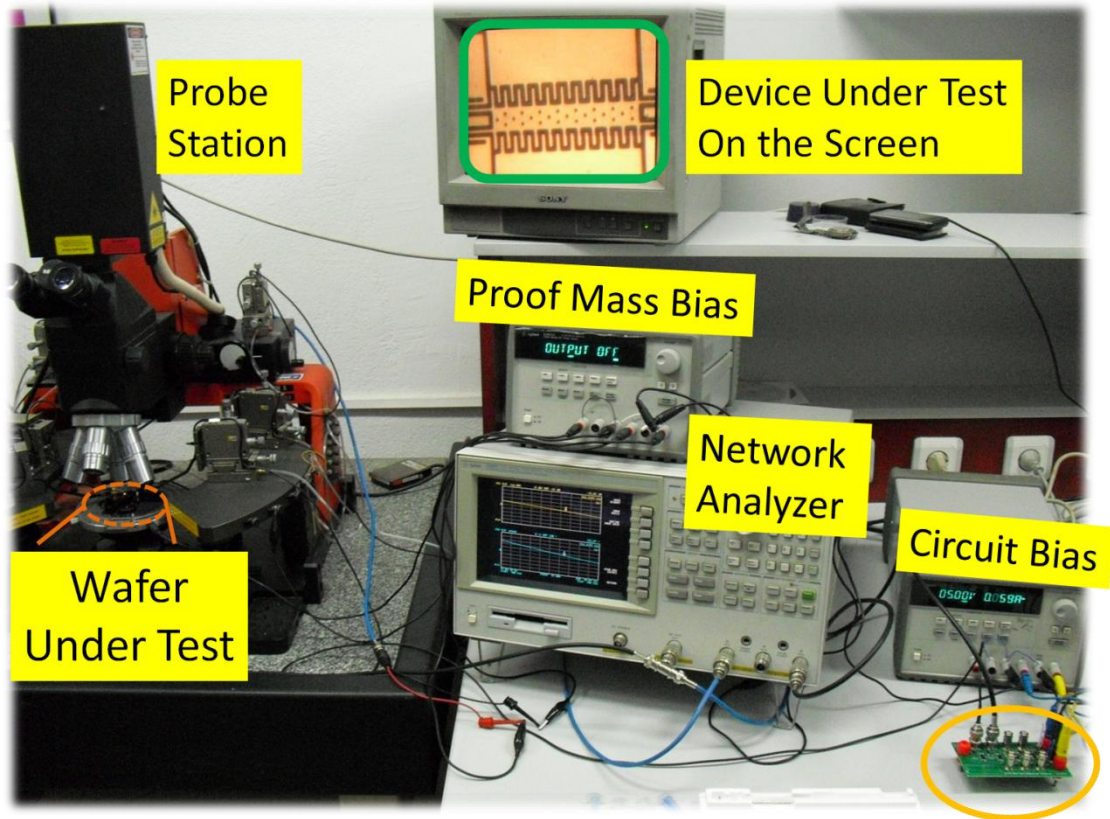


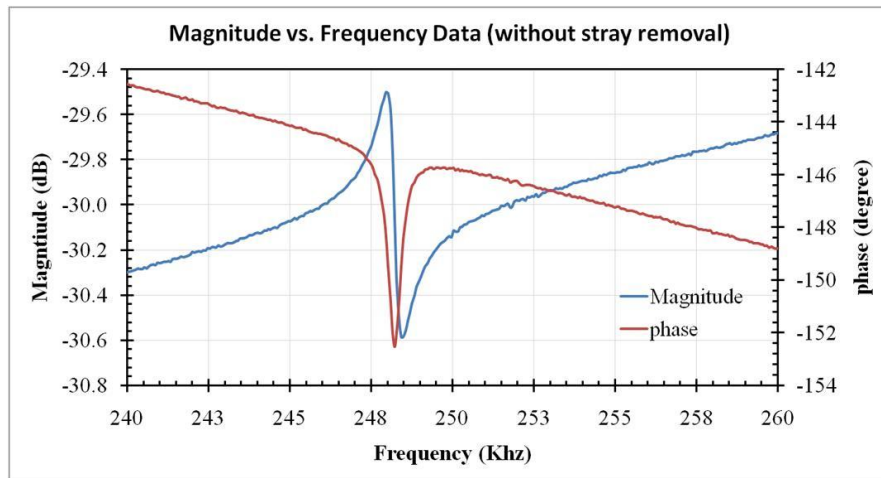
Figure 5.2 Test setup with sensor and test circuit

5.2 Open Loop Test Results

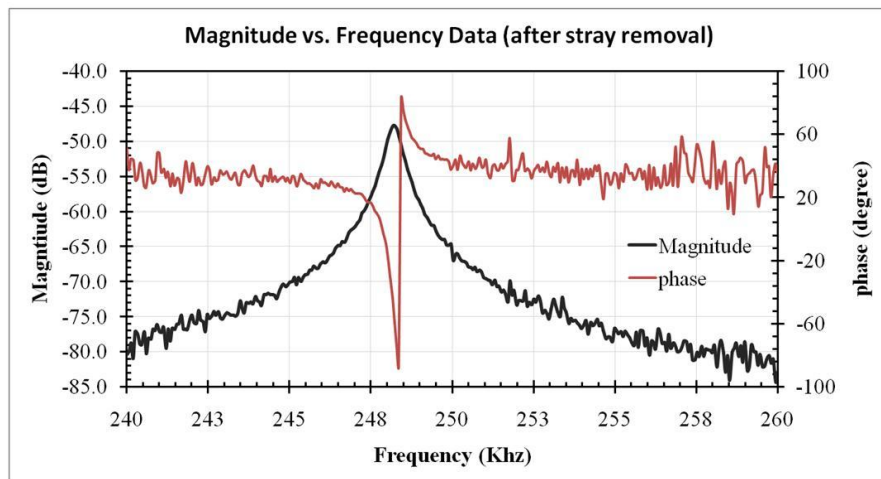
The devices are tested for open loop AC response and the resonator quality factors are determined. The stray capacitance between the drive and sense port as mentioned in section 3.2.2 was a problem during the tests hence the filter characteristics is vanished under the stray behavior. To eliminate the effect of stray capacitance, tests are performed twice for each device and the first test is performed when the DC voltage is ON. Then

the DC voltage is turned OFF and the data are stored again. After taking these sets of data, a vector subtraction is performed and stray data are subtracted from the test data.

Effect of stray capacitance on the sensor performance is represented in **Figure 5.3**. The magnitude response is severely increased after stray removal.



(a)



(b)

Figure 5.3 Effect of stray capacitance on sensor performance for device with code 16030A4F80B

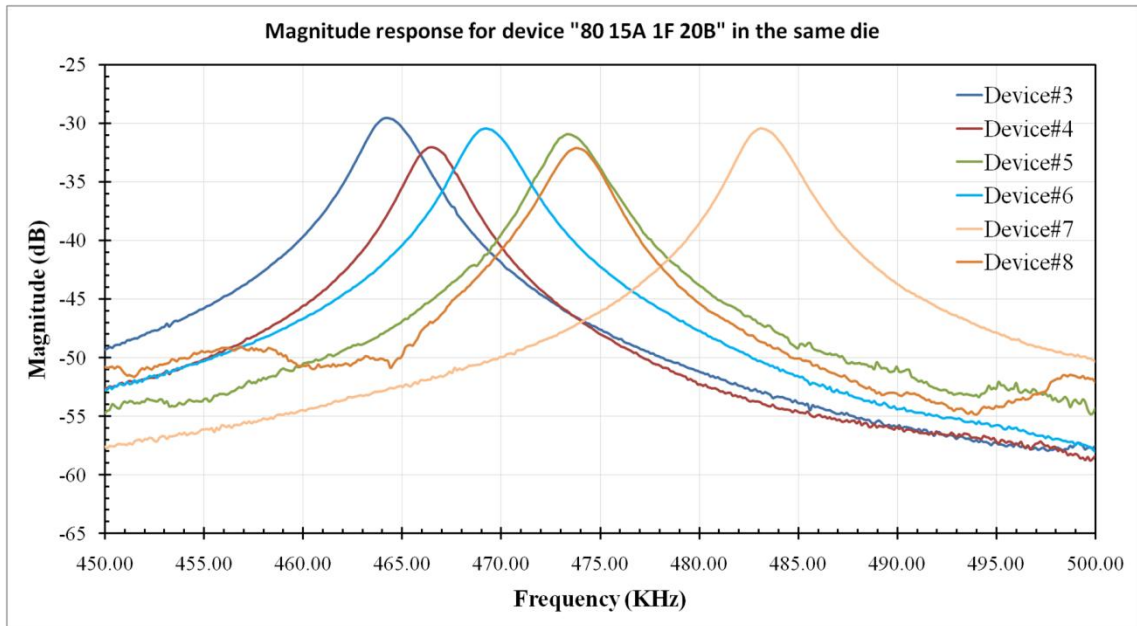
The magnitude and phase responses for one device with code 80 15A 1F 20B are inspected. The results change according to device location on the wafer, the change is obvious even in the same die as can be seen on **Figure 5.4**. The reason for such different behaviors is the problems at DRIE and lithography that are addressed at fabrication chapter.

The quality factors and resonance frequencies of the devices are given in **Table 5.1**. When compared with the simulation results almost all devices are well fit into the simulations. The effect of undercuts and thinning is approximately included to the simulations in both COMSOL and MATLAB.

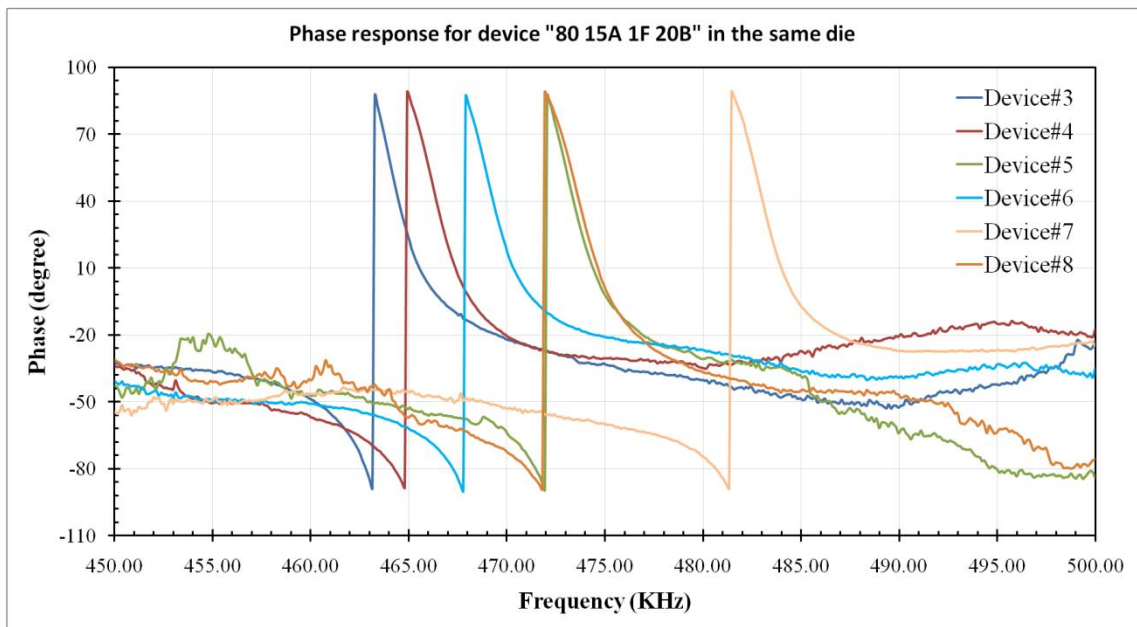
Table 5.1 Simulation Results in COMSOL and MATLAB are compared with test results

Device Code	COMSOL (f_n)	MATLAB (f_n)	Test Results	
			Quality Factor	f_n
16030A4F40B	706.36 kHz *	688 kHz	~1200	~640 kHz
16030A4F80B	387.00 kHz	243 kHz	~470	~250 kHz
8030A4F40B	1.09 MHz *	973 kHz	----	----
8030A2F40B	384.69 kHz	315 kHz	~330	~350 kHz
8015A4F40B	1.10 MHz*	1.28 MHz	----	----
8015A2F40B	475.02 kHz	383 kHz	~290	434 kHz
8015A1F20B	450.24 kHz	334 kHz	~200	~495 kHz
4015A2F40B	626.57 kHz	608 kHz	~350	~560 kHz
4015A2F20B	2.12 MHz	1.71 MHz	~1800	~1.9 MHz
4015A1F20B	608.16 kHz	472 kHz	~130	~440 kHz

* The given COMSOL responses are belong to 2nd mode, the 1st mode is out of plane



(a)



(b)

Figure 5.4 Test results for devices with code 80 15A 1F 20B on the same die. (a) Magnitude responses, (b) phase responses after stray removal.

Test magnitude and phase responses after stray removal for other type of devices are given in **Figure 5.5**.

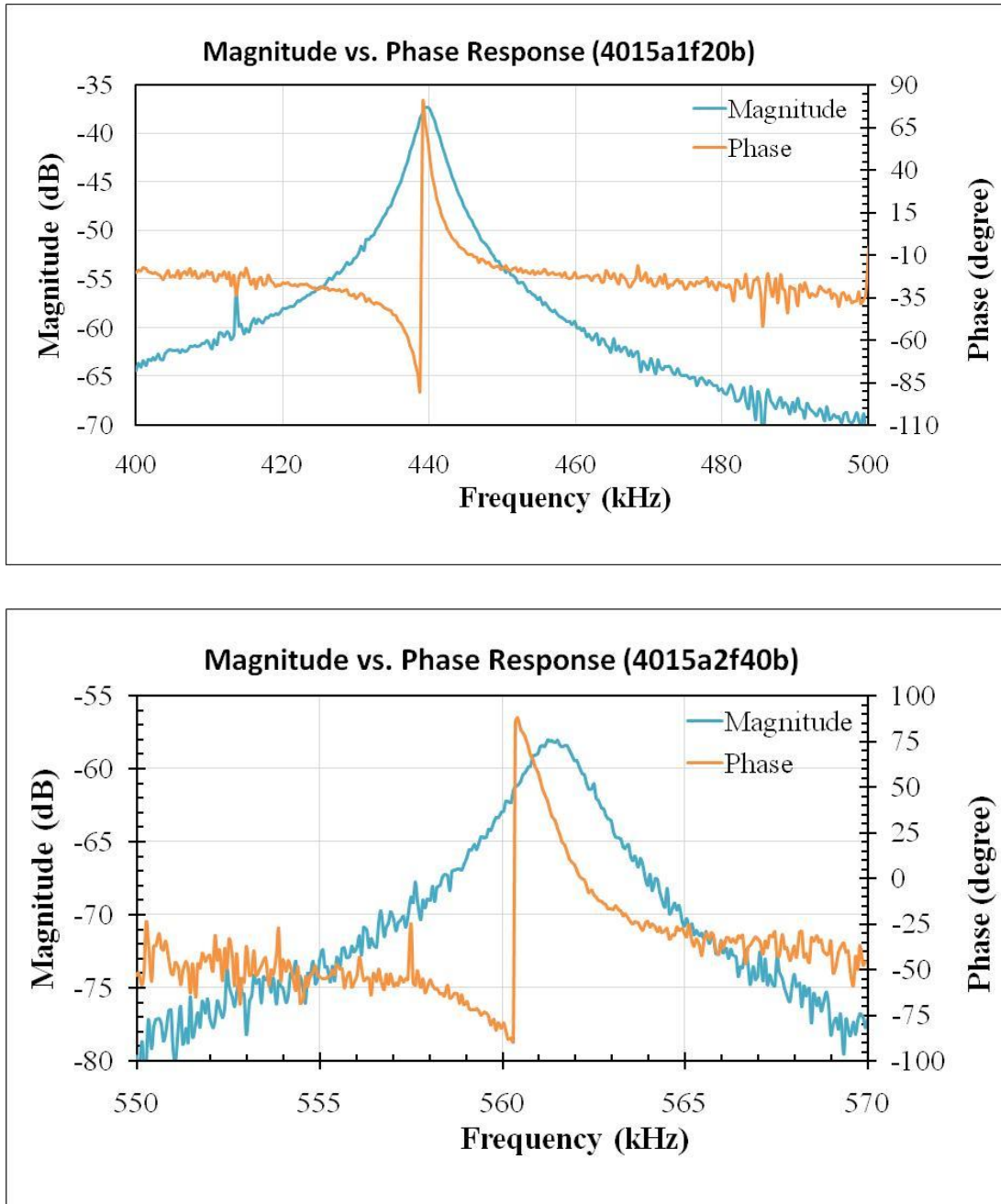


Figure 5.5 Magnitude vs. frequency response for each device after stray removal

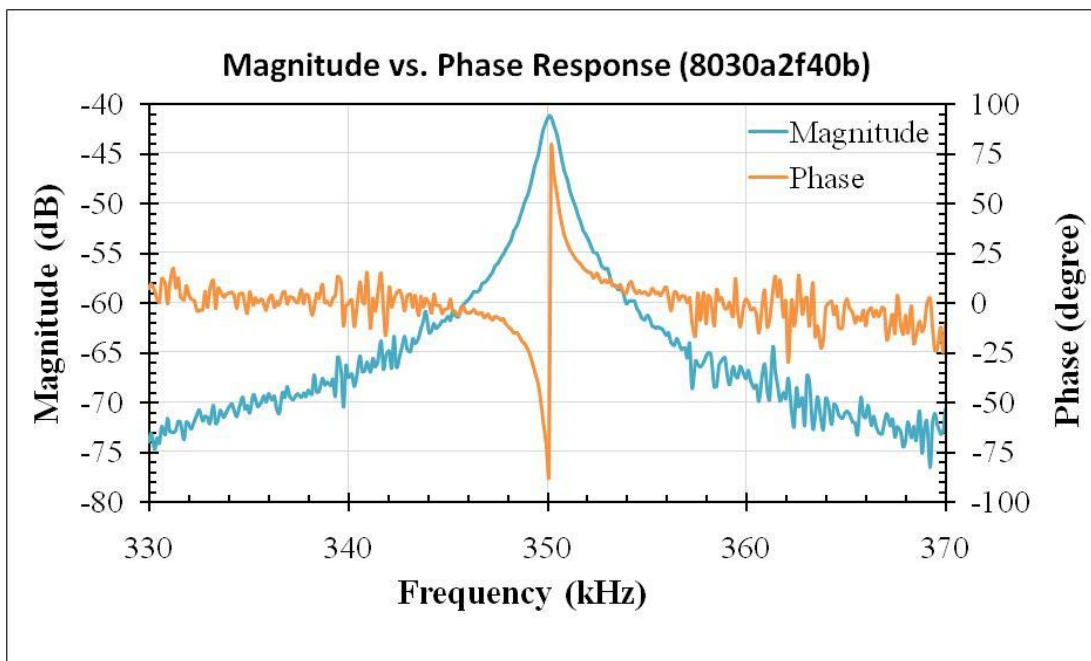
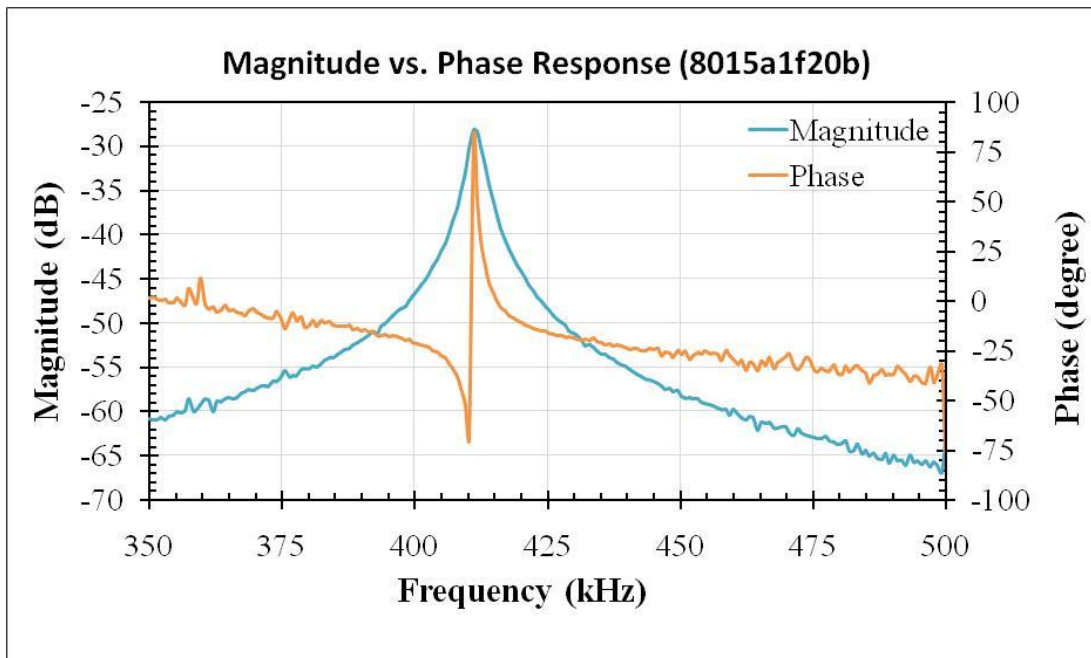


Figure 5.5 Continued.

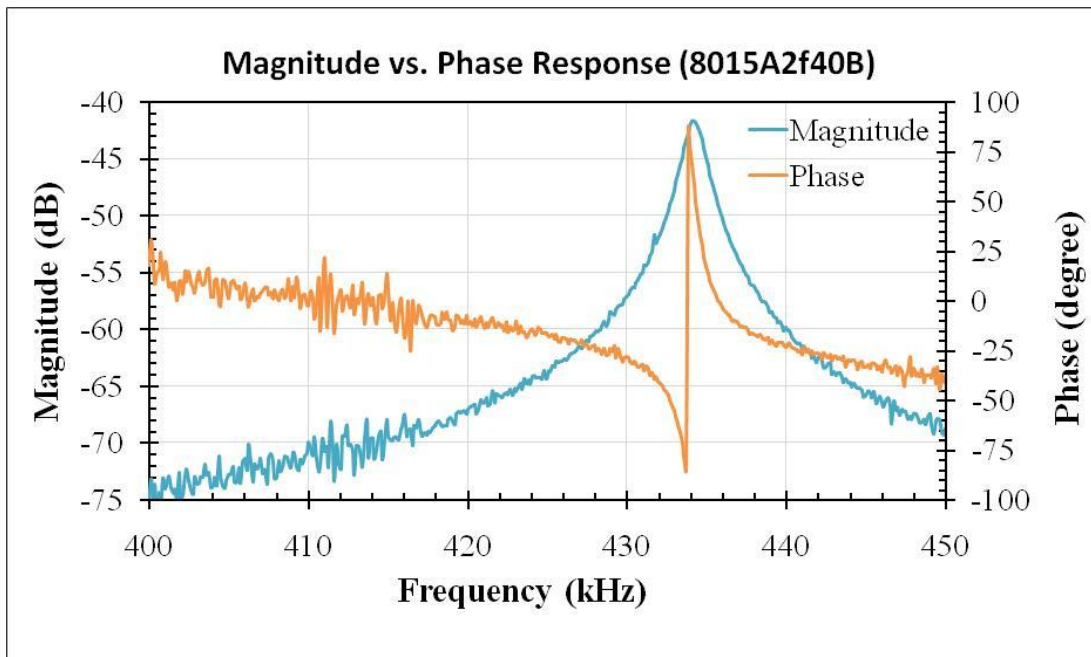
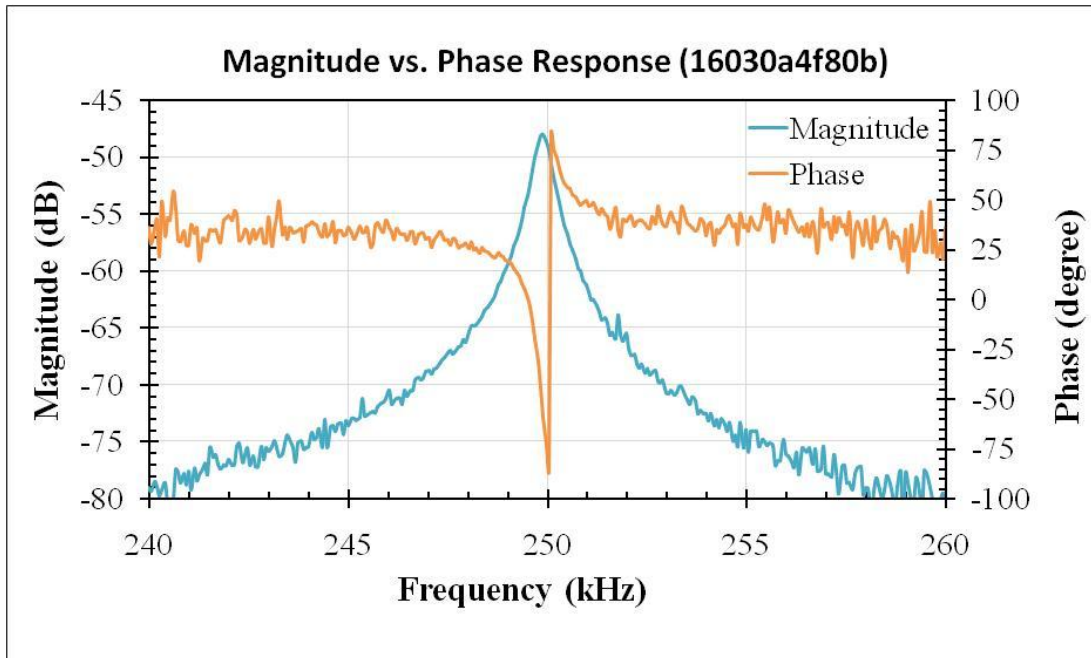


Figure 5.5 Continued.

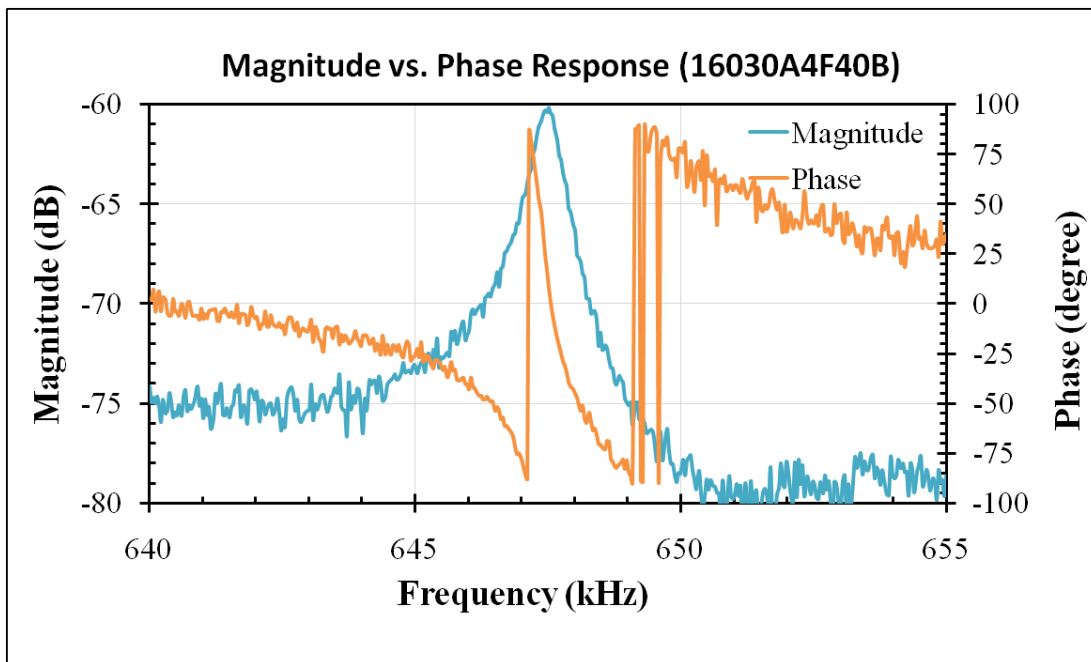
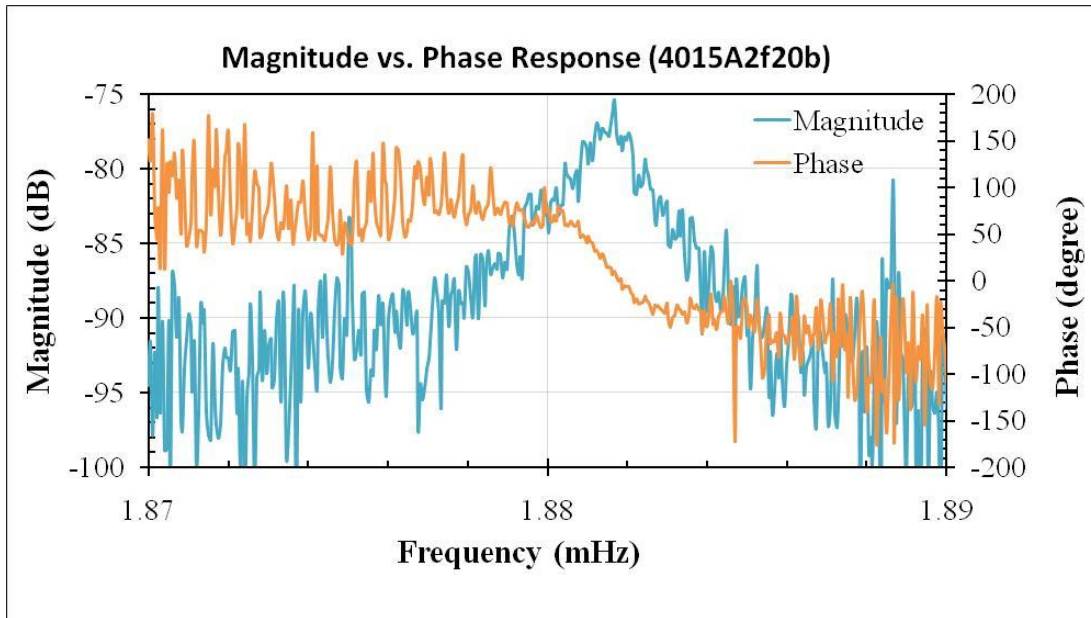


Figure 5.5 Continued.

5.3 Mass Detection tests on Gravimetric Resonators

Latex beads with 3 μm diameter are used during the first mass detection tests and successful results are observed. Mass of one bead is calculated as 14.127 pg and this amount of mass is detected on the proof mass, but do not forget that beads have a coefficient of variation of 10%. The attached bead on device with code 4015A2F20B is shown in **Figure 5.6**.

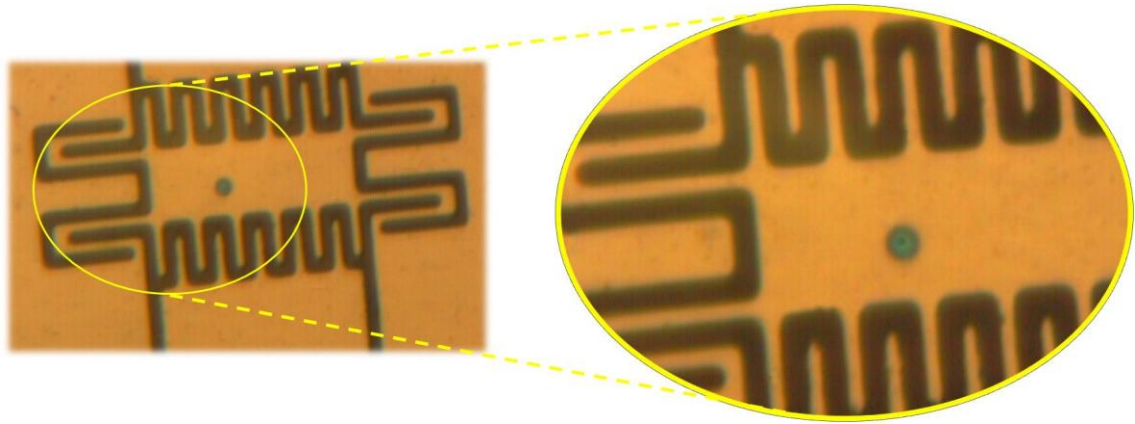


Figure 5.6 Bead attached to device with code 4015A2F20B

Figure 5.7 shows the first mass detection results on the device with code 4015A2F20B. The injected current for this type of device is very close to the input referred current noise of the electronics interface and hence the output is very noisy. However the resonance frequency change of 2.51 kHz can be clearly observed on the response. For this type of device the mass sensitivity can be calculated by,

$$\frac{\partial m}{\partial f} = \frac{k}{2\pi^2 f_n^3} = 6.16 \text{ fg/Hz}$$

The result above gives idea about the theoretical mass sensitivity of the device. The frequency change of 2.51 kHz for added mass of 14.127 pg gives a mass sensitivity of 5.91 fg/Hz which is consistent with the theoretical result. The mass sensitivity is

assumed to be linear since the loaded mass is smaller than the attached bead mass, but this does not mean that we can catch 5.91 fg on these structures since the reading cannot be performed in 1 Hz bandwidth. The error between the calculated and tested results is 4.23 % which is also consistent with the coefficient variations of the beads (10%).

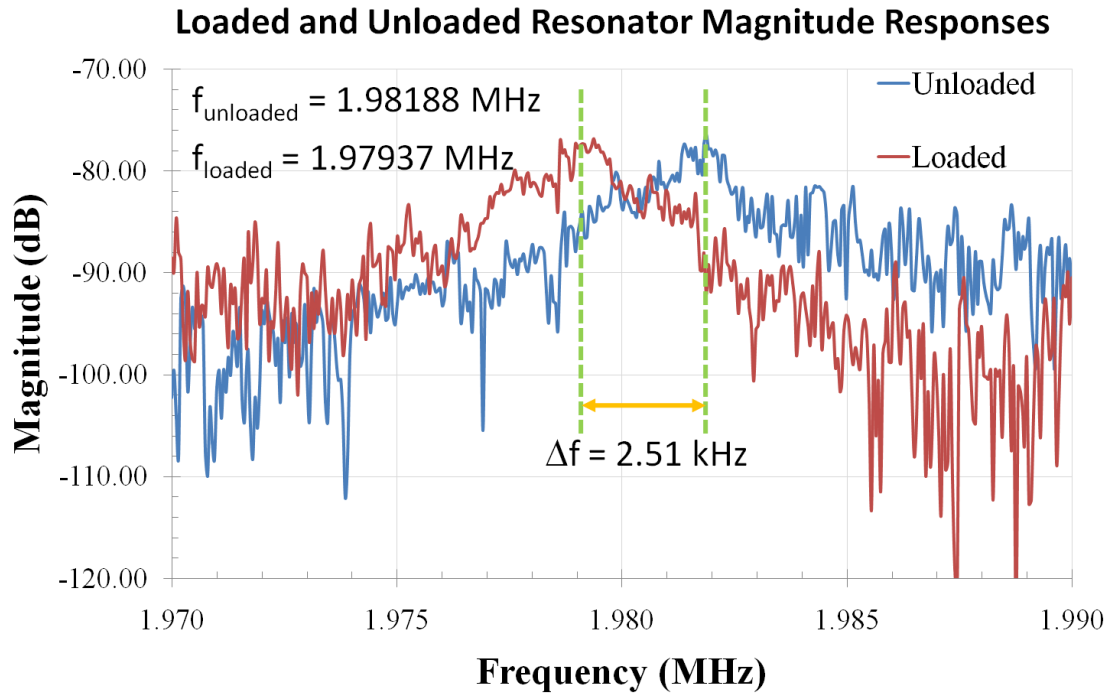


Figure 5.7 Loaded and unloaded test results for device 4015A2F20B.

Another mass detection test is performed with device code 40 15A 2F 40B. Multiple beads on the same proof mass are tested respectively and results are presented in **Figure 5.8**.

The attached beads are shown in **Figure 5.9**. Results show that the response to attached beads are not linear but the reason is that the beads are not similar. Therefore if we can talk about a mean sensitivity, sensitivity is 27.5 fg/Hz for this device.

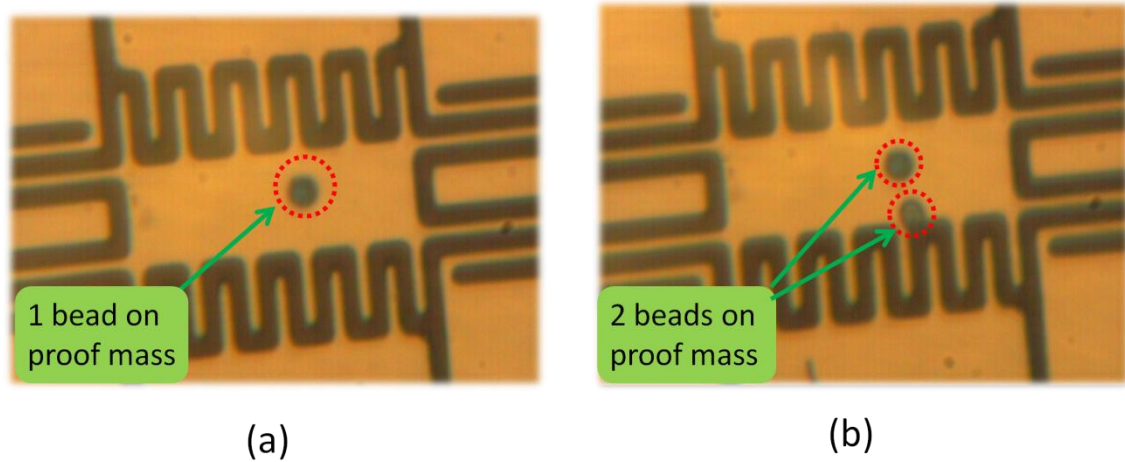
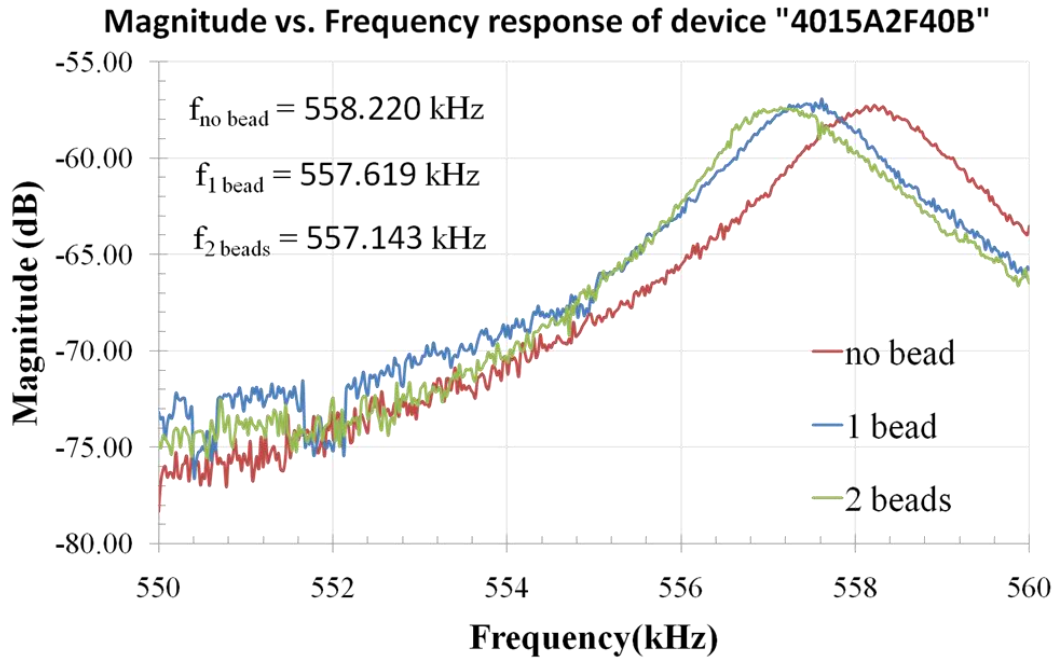


Figure 5.9 Attached beads on the proof mass (a) First bead is attached and tested, (b) Another bead is attached and tested.

CHAPTER 6

CONCLUSION AND FUTURE WORK

In this research, a gravimetric resonator for rare cell detection purposes is developed and design, simulation, and fabrication of the sensor are presented. The research can be divided into sub tasks and these tasks can be summarized as follows:

- Theory of second order spring mass damper system is examined briefly to understand the mechanism of resonance. Electrostatic capacitive actuation and sensing are selected as the driving mechanisms of the resonator and an electrical equivalent circuit for fast analysis of different designs including the mechanical resonator, drive and sense parts is constructed. Damping analysis of the lateral resonator is given and gravimetric mass detector performance parameters are discussed.
- Design of mechanical structure of the lateral resonator and simulations are performed successfully. Main emphasis of the design is on mass detection and also micro channel formation is also considered during the design. The principle behind the lateral motion is to decrease the squeeze film damping effects. Embedding resonators inside a micro channel and performing tests during the fluid flow over the resonator, thanks to parylene surface, enables online monitoring of the cells which is the challenging topic in state of the art BioMEMS researches.
- Mechanical dimensions of the resonators are determined by taking the mass sensitivity to account and frequency of resonance tried to be increased since it also increases the mass sensitivity of the resonators. Spring beams are designed accordingly to increase the frequency but also the injected current is taken into

account since the injected current should be kept over the noise level at the output of the resonator.

- Thin film parylene is planned to be used over the resonators to enable online monitoring by simply preventing current flow over the analysis fluid due to its perfect electrical properties. Hydrophobicity is also guaranteed over comb fingers due to parylene coating and fluid penetration between the comb fingers and beneath the proof mass is planned to be prevented by parylene coating over comb fingers which decreases the damping over the resonator.
- Fabrication of the resonators is optimized and optimization procedure is explained in detail. Suspending of the resonators was the most challenging part and be eliminated by using SOI on glass fabrication technique. Micro channel fabrication optimization is also discussed and PDMS is chosen to be the channel material due to its biocompatibility. The problems emerging from metal adhesion over polymer surfaces are also eliminated.
- Test setup for measuring the open loop responses of the resonators is prepared and tests are performed. Effect of stray capacitance is eliminated by simply repeating the tests and performing a vector subtraction. First open loop responses of the resonators are taken and results are compared with the simulations. The discrepancies between the simulations and the test results are discussed and fabrication limitations and undercuts are put in charge for these discrepancies. Effect of device location over the wafer is given and discussed. The open loop test results for each device is presented and quality factors of these devices are also given which will be useful for mass detection. A resonator frequency range from 250 kHz to 1.9 MHz is shown for different device types and quality factors of 130 up to 1800 are experimentally shown and results are discussed. Polystyrene beads are used for tests and single and multiple bead detections are shown experimentally. A frequency change of 2.51 kHz is observed for one bead attachment onto the proof mass which is the most sensitive device. Multiple bead detection is also observed on the same proof mass. The required electronics

interface for the tests is prepared by designing a TIA (transimpedance amplifier) over a PCB with filters to reduce noise is also presented.

- Bioactivation protocol over the resonator is also developed, but this part is out of the scope of this thesis.

Future work over the project can be summarized as:

- Open loop transfer function analysis of the resonators inside fluid should be performed after thin parylene thickness optimization over the comb fingers. Effect of parylene and fluid should be addressed carefully.
- Sealing of the micro channels should be ensured during the PDMS fabrication. Alternative channel fabrication techniques over suspended structures should be investigated.
- Closed loop operation of the resonators should also be tested. The closed loop circuit is already finished but some modifications will be required over both fabrication and electronics to combine all of the system. Both air and fluid tests should be performed and effect of parylene over the closed loop operation should be taken into care.
- Developed bioactivation protocol should also be tested over the resonators and functionality of the sensor inside fluid environment should be ensured. After functional tests, tests with bacteria and cells should be performed for detection.
- The packaging issues should also be discussed to realize a self oscillating gravimetric mass detector.
- Successful results may direct the project to design monolithic gravimetric mass detectors including sensor and electronics side by side which will reduce the noise and boost the sensor performance.

REFERENCES

- [1] L. N. Sun, *et al.*, "A silicon integrated micro nano-positioning XY-stage for nano-manipulation," *Journal of Micromechanics and Microengineering*, vol. 18, pp. -, Dec 2008.
- [2] X. Liu, *et al.*, "A MEMS stage for 3-axis nanopositioning," *Journal of Micromechanics and Microengineering*, vol. 17, pp. 1796-1802, Sep 2007.
- [3] R. Bashir, "BioMEMS: state-of-the-art in detection, opportunities and prospects," *Advanced Drug Delivery Reviews*, vol. 56, pp. 1565-1586, Sep 22 2004.
- [4] R. Bashir, "An Introduction to BioMEMS and Bionanotechnology," ed, 2005.
- [5] M. Bao, *Analysis and Design Principles of MEMS devices*, 2005.
- [6] SCS. Parylene Conformal Coating Specifications & Properties [Online]. Available: <http://www.scscookson.com/parylene/properties.cfm>, 26.08.2010
- [7] PDMS (polydimethylsiloxane) Properties [Online]. Available: <http://web.mit.edu/6.777/www/matprops/pdms.htm>, 26.08.2010
- [8] J. Z. Hilt, *et al.*, "Ultrasensitive biomems sensors based on microcantilevers patterned with environmentally responsive hydrogels," *Biomedical Microdevices*, vol. 5, pp. 177-184, Sep 2003.
- [9] S. J. Hyun, *et al.*, "Mechanical detection of liposomes using piezoresistive cantilever," *Sensors and Actuators B-Chemical*, vol. 117, pp. 415-419, Oct 12 2006.
- [10] Y. I. Kim, *et al.*, "Biosensors for label free detection based on RF and MEMS technology," *Sensors and Actuators B-Chemical*, vol. 119, pp. 592-599, Dec 7 2006.
- [11] X. Cheng, *et al.*, "Cell detection and counting through cell lysate impedance spectroscopy in microfluidic devices," *Lab on a Chip*, vol. 7, pp. 746-755, Jun 2007.
- [12] Y. I. Kim, *et al.*, "Development of LC resonator for label-free biomolecule detection," *Sensors and Actuators a-Physical*, vol. 143, pp. 279-285, May 16 2008.

- [13] A. Kanapitsas, *et al.*, "Dielectric properties during apoptosis in peripheral blood cells from chronic lymphocytic leukaemia patients," *Ieee Transactions on Dielectrics and Electrical Insulation*, vol. 13, pp. 1057-1062, Oct 2006.
- [14] J. Suehiro, *et al.*, "Selective detection of bacteria by a dielectrophoretic impedance measurement method using an antibody-immobilized electrode chip," *Sensors and Actuators B-Chemical*, vol. 119, pp. 319-326, Nov 24 2006.
- [15] J. Suehiro, *et al.*, "Quantitative estimation of biological cell concentration suspended in aqueous medium by using dielectrophoretic impedance measurement method," *Journal of Physics D-Applied Physics*, vol. 32, pp. 2814-2820, Nov 7 1999.
- [16] M. K. Baller, *et al.*, "A cantilever array-based artificial nose," *Ultramicroscopy*, vol. 82, pp. 1-9, Feb 2000.
- [17] C. Amatore, *et al.*, "Electrochemical detection in a microfluidic device of oxidative stress generated by macrophage cells," *Lab on a Chip*, vol. 7, pp. 233-238, 2007.
- [18] T. Sannomiya, *et al.*, "Optical sensing and determination of complex reflection coefficients of plasmonic structures using transmission interferometric plasmonic sensor," *Review of Scientific Instruments*, vol. 81, pp. -, May 2010.
- [19] S. Nagrath, *et al.*, "Isolation of rare circulating tumour cells in cancer patients by microchip technology," *Nature*, vol. 450, pp. 1235-U10, Dec 20 2007.
- [20] T. Endo, *et al.*, "Label-free detection of peptide nucleic acid-DNA hybridization using localized surface plasmon resonance based optical biosensor," *Analytical Chemistry*, vol. 77, pp. 6976-6984, Nov 1 2005.
- [21] D. Z. Jin, *et al.*, "High-mode resonant piezoresistive cantilever sensors for tens-femtogram resolvable mass sensing in air," *Journal of Micromechanics and Microengineering*, vol. 16, pp. 1017-1023, May 2006.
- [22] V. Dauksaite, *et al.*, "Antibody-based protein detection using piezoresistive cantilever arrays," *Nanotechnology*, vol. 18, pp. -, Mar 28 2007.
- [23] A. Gupta, *et al.*, "Detection of bacterial cells and antibodies using surface micromachined thin silicon cantilever resonators," *Journal of Vacuum Science & Technology B*, vol. 22, pp. 2785-2791, Nov-Dec 2004.

- [24] K. Park, *et al.*, "Living cantilever arrays' for characterization of mass of single live cells in fluids," *Lab on a Chip*, vol. 8, pp. 1034-1041, 2008.
- [25] A. P. Davila, *et al.*, "Microresonator mass sensors for detection of Bacillus anthracis Sterne spores in air and water," *Biosensors & Bioelectronics*, vol. 22, pp. 3028-3035, Jun 15 2007.
- [26] A. Gupta, *et al.*, "Single virus particle mass detection using microresonators with nanoscale thickness," *Applied Physics Letters*, vol. 84, pp. 1976-1978, Mar 15 2004.
- [27] T. Thundat, *et al.*, "Vapor Detection Using Resonating Microcantilevers," *Analytical Chemistry*, vol. 67, pp. 519-521, Feb 1 1995.
- [28] B. Ilic, *et al.*, "Single cell detection with micromechanical oscillators," *Journal of Vacuum Science & Technology B*, vol. 19, pp. 2825-2828, Nov-Dec 2001.
- [29] J. H. Seo and O. Brand, "High Q-factor in-plane-mode resonant microsensor platform for gaseous/liquid environment," *Journal of Microelectromechanical Systems*, vol. 17, pp. 483-493, Apr 2008.
- [30] J. H. Lee, *et al.*, "Effect of mass and stress on resonant frequency shift of functionalized Pb(Zr_{0.52}Ti_{0.48})O₃ thin film microcantilever for the detection of C-reactive protein," *Applied Physics Letters*, vol. 84, pp. 3187-3189, Apr 19 2004.
- [31] G. H. Wu, *et al.*, "Bioassay of prostate-specific antigen (PSA) using microcantilevers," *Nature Biotechnology*, vol. 19, pp. 856-860, Sep 2001.
- [32] B. Boonliang, *et al.*, "A focused-ion-beam-fabricated micro-paddle resonator for mass detection," *Journal of Micromechanics and Microengineering*, vol. 18, pp. -, Jan 2008.
- [33] J. H. Lee, *et al.*, "Label free novel electrical detection using micromachined PZT monolithic thin film cantilever for the detection of C-reactive protein," *Biosensors & Bioelectronics*, vol. 20, pp. 269-275, Sep 15 2004.
- [34] T. Alava, *et al.*, "Silicon-based micromembranes with piezoelectric actuation and piezoresistive detection for sensing purposes in liquid media," *Journal of Micromechanics and Microengineering*, vol. 20, pp. -, Jul 2010.

- [35] A. K. Gupta, *et al.*, "Anomalous resonance in a nanomechanical biosensor," *Proceedings of the National Academy of Sciences of the United States of America*, vol. 103, pp. 13362-13367, Sep 5 2006.
- [36] I. Zine-El-Abidine and P. Yang, "A tunable mechanical resonator," *Journal of Micromechanics and Microengineering*, vol. 19, pp. -, Dec 2009.
- [37] D. J. Young, *et al.*, "Silicon carbide MEMS-resonator-based oscillator," *Journal of Micromechanics and Microengineering*, vol. 19, pp. -, Nov 2009.
- [38] V. Mukundan and B. L. Pruitt, "MEMS Electrostatic Actuation in Conducting Biological Media," *Journal of Microelectromechanical Systems*, vol. 18, pp. 405-413, Apr 2009.
- [39] K. B. Lee, *et al.*, "A closed-form approach for frequency tunable comb resonators with curved finger contour," *Sensors and Actuators a-Physical*, vol. 141, pp. 523-529, Feb 15 2008.
- [40] P. S. Riehl, *et al.*, "Electrostatic charge and field sensors based on micromechanical resonators," *Journal of Microelectromechanical Systems*, vol. 12, pp. 577-589, Oct 2003.
- [41] A. P. Lee, *et al.*, "Vertical-actuated electrostatic comb drive with in situ capacitive position correction for application in phase shifting diffraction interferometry," *Journal of Microelectromechanical Systems*, vol. 12, pp. 960-971, Dec 2003.
- [42] L. W. Lin, *et al.*, "Micro Electromechanical Filters for Signal-Processing," *Ieee Micro Electro Mechanical Systems : An Investigation of Micro Structures, Sensors, Actuators, Machines and Robots*, pp. 226-231 237, 1992.
- [43] T. Chen, *et al.*, "A hybrid-type electrostatically driven microgripper with an integrated vacuum tool," *Sensors and Actuators a-Physical*, vol. 158, pp. 320-327, Mar 2010.
- [44] K. Wang, *et al.*, "An electrostatic zigzag transmissive microoptical switch for MEMS displays," *Journal of Microelectromechanical Systems*, vol. 16, pp. 140-154, Feb 2007.
- [45] S. E. Alper, *et al.*, "A Compact Angular Rate Sensor System Using a Fully Decoupled Silicon-on-Glass MEMS Gyroscope," *Journal of Microelectromechanical Systems*, vol. 17, pp. 1418-1429, Dec 2008.

- [46] K. Biswas, *et al.*, "MEMS capacitive accelerometers," *Sensor Letters*, vol. 5, pp. 471-484, Sep-Dec 2007.
- [47] S. E. Alper, *et al.*, "Ultrathick and high-aspect-ratio nickel microgyroscope using EFAB multilayer additive electroforming," *Journal of Microelectromechanical Systems*, vol. 16, pp. 1025-1035, Oct 2007.
- [48] S. E. Alper, *et al.*, "A high-performance silicon-on-insulator MEMS gyroscope operating at atmospheric pressure," *Sensors and Actuators a-Physical*, vol. 135, pp. 34-42, Mar 30 2007.
- [49] X. Chen and D. W. Lee, "Integrated microactuation scanning probe microscopy system," *Journal of Vacuum Science & Technology B*, vol. 27, pp. 1408-1412, May 2009.
- [50] Y. H. Cho, *et al.*, "Viscous Damping Model for Laterally Oscillating Microstructures," *Journal of Microelectromechanical Systems*, vol. 3, pp. 81-87, Jun 1994.
- [51] T. R. Albrecht, *et al.*, "Frequency-Modulation Detection Using High-Q Cantilevers for Enhanced Force Microscope Sensitivity," *Journal of Applied Physics*, vol. 69, pp. 668-673, Jan 15 1991.
- [52] S. Wiak and K. Smolka, "Numerical modeling of 3-D comb drive electrostatic accelerometers structure (method of levitation force reduction)," *Compe-the International Journal for Computation and Mathematics in Electrical and Electronic Engineering*, vol. 28, pp. 593-602, 2009.
- [53] Y. C. Chen, *et al.*, "Modeling and Stability Analysis of Comb-Fingers in Mems Electrostatic Actuators," *Detc2008: Proceedings of the Asme International Design Engineering Technical Conference and Computers and Information in Engineering Conference*, Vol 4, pp. 641-646 917, 2009.
- [54] S. W. Chyuan, "Computational simulation for MEMS combdrive levitation using FEM," *Journal of Electrostatics*, vol. 66, pp. 361-365, Jul 2008.
- [55] Y. C. Chen, *et al.*, "On the side instability of comb-fingers in MEMS electrostatic devices," *Sensors and Actuators a-Physical*, vol. 148, pp. 201-210, Nov 4 2008.
- [56] F. D. Bannon, *et al.*, "High-Q HF microelectromechanical filters," *Ieee Journal of Solid-State Circuits*, vol. 35, pp. 512-526, Apr 2000.

- [57] V. Peykov, *et al.*, "Electrowetting: a model for contact-angle saturation," *Colloid and Polymer Science*, vol. 278, pp. 789-793, Aug 2000.
- [58] Q. S. Yu, *et al.*, "Engineering the surface and interface of Parylene C coatings by low-temperature plasmas," *Progress in Organic Coatings*, vol. 41, pp. 247-253, May 2001.
- [59] C. L. Pang, *et al.*, "Monolithic silicon probes with flexible parylene cables for neural prostheses," *2006 1st IEEE International Conference on Nano/Micro Engineered and Molecular Systems, Vols 1-3*, pp. 1125-1128 1549, 2006.
- [60] J. S. Song, *et al.*, "Improved Biocompatibility of Parylene-C Films Prepared by Chemical Vapor Deposition and the Subsequent Plasma Treatment," *Journal of Applied Polymer Science*, vol. 112, pp. 3677-3685, Jun 15 2009.
- [61] M. Linder, *et al.*, "In vivo reactions in mice and in vitro reactions in feline cells to implantable microchip transponders with different surface materials," *Veterinary Record*, vol. 165, pp. 45-50, Jul 11 2009.
- [62] J. Jakabovic, *et al.*, "Preparation and properties of thin parylene layers as the gate dielectrics for organic field effect transistors," *Microelectronics Journal*, vol. 40, pp. 595-597, Mar 2009.
- [63] S. Kota, *et al.*, "Design and Fabrication of Microelectromechanical Systems," *Journal of Mechanical Design*, vol. 116, pp. 1081-1088, Dec 1994.
- [64] J. C. Mark Walters, Allen Cowen, and Greg Hames, *SOIMUMPs Design Handbook*, 2002.
- [65] Micragem™. SOI MEMS Process [Online]. Available: <http://www.micralyne.com/micragem/>, 26.08.2010
- [66] Tronics-Microsystems. MEMSOI MPW [Online]. Available: <http://www.tronics.eu/mems-technology/memsoi-mpw-run-europractice.html>, 26.08.2010
- [67] C. W. Lin, *et al.*, "Implementation of SOG devices with embedded through-wafer silicon vias using a glass reflow process for wafer-level 3D MEMS integration," *Mems 2008: 21st Ieee International Conference on Micro Electro Mechanical Systems, Technical Digest*, pp. 802-805 1080, 2008.

- [68] Microposit. S1800 G2 Series Photoresists [Online]. Available: http://www.microresist.de/products/room_haas/pdf/Microposit_S1800_G2_Serie.pdf, 26.08.2010
- [69] S.-S. C. Services. Parylene Properties [Online]. Available: <http://www.scscoatings.com/docs/coatspec.pdf>, 26.08.2010
- [70] S.-E. M. Company. MicroPrime HP Primer [Online]. Available: http://www.microsi.com/photolithography/data_sheets/MicroPrimeHPPrimerDataSheet.pdf, 26.08.2010
- [71] A. E. Materials. AZ 9260 Photoresist [Online]. Available: http://www.az-em.com/pdfs/9200/az_9260_photoresist.pdf, 26.08.2010
- [72] S. E. Alper, "MEMS Gyroscopes for Tactical-Grade Inertial Measurement Applications," Doctor of Philosophy, The Graduate School of Natural and Applied Sciences, Middle East Technical University, Ankara, 2005.
- [73] Y. Y. Tan, *et al.*, "Modeling and simulation of the lag effect in a deep reactive ion etching process," *Journal of Micromechanics and Microengineering*, vol. 16, pp. 2570-2575, Dec 2006.
- [74] P. N. Wahjudi, *et al.*, "Improvement of metal and tissue adhesion on surface-modified parylene C," *Journal of Biomedical Materials Research Part A*, vol. 89A, pp. 206-214, Apr 2009.
- [75] A. Mata, *et al.*, "Characterization of polydimethylsiloxane (PDMS) properties for biomedical micro/nanosystems," *Biomedical Microdevices*, vol. 7, pp. 281-293, Dec 2005.

APPENDIX A

DETAILED ANALYSIS OF SPRING-MASS-DAMPER SYSTEM

A.1 Resonance with Damping (No Force exerted)

If we start with the equation of a spring mass damper system, than the system equation can be shown as following equation, if there is not a driving force of the system:

$$m\ddot{x} = -kx - c\dot{x}$$

where m is the mass and c is the coefficient of damping force and k is the spring constant. Or, equivalently we have

$$\ddot{x} + \frac{c}{m}\dot{x} + \frac{k}{m}x = 0 \quad (\text{A.1})$$

Using

$$w_0^2 = \frac{k}{m}$$

and

$$n = \frac{c}{2m}$$

rearranging equation (A.1), we have

$$\ddot{x} + 2n\dot{x} + w_0^2x = 0 \quad (\text{A.2})$$

where w_0 is the radial frequency of the vibration system if there is no damping (i.e., a free vibration) and n is called the coefficient of damping. By letting $x = Ae^{\lambda t}$, which is also a special solution to a 2nd order differential equation, we have

$$\lambda^2 + 2n\lambda + w_0^2 = 0 \quad (\text{A.3})$$

Equation (A.4) gives the solutions for equation (A.3).

$$\lambda_{1,2} = -n \pm \sqrt{n^2 - w_0^2} \quad (\text{A.4})$$

The performances of the system can be discussed according to the ratio between n and w_0 . The ratio $\zeta = n/w_0$ is known as the damping ratio of the system. We will investigate the damping behavior of the system with different damping coefficients since damping analysis gives deep understanding of the system behavior.

A.1.1 Slight Damping (Under-Damping)

If $n < w_0$, i.e., $\zeta < 1$, we have

$$\lambda_{1,2} = -n \pm i\sqrt{(w_0^2 - n^2)}$$

The solution to equation (A.2) is

$$x = Ae^{-nt} \sin(\sqrt{w_0^2 - n^2} t + \alpha) \quad (\text{A.5})$$

Equation (A.5) indicates that the system will have an oscillation, but it differs from the free vibration in that:

- i. The vibration frequency is $w_d = \sqrt{w_0^2 - n^2} = w_0 \sqrt{1 - \zeta^2}$, which is smaller than the free vibration frequency w_0 .

- ii. The amplitude of the vibration decays exponentially with time as can be seen with e^{-nt} term in the equation (A.5).

A.1.2 Heavy Damping (Over-damping)

If $n > w_0$, i.e., $\zeta > 1$, the solution to the equation (A.4) will be:

$$\lambda_{1,2} = -n \pm \sqrt{(n^2 - w_0^2)}$$

and again if we solve for equation (A.2);

$$x = e^{-nt} (c_1 e^{\sqrt{(n^2 - w_0^2)}t} + c_2 e^{-\sqrt{(n^2 - w_0^2)}t}) \quad (\text{A.6})$$

There is no oscillation of the displacement; the mass returns to its balanced position slowly.

A.1.3 Critical Damping

If $n = w_0$, i.e. $\zeta = 1$, we have $\lambda_1 = \lambda_2 = -n = -w_0$ and in this case, with only one root $\lambda = \lambda_1 = \lambda_2$, there is two solutions for $x(t)$ that $x(t) = e^{\lambda t}$ is one of the solutions and the other is $x(t) = te^{\lambda t}$. Therefore, the general solution to equation (A.2) is

$$x(t) = c_1 e^{-nt} (c_2 t + c_3) \quad (\text{A.7})$$

The result indicates that there is no oscillation in case of critical damping but the time taken for the displacement to become virtually zero is a minimum. Fig. 2.5.2 shows the $x(t)$ relations for the three damping conditions.

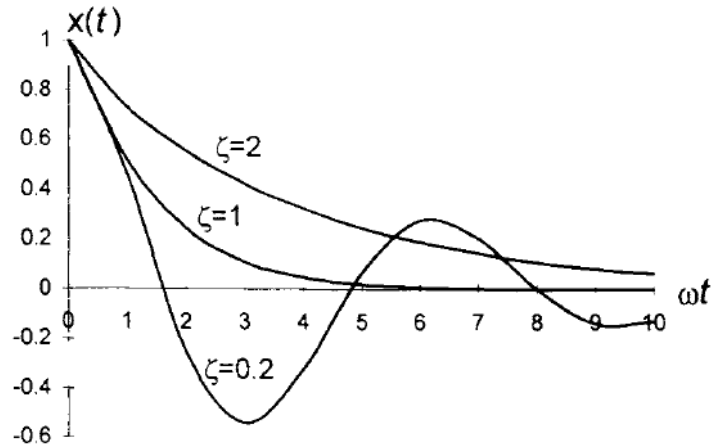


Figure A.1 Amplitude attenuation of systems for different damping ratio.

A.2 Resonance Driven by Force

Forced vibration response of the system is important to understand the driving mechanisms of the resonator for self resonant loop design. Suppose that a spring-mass system is set to continuous oscillation by applying a sinusoidal force with a frequency of ω and amplitude of F_0

$$F = F_0 \sin(\omega t)$$

the differential equation for the system is:

$$m\ddot{x} = -kx - c\dot{x} + F_0 \sin(\omega t) \quad (\text{A.8})$$

The solution to equation (2.1) can be analyzed in two parts: homogenous solution and particular solution.

To solve for homogenous solution, we have to solve the equation (2.2).

$$m\ddot{x}_h + c\dot{x}_h + kx_h = 0 \quad (\text{A.9})$$

The solution to equation (2.2) is known to be damped oscillation (for $n < w_0$)

$$x_h = Ae^{-nt} \sin(\sqrt{(w_0^2 - n^2)}t + \alpha)$$

To solve for the particular solution, a specific solution with stable oscillation characteristic will be used and the parameters of the solution will be determined by using equation (2.1).

$$x_p = B \sin(\omega t - \varphi) \quad (\text{A.10})$$

where B is the amplitude of the resulting vibration and φ the phase lag of the vibration against the sinusoidal force. By substituting equation (2.4) into equation (2.1), and solving the equation leads two equations:

$$B(w_0^2 - \omega^2) - f \cos \varphi = 0$$

and

$$2nB\omega - f \sin \varphi = 0$$

Therefore the amplitude B and the phase lag φ are found to be

$$B = \frac{f}{\sqrt{(w_0^2 - \omega^2)^2 - 4n^2\omega^2}} \quad (\text{A.11})$$

and

$$\varphi = \tan^{-1} \frac{2n\omega}{w_0^2 - \omega^2} \quad (\text{A.12})$$

Thus, the solution to equation (2.1) is,

$$x = Ae^{-nt} \sin(\sqrt{(w_0^2 - n^2)}t + \alpha) + B \sin(\omega t - \varphi) \quad (\text{A.13})$$

The solution given in equation (2.10) indicates that, in the early stages, beats occur due to forced vibration and damped vibration, giving rise to transient oscillations, which are usually short-lived and can be ignored in most cases. We will only consider what happens when conditions are steady.

We will investigate the vibration frequency, amplitude characteristics for different frequencies and phase lag of the system.

A.2.1 Vibration Frequency

The frequency of the steady vibration is the same as the frequency of the driving force. However, there is a phase lag that is a function of the free vibration frequency w_0 , the driving frequency w and the damping coefficient n , as is shown by equation (2.9).

A.2.2 Amplitude

The amplitude of the steady vibration is given by equation (2.7). It can be written as

$$B = \frac{B_0}{\sqrt{\left(1 - \frac{w^2}{w_0^2}\right)^2 + 4\left(\frac{n}{w_0}\right)^2 \left(\frac{w}{w_0}\right)^2}}$$

where $B_0 = F_0/k$ is the static displacement of the mass caused by a constant force F_0 . For $w/w_0 = \lambda$ and $B/B_0 = \beta$, we have

$$\beta = \frac{1}{\sqrt{(1 - \lambda^2)^2 + 4\zeta^2\lambda^2}} \quad (\text{A.14})$$

For a constant force amplitude F_0 , the dependence of β on the driving frequency is:

(a) Low Driving Frequencies ($w \ll w_0$ or $\lambda \ll 1$)

In this case, $\beta \approx 1$. This means that the amplitude is the same as the displacement caused by the static force F_0 .

(b) Medium Frequencies ($w \approx w_0$ or $\lambda \approx 1$)

The amplitude has a maximum at $w = w_0 \sqrt{1 - 2\zeta^2}$. If the damping is light ($\zeta < 0.7$), w is very closer to w_0 and β is approximately equal to $1/2\zeta$, which can be very large for small ζ . The resonance peak disappears at $\zeta \geq 0.7$. In this case, the curve for $\beta \sim w$ relation has the largest flat region (i.e., the largest bandwidth). Therefore, $\zeta = 0.7$ is often referred to as an optimum damping condition.

(c) High Frequencies ($w \gg w_0$ or $\lambda \gg 1$)

In this case, we have $\beta \approx 1/\lambda^2$. This means that the amplitude decreases very fast with frequency.

Example curves showing the frequency dependence of the relative amplitude are given in Fig. 2.5.4, which shows that the amplitude of a forced vibration is a function of driving frequency and the damping ratio.

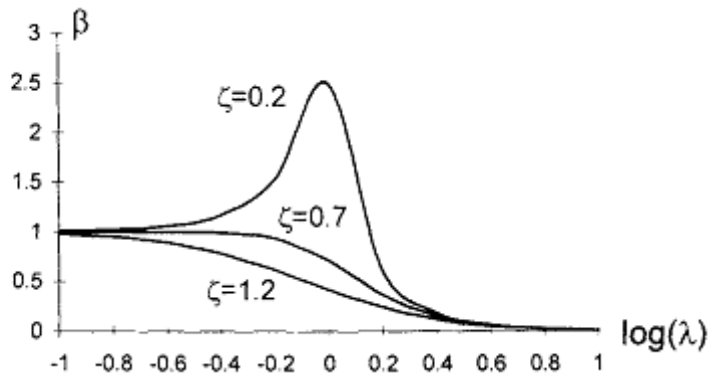


Figure A.2 Amplitude frequency relations for different damping ratios.

A.2.3 Phase Lag

The forced vibration takes on the frequency of the driving force, but it has a phase lag as shown in equation (2.9). For very small w , ϕ is close to zero. ϕ increases with w , passes $\pi/2$ at the natural frequencies of the system and approaches π at very high frequency, as shown in Fig. 2.5.5.

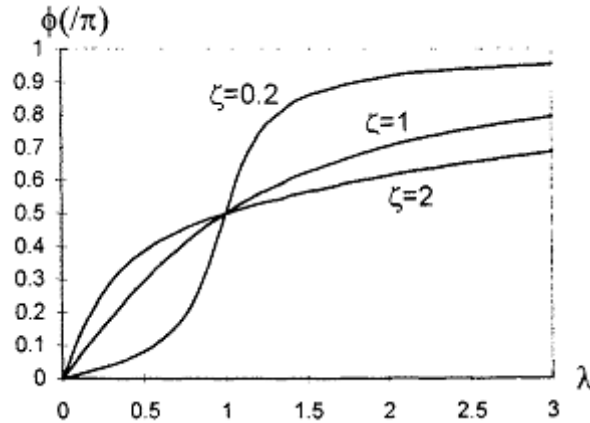


Figure A.3 Phase lag of forced vibrations for different damping ratios.

A.3 Resonance and Quality Factor

A.3.1 Resonant Frequency

According to equation (A.14) or Fig. 2.5.4, for slight damping, the amplitude has maximum at a frequency near the free vibration frequency. This phenomenon is known as resonance and the corresponding frequency is called resonant frequency. Using the condition of $d\beta/d\lambda = 0$, we find that the resonant frequency of a forced vibration is $\lambda_r = \sqrt{1 - 2\zeta^2}$ or $w_r = w_0\sqrt{1 - 2\zeta^2}$. As the natural vibration frequency (without damping) of the system is w_0 and the damped vibration frequency of the system is

$w_d = w_0\sqrt{1 - \zeta^2}$ we find that, for slight damping, w_0 , w_d and w_r are all close to each other.

At resonant frequency the relative amplitude reaches a maximum value

$$\beta_r = \frac{1}{2\zeta\sqrt{1 - \zeta^2}} \quad (\text{A.15})$$

For slight damping, we have the amplitude at resonance: $\beta_r \approx 1/2\zeta$.

A.3.2 Phase Lag at Resonance

By substituting w_r into equation (2.9), we have the phase lag at resonance

$$\varphi_r = \tan^{-1} \frac{\sqrt{1 - 2\zeta^2}}{\zeta} \quad (\text{A.16})$$

For slight damping, $\varphi_r = \tan^{-1} 1/\zeta = \pi/2$ or $\zeta = 1/\tan \varphi_r$.

A.3.3 Quality Factor

For many sensor applications, the sharpness of the designed resonator, that is the band pass filter is important for high resolution or high accuracy of measurement. Therefore, the more the quality factor, the more the filter rejects other frequencies different than the natural frequency of the structure. Generally Q -factor determines how under-damped an oscillator or resonator is. Quality factor can be explained in different domains like energy domain or in frequency domain.

Q is mathematically defined as the peak value of the relative amplitude at resonant frequency, i.e.,

$$Q = \beta_r = \frac{1}{2\zeta\sqrt{1-\zeta^2}} \quad (\text{A.17})$$

It is reasonable to find that Q is related to the damping ratio ζ . The smaller the damping ratio, the larger the Q is.

In physics, higher Q indicates a lower rate of energy loss relative to the stored energy of the oscillator; the oscillations die out more slowly, that is,

$$Q = 2\pi \frac{E}{\Delta E} \quad (\text{A.18})$$

where E is the total energy of the vibration system and ΔE is the energy dissipated by damping in one cycle (equals 2π radian) of oscillation. For a system vibrating at its resonant frequency w_r , the displacement is

$$x = A \sin w_r t$$

The total energy of the system is

$$E = \frac{1}{2} m \dot{x}^2 = \frac{1}{2} m A^2 w_r^2$$

The energy dissipation in one cycle is

$$\Delta E = - \int_0^T F_d \dot{x} dt$$

where F_d is the damping force, i.e., $F_d = -c\dot{x}$. Therefore, we have

$$\Delta E = \int_0^T c \dot{x}^2 dt = \pi c A^2 w_r$$

and

$$Q = 2\pi \frac{E}{\Delta E} = \frac{m w_r}{c}$$

By using $n = \frac{c}{2m}$ and $\zeta = \frac{n}{w_o} \cong \frac{n}{w_r}$, we have $Q \cong \frac{1}{2\zeta}$

In electrical resonant circuits also uses the Q -factor to determine the filter characteristics. The energy of a vibration system is proportional to the square of the vibration amplitude. At resonance, the system has its maximum energy

$$E_r = C\beta_r^2$$

The relative amplitude for a half maximum energy is $\beta_r/\sqrt{2}$. There are two frequencies for the amplitude: one is smaller than w_r and another larger than w_r . If the two frequencies are w_1 and w_2 , the corresponding relative frequencies, λ_1 and λ_2 , can be found by the equation

$$\frac{1}{\sqrt{(1-\lambda^2)^2 + 4\zeta^2\lambda^2}} = \frac{1}{\sqrt{2}}\beta_r$$

λ_1 and λ_2 are found to be

$$\lambda_{1,2} = \sqrt{1-2\zeta^2} \left(1 \pm \frac{\zeta}{1-2\zeta^2} \right)$$

This leads to

$$\Delta\lambda = \lambda_1 - \lambda_2 = \sqrt{1-2\zeta^2} \frac{2\zeta}{1-2\zeta^2} = \frac{2\zeta}{\sqrt{1-2\zeta^2}}$$

Therefore, for slight damping, we have

$$\frac{\lambda_r}{\Delta\lambda} = \frac{1-2\zeta^2}{2\zeta} \approx \frac{1}{2\zeta}$$

This means that the Q factor can be equally defined as

$$Q = \frac{\lambda_r}{\Delta\lambda} \tag{A.19}$$

It is clear that the three definitions are equivalent for small ζ , i.e., for a large Q value. For silicon micro resonators in air, the Q value is usually of the order of 100. It may go up to over one hundred thousand in a vacuum.

A.3.4 The Measurement of Quality Factor

Q factor is a very important parameter to characterize a vibration system. As the damping ratio that determines the Q factor is usually very small and difficult to estimate theoretically, and usually found through experimental measurements.

According to the basic definition, Q is equal to the relative amplitude of the system at resonance, i.e., β_r . Therefore, if we find amplitude-frequency relation for a constant driving force for frequencies from dc to a frequency higher than the resonant frequency, $Q = \beta_r$ can be found at the resonant frequency. As the measurement must cover large frequency range and the amplitude may change by several orders of magnitude, the measurement is often time-consuming and inaccurate.

According to equation (A.19), Q can be found by the A-f measurement in a small frequency range near the resonant frequency. First, we find the resonant frequency f_r and the amplitude A_r at the frequency. Then the amplitude-frequency relation around the resonant frequency is measured so that the frequencies f_1 and f_2 with amplitude of $A_r/\sqrt{2}$ are found. The Q can be found by the relation $Q = \frac{f_r}{f_2 - f_1}$.

According to equation (A.16) and equation (A.17), Q is related to the damping ratio ζ , which is related to the phase lag at resonance. Therefore, we first find the resonant frequency ω_r and then find the phase lag φ_r at resonant frequency. Q can then be calculated by

$$Q = \frac{\tan(\varphi_r)}{2}$$

APPENDIX B

COMSOL AND MATLAB SIMULATIONS OF GRAVIMETRIC RARE CELL DETECTORS

B.1 COMSOL Model Analysis of Devices

4015a1f20b Modal Analysis in COMSOL

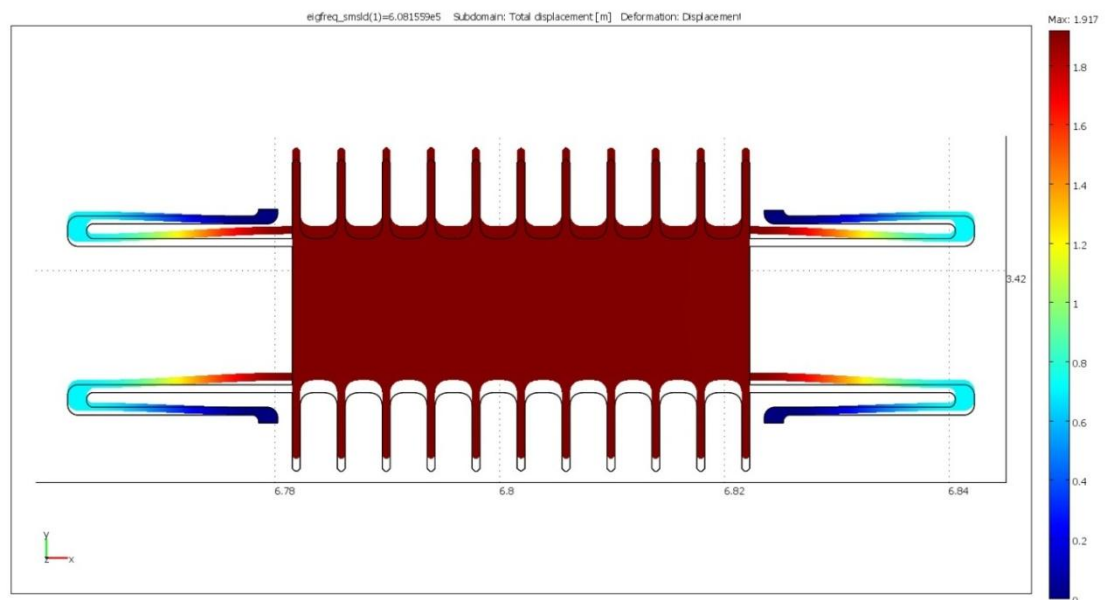


Figure B.1 First Mode of device with code 4015A1F20B at 608.16 KHz

4015a2f20b Modal Analysis in COMSOL

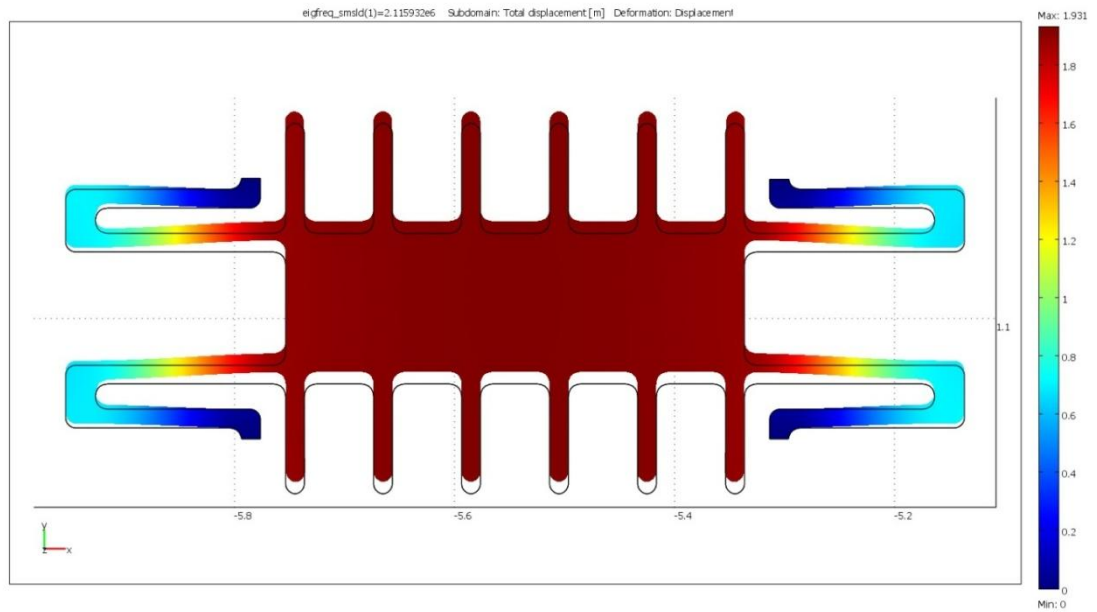


Figure B.2 First Mode of device with code 4015A2F20B at 2.12 MHz

4015a2f40b Modal Analysis in COMSOL

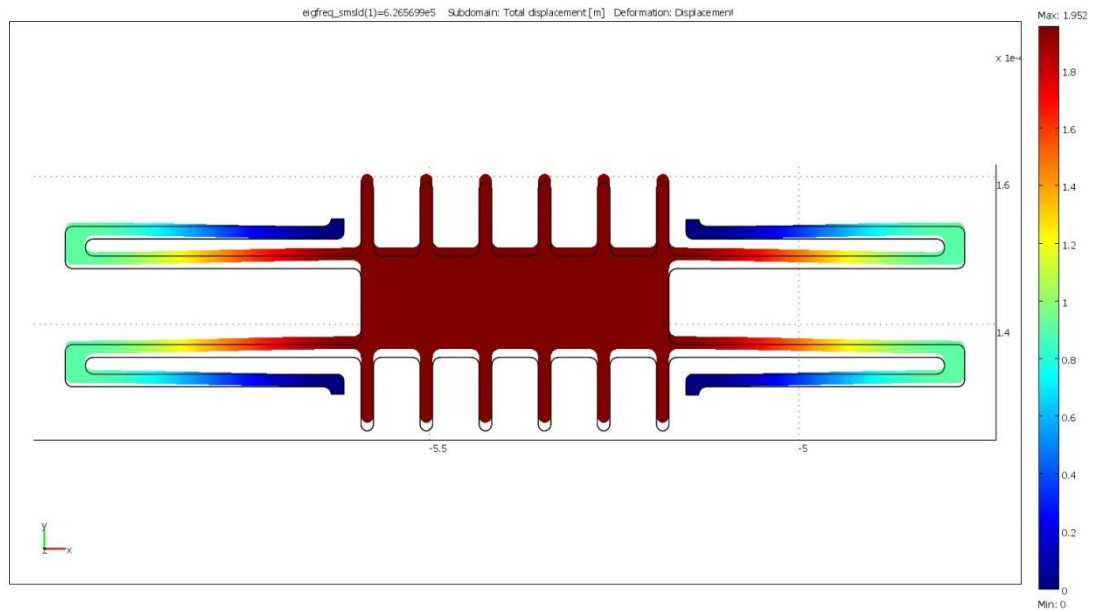


Figure B.3 First Mode of device with code 4015A2F40B at 626.57 KHz

8015a1f20b Modal Analysis in COMSOL

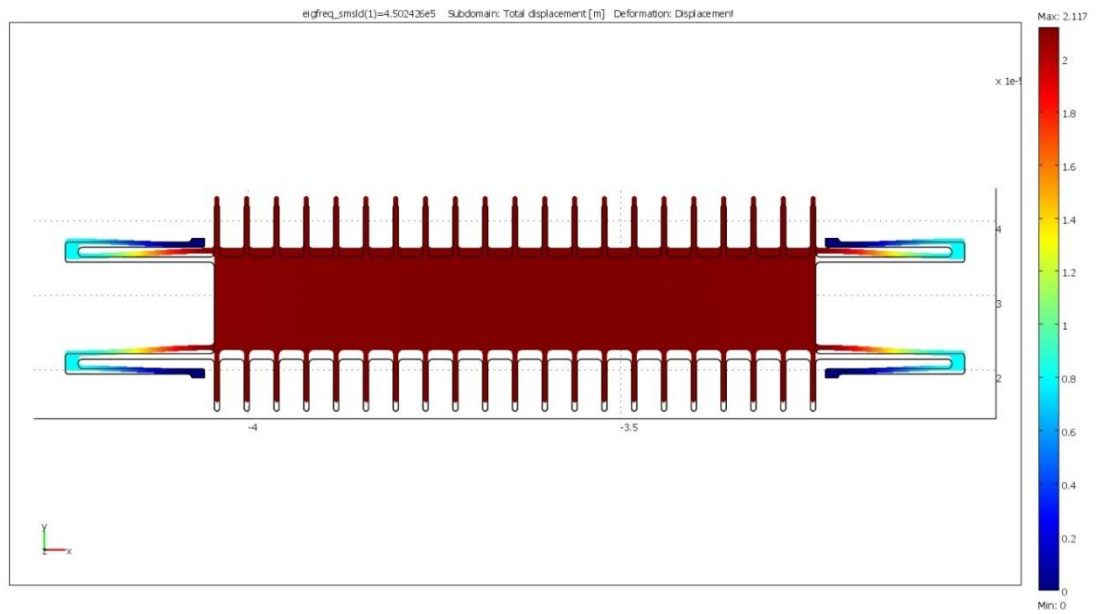


Figure B.4 First Mode of device with code 8015A1F20B at 450.24 KHz

8015a2f40b Modal Analysis in COMSOL

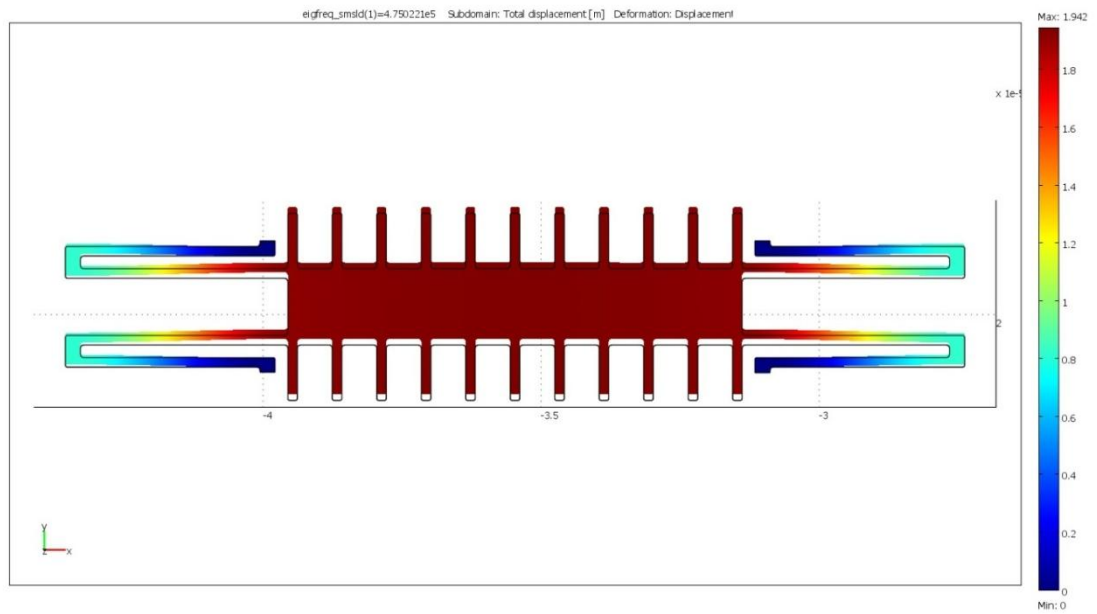


Figure B.5 First Mode of device with code 8015A2F40B at 475.02 KHz

8015a4f40b Modal Analysis in COMSOL

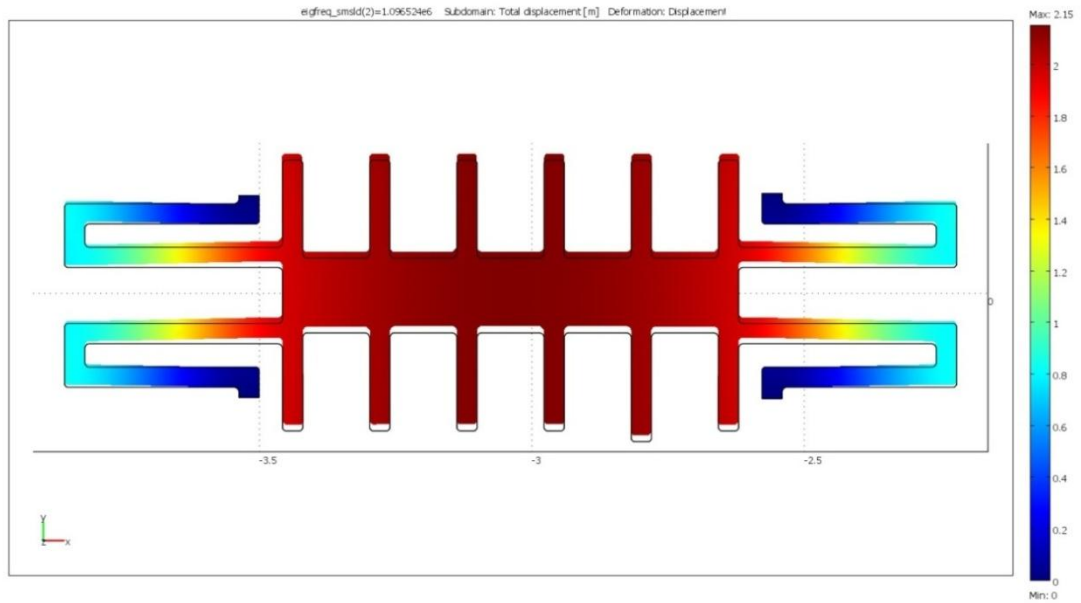


Figure B.6 Second Mode of device with code 8015A4F40B at 1.10 MHz

8030a2f40b Modal Analysis in COMSOL

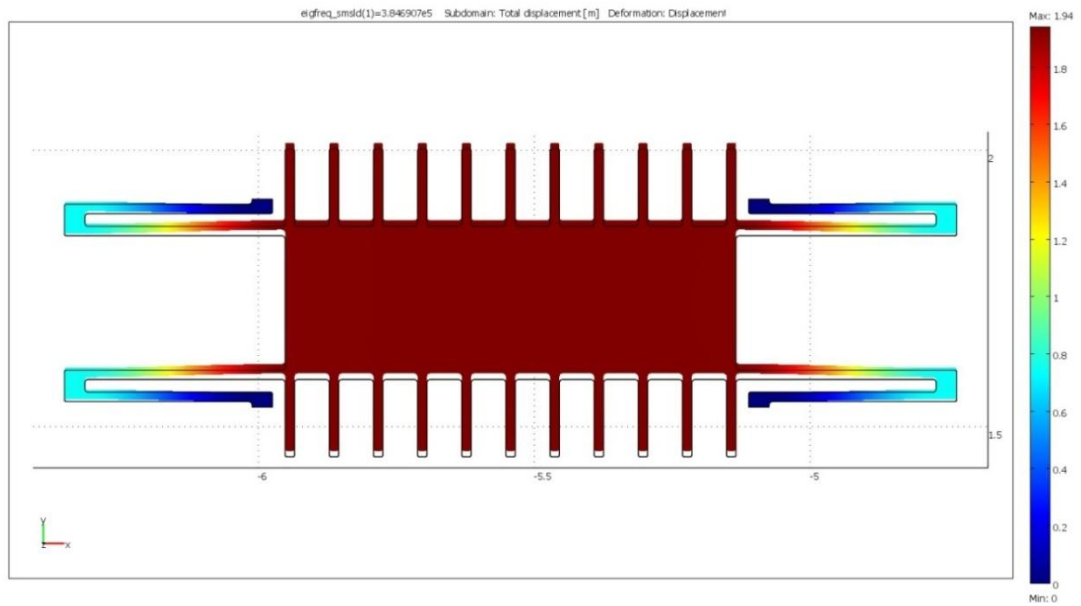


Figure B.7 First Mode of device with code 8030A2F40B at 384.69 KHz

8030a4f40b Modal Analysis in COMSOL

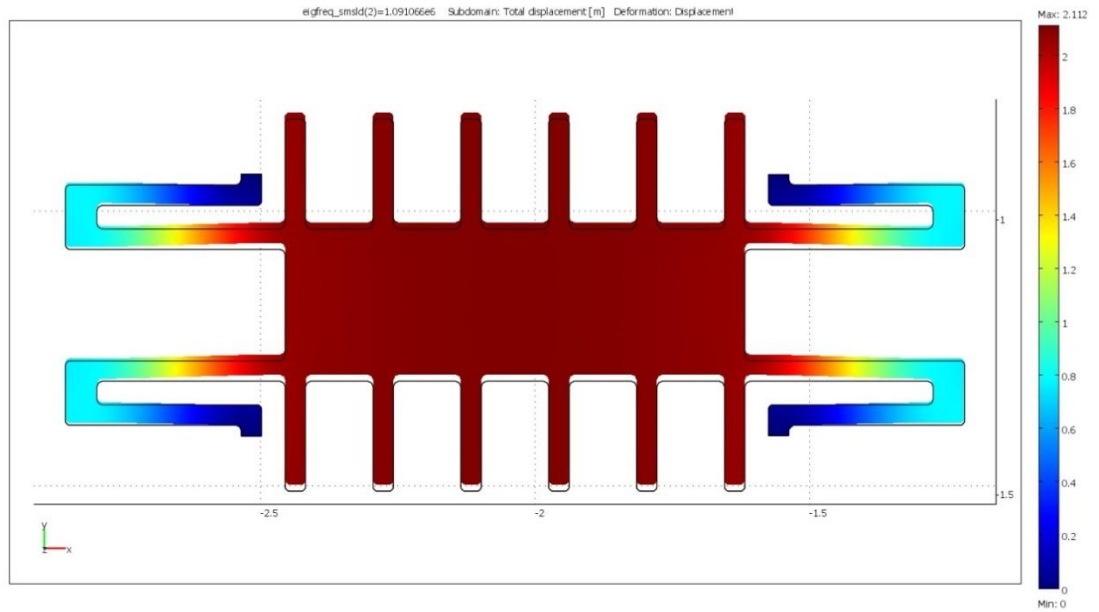


Figure B.8 Second Mode of device with code 8030A4F40B at 1.09 MHz

16030a4f40b Modal Analysis in COMSOL

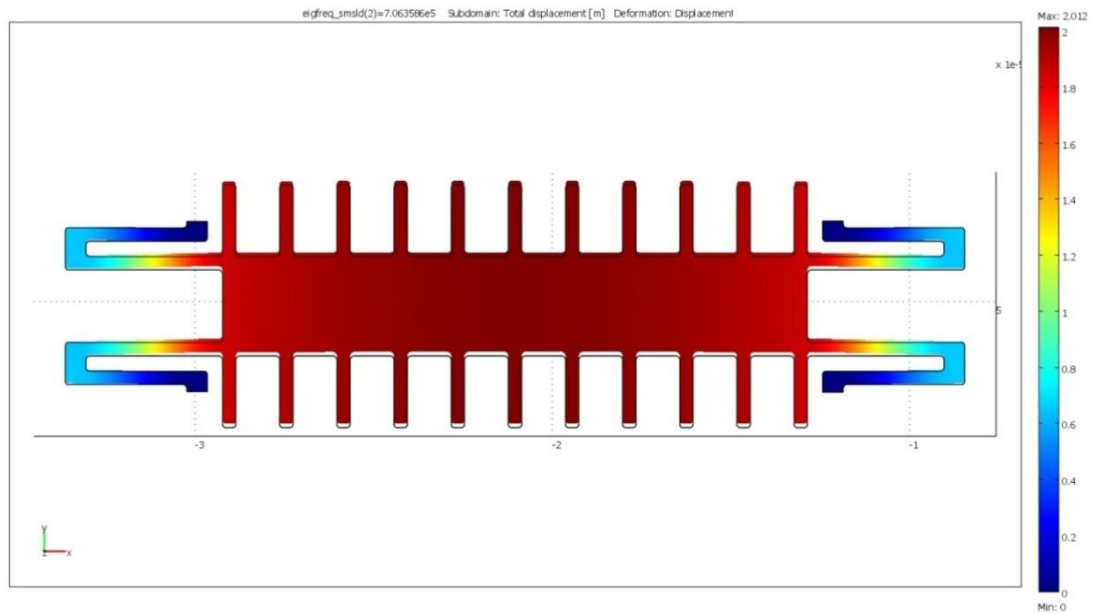


Figure B.9 Second Mode of device with code 16030A4F40B at 706.00 KHz

16030a4f80b Modal Analysis in COMSOL

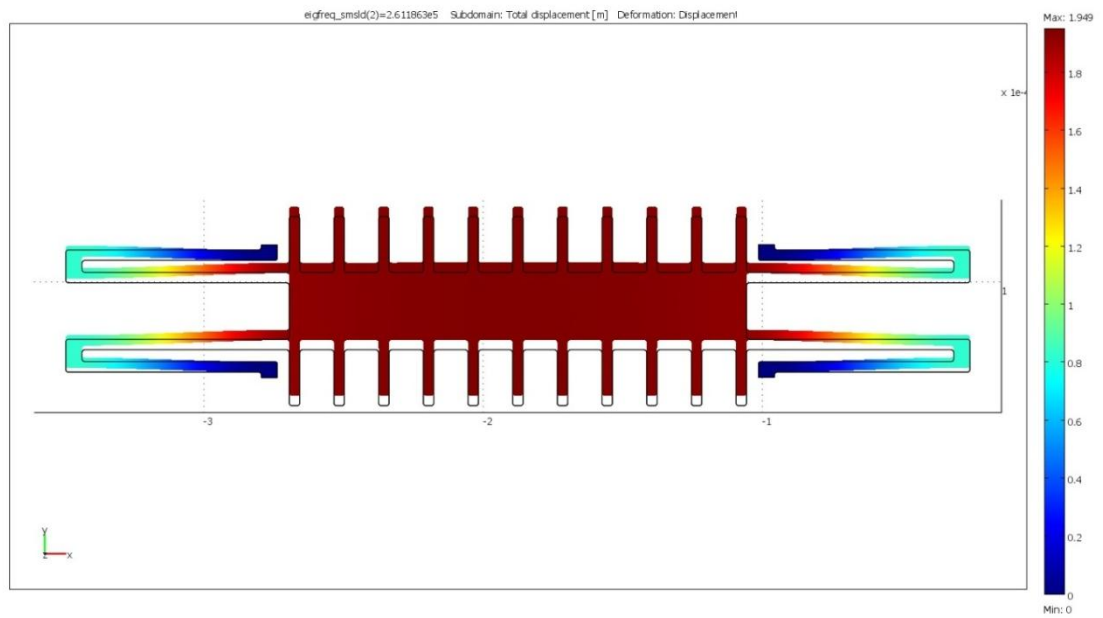


Figure B.10 Second Mode of device with code 16030A4F80B at 261.19 KHz

B.2 MATLAB Simulations

4015a1f20b Open Loop Resonance Frequency Simulations in MATLAB

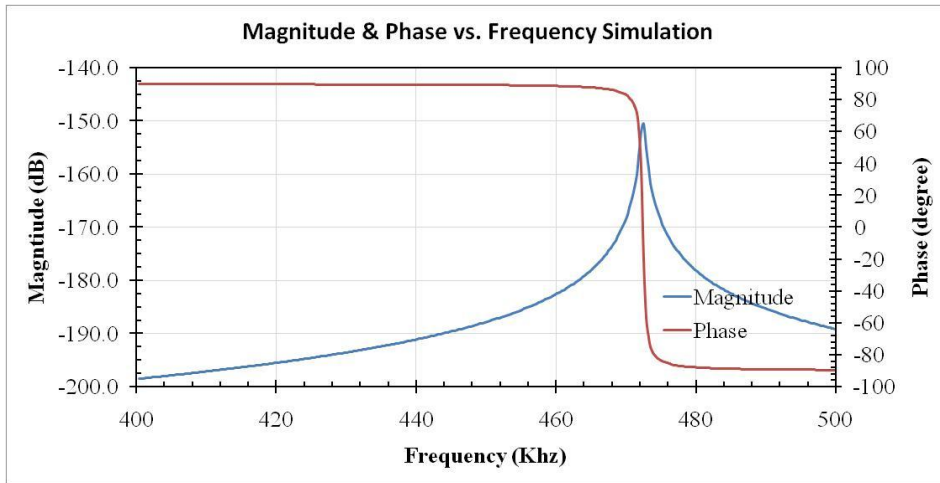


Figure B.11 Magnitude and Phase Response Simulation in MATLAB for device with code 4015A1F20B

4015a2f20b Open Loop Resonance Frequency Simulations in MATLAB

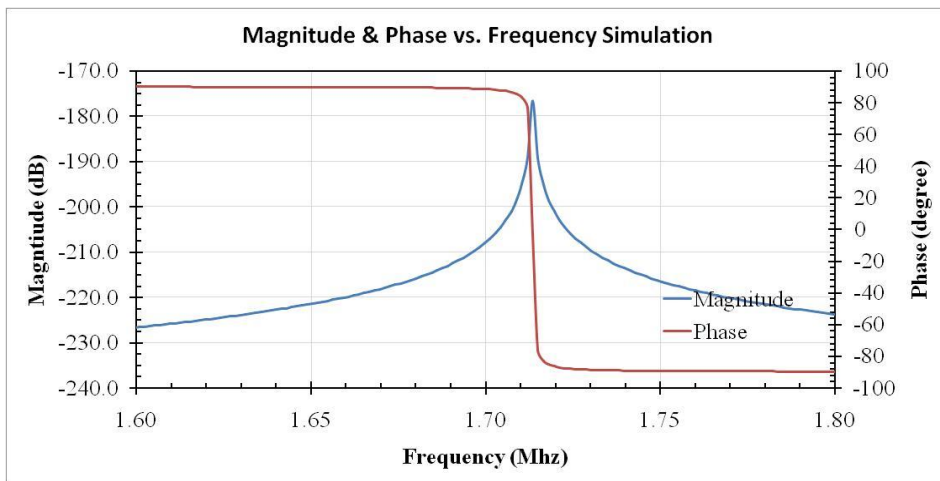


Figure B.12 Magnitude and Phase Response Simulation in MATLAB for device with code 4015A2F20B

4015a2f40b Open Loop Resonance Frequency Simulations in MATLAB

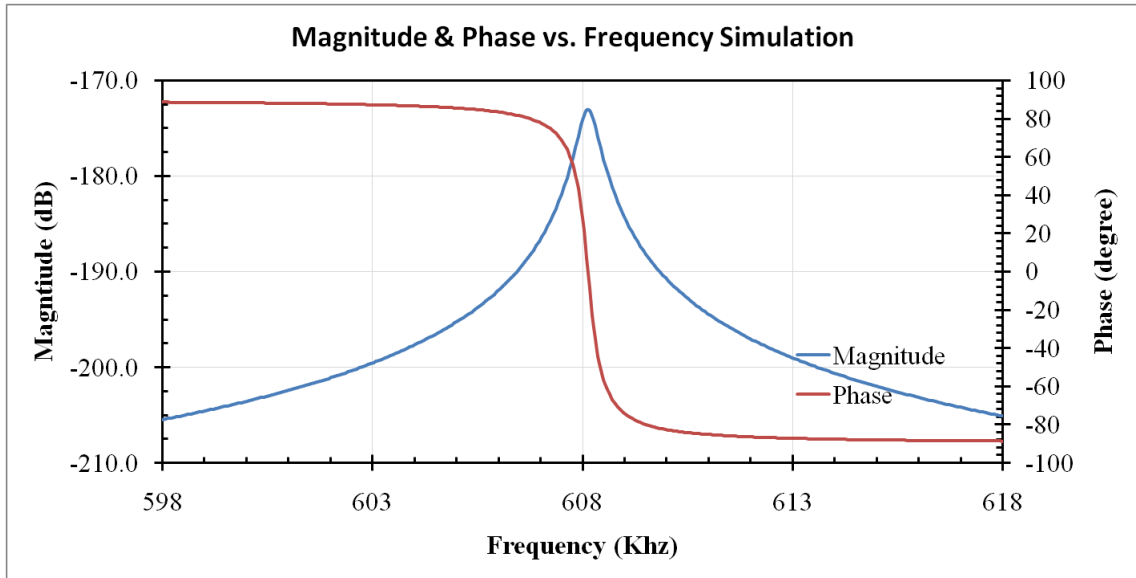


Figure B.13 First Mode of device with code 4015A2F40B at 626.57 KHz

8015a1f20b Open Loop Resonance Frequency Simulations in MATLAB

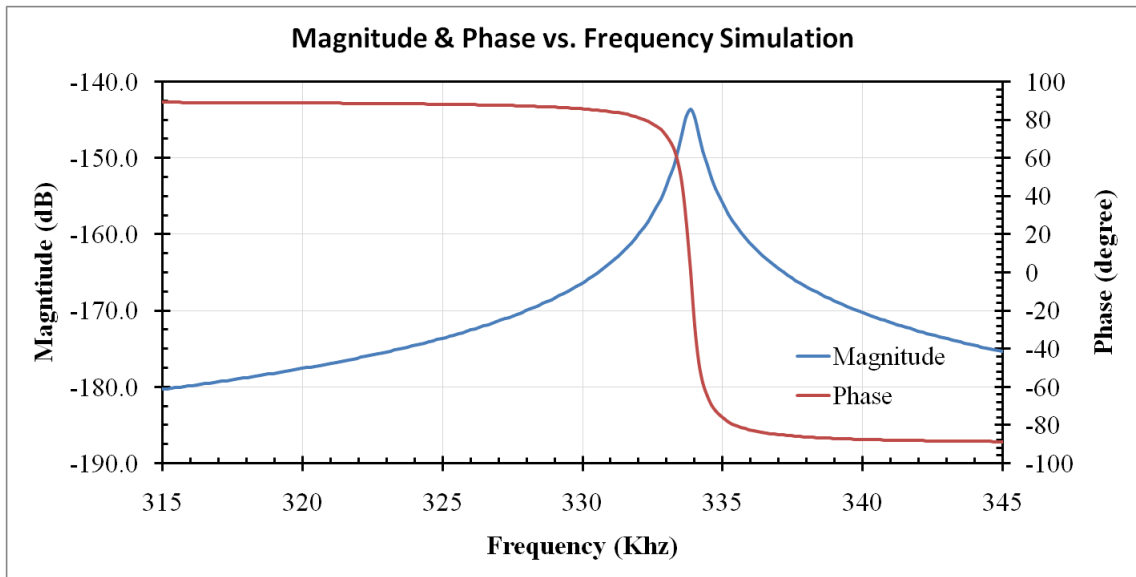


Figure B.14 First Mode of device with code 8015A1F20B at 450.24 KHz

8015a2f40b Open Loop Resonance Frequency Simulations in MATLAB

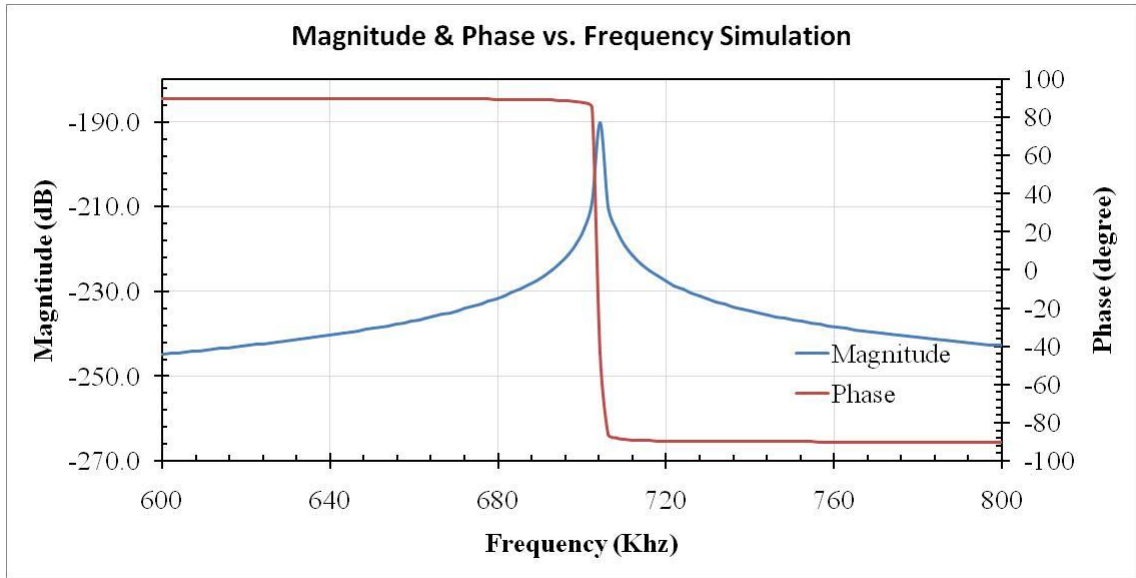


Figure B.15 First Mode of device with code 8015A2F40B at 475.02 KHz

8015a4f40b Open Loop Resonance Frequency Simulations in MATLAB

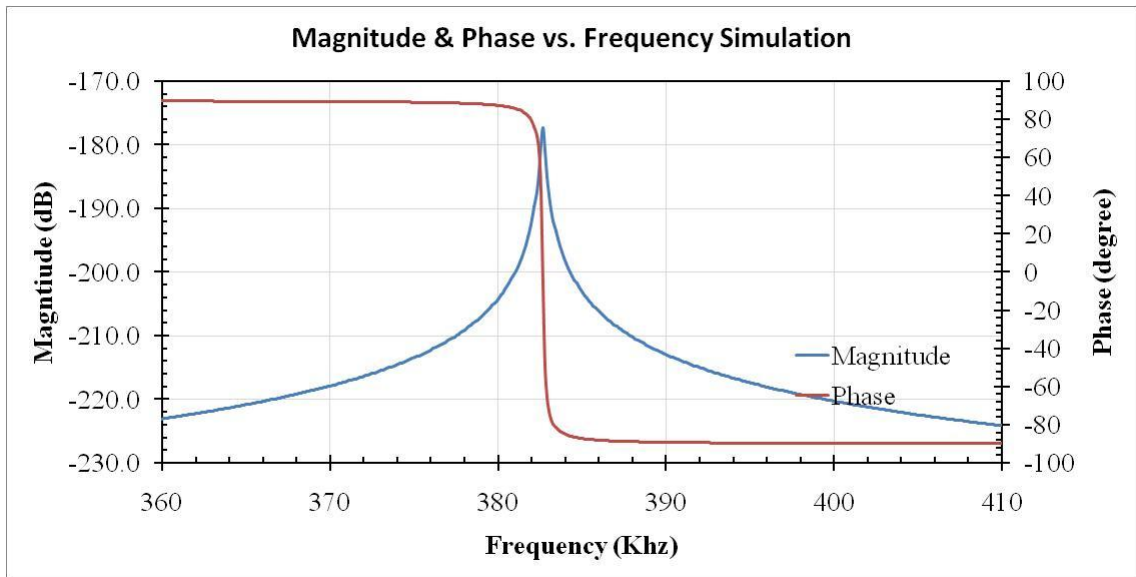


Figure B.16 First Mode of device with code 8015A4F40B at 855.25 KHz

8030a2f40b Open Loop Resonance Frequency Simulations in MATLAB

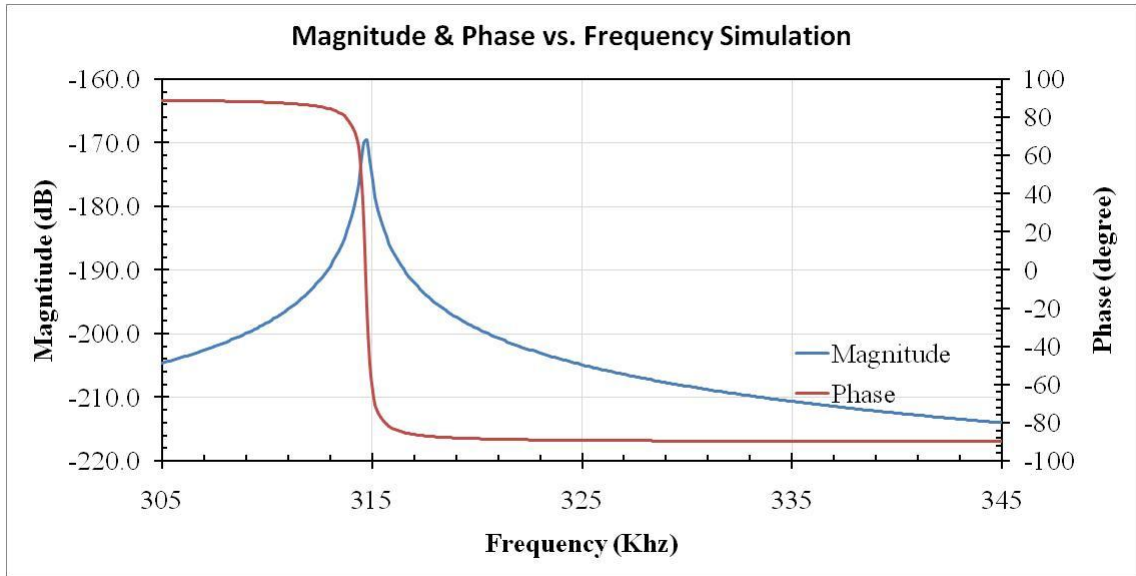


Figure B.17 First Mode of device with code 8030A2F40B at 384.69 KHz

8030a4f40b Open Loop Resonance Frequency Simulations in MATLAB

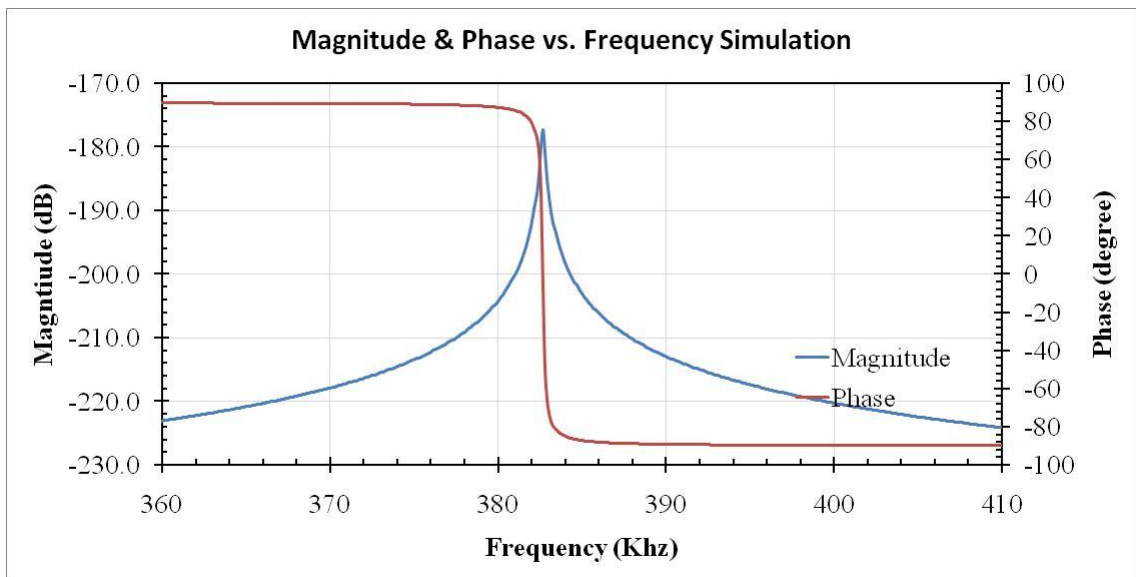


Figure B.18 First Mode of device with code 8030A4F40B at 861.67 KHz

16030a4f40b Open Loop Resonance Frequency Simulations in MATLAB

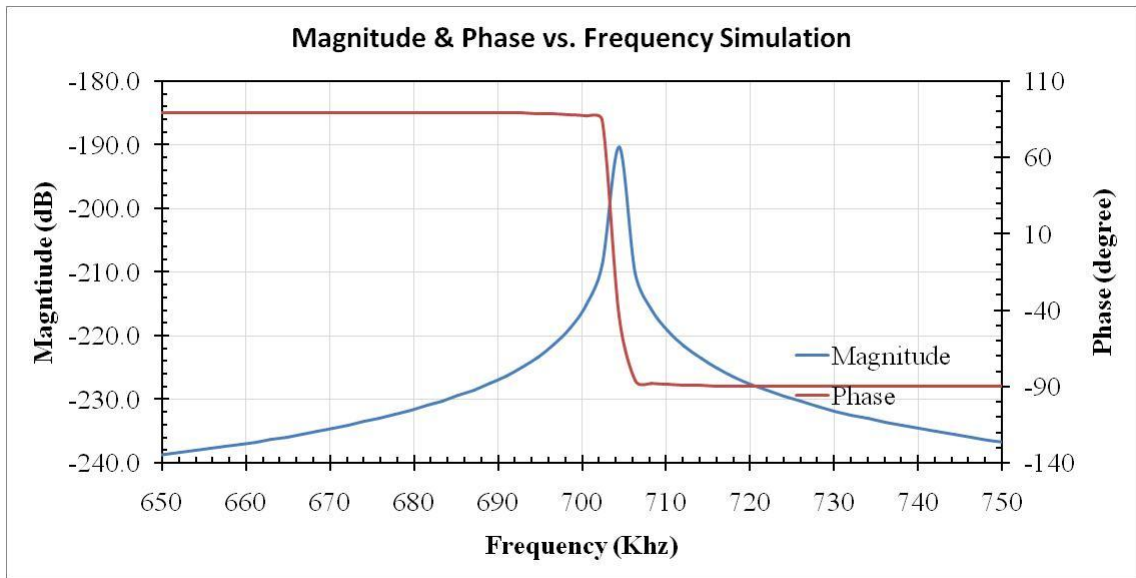


Figure B.19 First Mode of device with code 16030A4F40B at 387.00 KHz

16030a4f80b Open Loop Resonance Frequency Simulations in MATLAB

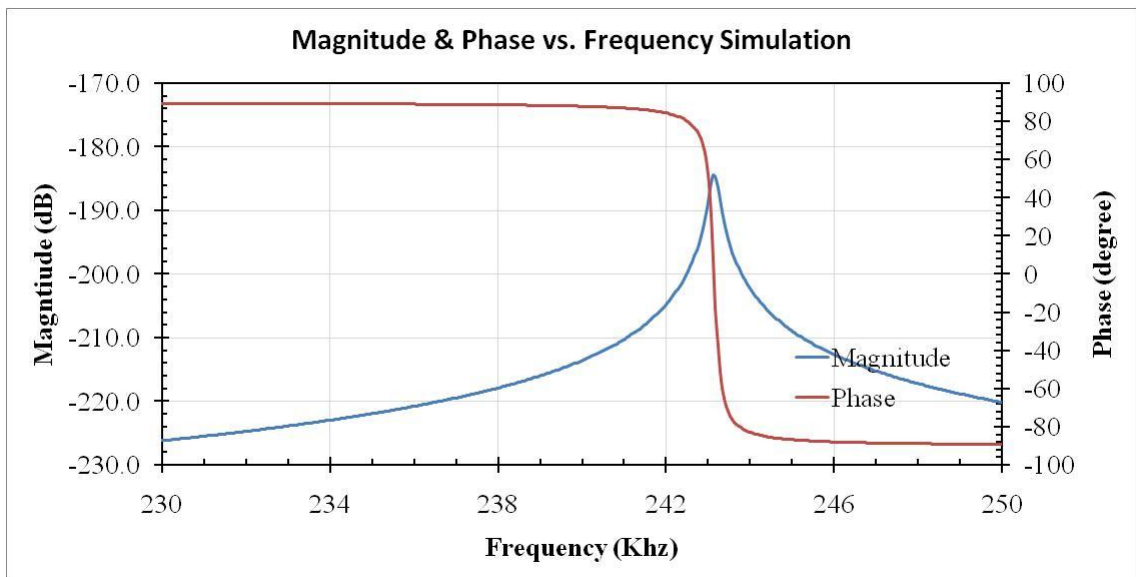


Figure B.20 First Mode of device with code 16030A4F80B at 228.45 KHz